WIND CLIMATOLOGY OF QUESNEL LAKE, BRITISH COLUMBIA

by

Hadleigh David Thompson

B.Sc. Atmospheric Science, The University of British Columbia, 2016

THESIS SUBMITTED IN PARTIAL FULFILLMENT OF
THE REQUIREMENTS FOR THE DEGREE OF
MASTER OF SCIENCE
IN
NATURAL RESOURCES AND ENVIRONMENTAL STUDIES

UNIVERSITY OF NORTHERN BRITISH COLUMBIA

April 2019

Committee Members:

Supervisor: Stephen Déry, Ph.D

Environmental Science and Engineering Program

University of Northern British Columbia, Prince George, Canada.

Committee Member: Peter Jackson, Ph.D

Environmental Science and Engineering Program

University of Northern British Columbia, Prince George, Canada.

Committee Member: Bernard Laval, Ph.D

Department of Civil Engineering

University of British Columbia, Vancouver, Canada.

Abstract

Intermontane lakes are often enclosed by complex topography that creates difficulty in resolving the local and regional wind fields. Quesnel Lake, nestled into the western flank of the Cariboo Mountains in central British Columbia, is one such lake. This study examines the wind climatology of Quesnel Lake at three distinct spatial and temporal scales. Firstly, long-term wind data from meteorological stations bordering the Cariboo Mountains exhibit a cycle of calm and active periods throughout the year. Secondly, an environment-to-circulation synoptic climatology is presented that illustrates the large-scale atmospheric patterns that lead to strong wind events at the lake. Finally, the spatial and temporal variability of the near-surface wind field has been examined using an array of shore-based meteorological stations. The response of the wind field to synoptic forcing is found to be driven primarily by the orientation of the regional 800 hPa pressure gradient.

Contents

List of Tables

List of Figures

Acknowledgments

The development and completion of this thesis would not have been possible without the generous guidance and expert advice of my supervisor, Stephen Déry, and committee members Peter Jackson, and Bernard Laval. All three have been instrumental in my progress as a graduate student throughout this Masters degree. My sincere thanks to Dr. Douw Steyn for his time and energy in reviewing this thesis and providing such valuable feedback. I would like to acknowledge all of the principal investigators and fellow graduate students working on the Mount Polley project, of which there are too many to list here, however, a special mention must go to Ellen Petticrew and Phil Owens for welcoming my meteorological contributions to the broader research investigations that are still ongoing at Quesnel Lake.

The practical aspects of site visits and data collection at Quesnel Lake would not have been possible without assistance from Michael Allchin, Lazlo Enyedy, and all of the Quesnel River Research Centre staff. Many thanks also to the various field assistants of the Northern Hydrometeorology Group who have all contributed by installing instruments, collecting data, and providing logistical support. I must acknowledge the invaluable loan of meteorological equipment from Ken Otter, without which I would not have been able to collect data used throughout Chapter 5.

Financial support has been provided by Environment and Climate Change Canada's Environmental Damages Fund, and in-part by the Natural Sciences and Engineering Research Council of Canada, and the University of Northern British Columbia's Office of Research and Graduate Programs.

Finally, I am indebted to my wife Kirstin for accompanying me on this journey, and providing me with all the support a husband could ever ask for.

”Air in motion, which is wind, in passing over the smooth surface of the water, may rub, as it were, upon that surface, and raise it into wrinkles, which, if the wind continues, are the elements of future waves”

—Benjamin Franklin

1 Introduction

1.1 Motivation

Interactions of the lower atmospheric boundary layer (ABL) with an underlying water surface provides opportunities for the exchange of mass, energy, and momentum (Spigel and Imberger, 1980; Hodges et al., 2000). The transfer of turbulent kinetic energy (TKE) and momentum can drive physical processes within a body of water, and are of particular interest to limnologists modelling lake hydrodynamics. The frictional interaction at the air-water interface which allows for momentum transfer to occur will then produce downwind movement in the lake's surface layer. This influence of wind upon the water surface is known as *wind forcing*. Sufficient wind forcing is one mechanism of forcing basin-scale waves known as seiche, which are standing waves at the surface (surface seiche) and density interfaces (internal seiche) (Antenucci and Imberger, 2003; Gardner et al., 2006).

Internal seiches in Quesnel Lake, British Columbia (BC), have been previously cited for their role in downstream temperature fluctuations (Laval et al., 2008), the lake's thermal energy balance (Potts, 2004), and possible sediment re-suspension (Petticrew et al., 2015). The Mount Polley mine spill into the West Basin of Quesnel Lake that occurred on 4 August 2014 now provides motivation for further physical limnology research, including the need to clarify the role of wind forcing in mixing events, seasonal overturning, and seiche events. This research is part of a larger inter-disciplinary investigation to understand the long term physical, chemical, and biological effects of the spill. A hydrology-based climatology of the Quesnel Lake watershed by Burford et al. (2009) analyzed long-term trends in temperature, precipitation and run-off in the region. However, a detailed wind climatology, investigating the seasonal nature of wind and its spatial and temporal variability, is currently missing from the literature. An analysis of wind data from the Quesnel Lake

basin and surrounding region will contribute to a better understanding of Quesnel Lake's limnology, and the regional climate.

Wind observations at only a single spatial or temporal scale do not account for the highly-variable nature of wind and the influence that topography, atmospheric boundary layer (ABL) stability, and surface roughness can have on the wind field. To compile a wind-climatology for Quesnel Lake, I have considered multiple spatial and temporal resolutions, similar to a meteorologist's *Forecasters-funnel* (see Meyers and Steenburgh, 2013). The resultant climatology will comprise wind observations at lake-level being interpreted in context of the synoptic forcing and seasonal patterns.

1.2 Objectives

The two primary objectives of this research are:

1. To identify the typical wind conditions that could be expected at a given location within the Quesnel Lake basin at a given time of year, and to lesser extent, time of day.

2. To identify the major synoptic-scale atmospheric patterns responsible for periods of wind forcing sufficient in strength to excite seiche activity within the lake.

The organization of this thesis is as follows: Chapter 1 provides an outline to the problem, my objectives, and a review of literature, focused on wind-forcing, the seasonal nature of winds, and previous wind climatologies. Chapter 2 outlines the study area, weather station locations, and data used during this research. Chapter 3 investigates long-term wind data from Environment and Climate Change Canada (ECCC) stations surrounding the Cariboo Mountains, in an attempt to define the wind seasons of the region. Chapter 4 investigates the synoptic forcing for episodes of strong wind stress, observed at lake-level. From the

most recent summer field campaign (summer 2018), Chapter 5 investigates the spatial and temporal variability of wind during August to October, from five stations located around Quesnel Lake. Finally, Chapter 6 provides the overall conclusions and an outlook for future meteorological research at Quesnel Lake.

1.3 Literature review

1.3.1 The atmosphere-water interface

Wind affects the physical state of a body of water when the transfer of momentum occurs between the atmosphere and surface. This exchange is via an interfacial stress, commonly known as the surface shear stress (henceforth 'wind stress') (Donelan et al., 2004). The quantification of this mechanism has been studied on a variety of scales, from investigations of flow in the aqueous surface sub-layer (i.e., molecular friction) (Banner and Peirson, 1998), to research into the strength of wind-driven storm surge forcing beneath hurricanes (Bryant and Akbar, 2016). On a global scale, an atlas by Hellerman and Rosenstein (1983) quantified monthly averaged wind stress over the world's oceans.

A set of standard equations from popular boundary layer textbooks (e.g., Oke, 1987; Garratt, 1992) are used extensively in the literature (Falconer et al., 1991, see also Agrawal et al., 1992; Gardner et al., 2006). Wind stress (τ) is parametrized from wind speed measurements as

$$\tau = \rho_a C_D (U_{10})^2, \tag{1.1}$$

where U_{10} is the wind speed at a height of 10 meters above the surface, ρ_a is air density, and C_D is a (dimensionless) drag coefficient. This latter variable is a function of wind speed, surface roughness, ABL stability, and friction velocity (the velocity scale for turbulence

created by wind shear near the ground). Empirical values for C_D are provided by look-up tables that account for a variety of underlying surface types given a stable ABL and a constant friction velocity (Stull, 1988).

A topographical factor influencing wind stress is the transition of an internal boundary layer (IBL) across a surface delineation. This is observed at the edge of a lake whereby a wind blowing from land to water will experience a reduction in surface roughness and speed up due to the decreased friction. This acceleration in flow results in divergence of the wind field downstream from the shoreline (Oke, 1987). Examples of this were seen by Valerio et al. (2017), where shore-based meteorological stations underestimated on-lake wind conditions considerably. When modelling circulations in Clear Lake, Rueda et al. (2005) observed patterns that would not have arisen if the flow had been modelled with a uniform wind field. Both of these examples show the necessity to consider the spatial variability of winds within a lake basin (see also Laval et al., 2003; Józsa, 2014).

In addition to equation (1.1), wind climatologies authored by the wind energy community focus on measurements of wind power, P, using

$$P = \tau(U_{10}) = \rho_a \, C_D \, (U_{10})^3. \tag{1.2}$$

When investigating seiche activity in Lake Iseo, however, Valerio et al. (2017) note that equation (1.2) underestimates the amount of energy exchange between the ABL and the water surface. Therefore, following from Hellerman and Rosenstein (1983) and Wüest et al. (2000), equation (1.3) can be used to estimate the rate of turbulent kinetic energy production in the surface layer of a lake, E, by integrating the amount of shear stress that is imparted to the surface layer, over area A by

$$E = \int_A \frac{1}{\rho_w} P\, C_U\, C_S \, \mathrm{d}A = \int_A \frac{\rho_a}{\rho_w} C_D\, (U_{10})^3\, C_U\, C_S \;\, \mathrm{d}A. \tag{1.3}$$

Here ρ_w represents the density of water and C_U and C_S are empirical constants describing the fraction of wind stress and energy that is available for transfer from the air to the sub-surface water column. Since turbulent kinetic energy dissipates by mechanisms other than direct exchange with the surface, these constants are usually less than unity (Findikakis and Law, 1999).

Despite having equations (1.1), (1.2), and (1.3), common practice is to use U^2 and U^3 (where U represents the measured wind speed) as proxies for wind stress and wind power, respectively (Horn et al., 1986; Stevens et al., 1996; Valerio et al., 2017). Note the averaging of temporal data will result in an under-estimation of the proxy wind stress (or wind power) value if wind speed data are raised to the second (or third) power after filtering (Hellerman and Rosenstein, 1983). Therefore, datasets of U^2 and/or U^3 should be constructed from raw wind speeds before any filtering is performed.

1.3.2 Wind-forced seiching

Wind-forcing applied to bodies of water permeates various aspects of science and engineering. Wave fields in ocean waters (Donelan et al., 2004), seiche activity in South American fjords (Castillo et al., 2017), and potential reversal of river delta flow (Gardner et al., 2006) are all examples of wind-forced phenomena. However, to maintain relevance to the Quesnel Lake spill, and due to the possibility of sediment re-suspension as observed in similar studies (Shteinman et al., 1997; Jordi et al., 2008), I shall focus on the topic of basin-scale seiche.

The basic mechanism that initiates a wind-forced seiche response in a lake is the piling of

surface water towards the downwind end of the basin by persistent winds. If the lake is thermally stratified (using a two-layer density stratification approximation) the additional water mass at the downwind end will force a downwards tilt to the thermocline until the slope of the thermocline equilibrates with the wind forcing (assuming a steady state wind) (Spigel and Imberger, 1980). This initial set-up is followed by a lull (a reduction in wind speed) in the wind field which allows an oscillatory response of the thermocline, which is known as a baroclinic, or internal, seiche (see Spigel and Imberger, 1980; Antenucci and Imberger, 2003). The duration for the wind to act upon the lake for the thermocline to first reach the required equilibrium tilt has been shown by Spigel and Imberger (1980) to be one quarter of the fundamental seiche period of the basin, $(T/4)$. For Quesnel Lake, this requires winds to be of sufficient strength for $\sim$1.5 days along the thalweg of the lake during the summer months when the lake is thermally stratified (Laval et al., 2008). If this duration of forcing is not met then a basin-scale response will not occur.

Seiche events may also arise from tsunamis (Abraham, 1997), surface waves (Okihiro et al., 1993), pressure disturbances (Rabinovich and Monserrat, 1998), glacier lake outburst floods (Castillo et al., 2017), or other possible mechanisms outlined by Brenner (2017). However, studies of wind-forced internal seiching in lakes began in Scotland as early as 1904 by Maclagan-Wedderburn (1904) (also see Spigel and Imberger, 1980). More recently, this body of research includes Hodges et al. (2000) who modelled wind-driven hydrodynamics in Lake Burragorang (Australia), and investigations on Lake Como (Italy) by Shintani et al. (2010). Both of these later studies relate to Quesnel Lake due to the similarities in basin depth and complexity (Brenner, 2017).

Examples of lakes close to central BC that exhibit similar baroclinic responses are Babine Lake, and the Nechako Reservoir. Situated 400 km northwest of Quesnel Lake, Babine Lake is similarly long, narrow, and surrounded by steep topography. Deflections of the

thermocline during summer in the southern portion of Babine Lake have been attributed to along-channel westerly winds (Farmer, 1978). The Nechako Reservoir also initially responds to wind forcing in a similar manner, yet the resulting oscillations are strongly damped, as outlined by Imam et al. (2013). This dampening reduces the basin-scale free oscillations in the reservoir compared to observations in Quesnel Lake.

1.3.3 Previous wind climate research

The subject of wind climate research covers a broad spectrum of interests. Klink (2002) notes that topics include bird migration, power potential, particulate dispersion, and forecast model validation. Examples of wind research in the early part of the 20th century are provided by the work of mathematicians such as Taylor (1916) and Richardson (1920). These studies were usually focused on methods to specify many of the physical parameters describing turbulence in the ABL. Thorough surveys of this research and further progressions in the field of boundary layer meteorology are now available as texts by Oke (1987), Stull (1988), and Garratt (1992); all of which are invaluable to students of meteorology.

Through the 1900's into the 2000's, these parametrizations continued to be refined. LeHau (1959) investigated wind profiles and surface stress in the ABL, while Tuller and Brett (1984) looked at the characteristics of wind that allow the fitting of a Weibull distribution curve (also see Garcia et al., 1998; Seguro and Lambert, 2000; Lun and Lam, 2000).

Wind climatologies have also focused on other wind-forced phenomena. The effect of wind over the open Arctic Ocean in summer has been shown to play an important role in coastal erosion observed near Canada's northern communities (Small et al., 2011); while Déry et al. (2010) focused on wind-transported snow as a hydrometeorological driver in the Cariboo Mountains of BC.

A major theme increasingly contributing to wind climate research is the use of wind energy as a renewable resource. Wind energy research now encompasses a complete body of literature itself. Petersen et al. (1998) note that wind power studies often include aspects of engineering, meteorology, climatology, and physical geography. Some avenues of research include the use of numerical models to forecast regional wind power (Jimenez and Dudhia, 2013), and spatially-broad wind power climatologies such as the European wind atlas by Petersen (1993).

Due to the potentially destructive nature of strong wind events, extreme winds have had, and will no doubt continue to have, special interest from meteorologists and climatologists. A climatology of strong winds associated with winter storms in Germany was the focus for Hofherr and Kunz (2010); while Kuo et al. (1995) explored the effects of wind during a single storm event on a long-span suspension bridge in Norway. Chenoli et al. (2013) identified the dominant synoptic patterns and their connection to large scale ocean-atmosphere oscillations in their climatology of strong wind events in Antarctica.

Within this breadth of wind climate research, a number of studies are notably relevant to a wind climatology of Quesnel Lake:

Klink (1999) used 216 stations across the continental United States to examine patterns in wind speed and direction. In the western United States wind speeds were highest during summer, and lowest during winter. Strong orographic channelling by the Rocky Mountains resulted in less variance in wind speeds in the western states compared to the eastern states. This topographic effect also prevented any spatially coherent pattern in wind direction seasonality from appearing in the western states compared to east of the Rockies.

On Canada's West Coast, Tuller (2004) investigated wind data from four coastal ECCC stations for the period 1945-1995. He found a decreasing trend in wind speeds over the

length of their timeseries. The trend was not consistent but strongest during 1970-1990. The decrease in mean wind speed was largely influenced by an increase in the percentage of calms observed. An analysis of the influence of large-scale atmosphere-ocean oscillations was also performed, thereby identifying changes in surface pressure patterns that accounted for the observed changes in wind speeds.

A Canada-wide study of wind speed data obtained from 117 ECCC stations during 1953-2006 was undertaken by Wan et al. (2010). Important conclusions include a significant decrease in wind speeds over western Canada, and the interior of BC being identified as the least windy location in Canada. Inter-annual variability in wind speeds over the West Coast of BC was maximal in autumn and winter, and minimal in summer.

The decease in mean surface wind speeds observed by the previous two studies is also reflected in work by Menounos et al. (2019), who partially attribute glacial-mass loss in BC to a reduction in 250 hPa zonal winds. A southward shift in jet stream is implicated for the decrease in moisture-laden mid-latitude cyclones, however, this would also reduce the frequency of peak wind speed events and lower the overall mean.

In the St. Lawrence River Valley (SLRV), Carrera et al. (2009) engage with the problem of wind channelling, defined as the occurrence of wind blowing near-parallel to the axis of a valley irrespective of the wind direction above ridge height (also see Eckman, 1998). Despite geometrical differences between Quesnel Lake and the SLRV (the SLRV is up to 90 km wide at points), the problem of resolving this channelled flow is similar in both locations. The authors used reanalysis data for the 925 hPa geopotential height field to derive above-ridge geostrophic winds. These were used in conjunction with surface weather observations to investigate directional differences in the near-surface and free-atmosphere wind fields.

As Carrera et al. (2009) note, the problem of channelled flow in a valley or basin is also similar to gap-winds. These winds can be caused by differences in atmospheric pressure on either side of a gap in topography, creating wind conditions specific to the site of the gap. Bakri et al. (2017a) created a synoptic climatology of gap-winds observed in Howe Sound, BC. They differentiated episodes depending on the direction of flow (inflow vs outflow), and compiled composites of synoptic conditions that led to the required pressure gradient patterns. Finally, Bakri et al. (2017a) employed a non-hierarchical clustering analysis method (k-means clustering) to differentiate between synoptic patterns where manual classification and compositing could not.

2 Data Sources

In each of Chapters 3, 4, and 5, details of the dataset used for each analysis is provided, with temporal and spatial resolutions being specified where appropriate. However, to reduce repetition throughout the text, this section provides an overview of the study area and the various data-sources. This outline is supplemented by Tables 1, 2, and 3.

2.1 The study area

2.1.1 The Cariboo Mountains

The Cariboo Mountains occupy 7,700 km^2 of central British Columbia (BC), Canada, forming the northern end of the Columbia Mountains (Sharma and Déry, 2016). The climate of the Cariboo Mountains has previously been categorized as transitional by Beedle et al. (2015), as they are drier than the Coast Mountains to the west, and wetter than the Rocky Mountains to the east (Sharma and Déry, 2016). Elevations range from 330 metres above sea level (masl), to 3520 masl. Throughout the text, I will use the boundaries and terminology of the *Cariboo Mountains Region* (CMR) as identified by Sharma and Déry (2016) (Fig. 2.1.2). The numerous habitats contained within this environment provide researchers with unique region-specific opportunities. Examples include previous studies of lacustrine sediments in Horsefly River (Wilson, 1977), and the recession of Cariboo Mountain glaciers (Beedle et al., 2015). Other research has more of a universal application, such as work by Radic et al. (2017) resolving near surface turbulent fluxes over glacial ice. Of interest to biologists are the opportunities to observe populations of keystone species such as mountain caribou (Edwards, 1954), and sockeye salmon (Stockner and Shortreed, 1983), in such pristine environments.

Situated within the CMR boundary is the 12,000 km^2 Quesnel River watershed, which

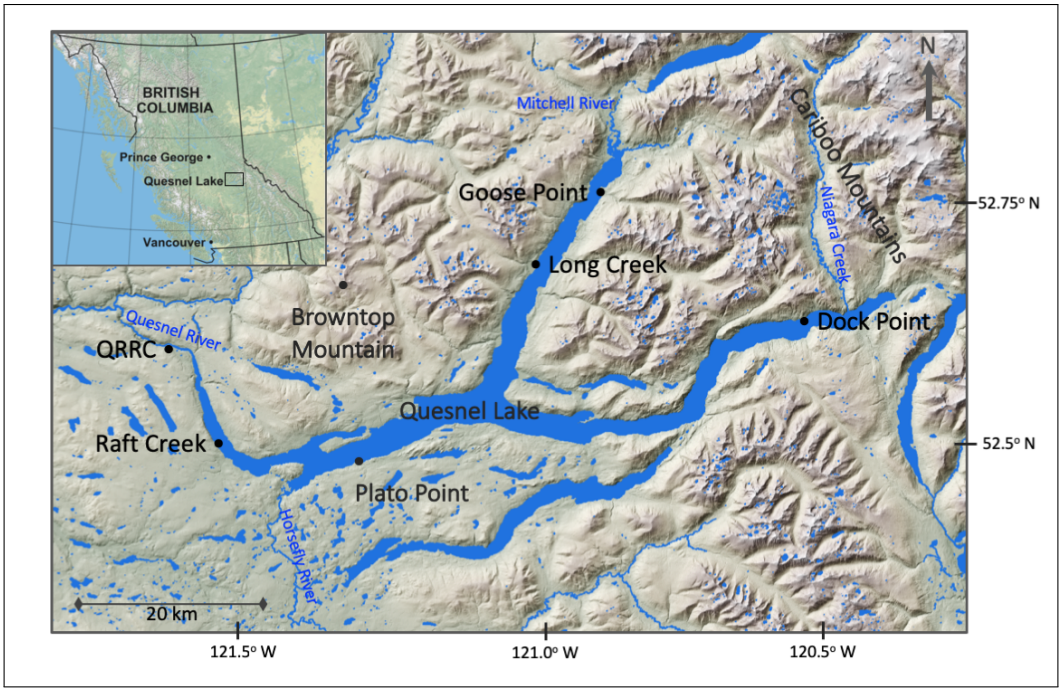

Figure 2.1.1: Quesnel Lake and the western flank of the Cariboo Mountains. Labelled are the active CAMnet meteorological stations in the immediate vicinity of Quesnel Lake that have been utilized throughout this study. Also labelled is the location of the Quesnel River Research Station (QRRC) and the major rivers mentioned in Section 2.1.2. Inset: The location of Quesnel Lake within BC, Canada

drains into the Fraser River at Quesnel (see Sharma and Déry, 2016). Early literature for the CMR is dominated by research examining salmon ecology (Ricker, 1947; Scrivener et al., 1994), and the effects of river dam projects on various salmonid species (e.g., Andrew and Geen, 1960); studies which were driven by industrialization of the region's natural resources. Even though climatology studies are less abundant, the CMR has been ideal for investigations of hydrometeorological drivers such as research by Déry et al. (2010) investigating the effect of blowing snow on glacial mass balance (also see Burford et al., 2009; Leggat et al., 2015; Radic et al., 2017). The continuing mass balance measurements of the Castle Creek Glacier (see Beedle et al., 2009), and the establishment of the Cariboo Alpine Mesonet (CAMnet) array of climate stations in and around the Cariboo Mountains (Hernández-Henríquez et al., 2018), have made notable contributions to hy-

drological, glaciological, and meteorological datasets of the region. The latter being directly relevant as data from select CAMnet stations have been used extensively in my research. However, the general wind patterns and seasonality of winds affecting the CMR are poorly understood; they are usually simplified by citing the band of prevailing westerlies commonly seen throughout the mid-latitudes of the northern-hemisphere (e.g., Sharma and Déry, 2016).

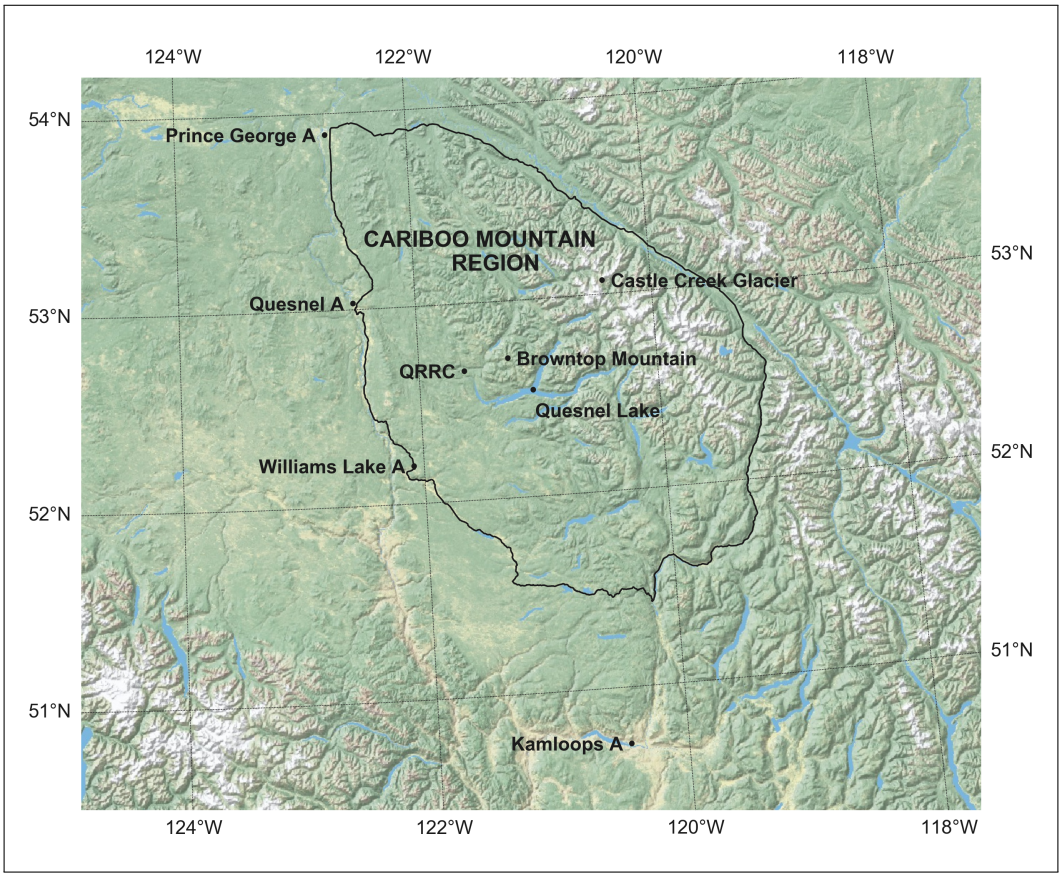

Figure 2.1.2: ECCC stations proximal to the Cariboo Mountain Region (CMR), labelled by their official ECCC designation (the A standing for 'Airport'). The outline of the CMR defined by Sharma and Déry (2016) is denoted by the black trace. Also labelled are the locations of Browntop Mountain, Castle Creek Glacier, Quesnel Lake, and the Quesnel River Research Centre (QRRC)

2.1.2 Quesnel Lake

Nestled in the western slopes of the Cariboo Mountains, 185 km south-east of Prince George, Quesnel Lake is a deep, fjord-type, oligotrophic lake (Laval et al., 2012). The three glacial-scoured arms of Quesnel Lake span 121°34′22″ W to 120°20′45″ W in longitude, and 52°27′46″ N to 52°46′51″ N in latitude. These coordinates correspond to dimensions of 83 km east-west, and 35 km north-south. Three major inflows, Horsefly River, the Mitchell River, and Niagara Creek, drain a surrounding watershed of 5930 km^2 (Potts, 2004). A mean width of 2.7 km, together with the lake's eastern portion being flanked by the Cariboo Mountains, results in the lake being partly surrounded by complex topography, which has the potential to cause local wind flow phenomena seen in similar terrain by Valerio et al. (2017). This can include the channelling of flow, lee-side separation, and valley breeze circulations. The intersecting arms and geometry of the basin make it a complex yet interesting location to study meteorological phenomena, such as the near-surface wind field.

Limnology studies within BC's deepest lake have been well reviewed by Potts (2004), who investigated the heat budget of Quesnel Lake. Other areas of research include the lake's salmon nursery habitat (Stockner and Shortreed, 1983), lake-surface temperature estimations (Sentlinger et al., 2008), and barotropic seiching in basins with complex bathymetry (Brenner, 2017). However, the Mount Polley spill generates the incentive for further investigations of the lake's physical processes, especially the mechanisms of sediment mixing and re-suspension. An opportunity exists to further the study of wind-forced baroclinic seiching as outlined by Laval et al. (2008), therefore a wind-climatology of Quesnel Lake and the surrounding CMR will contribute to a better understanding of the forcing associated with such episodes.

2.2 Near-surface wind data

The primary instrument used for wind data collection is the cup or propeller anemometer, used in conjunction with a wind vane. Although more advanced instrumentation exists, similar research to this project has succeeded with temporal resolutions ranging from ten minutes to one day, proving the high resolution data (e.g., 20 Hz) of a sonic anemometer to be inconsequential. Wind measurements and instrumentation are covered in detail by *The Weather Observer's Handbook* (Burt, 2012). For the operating procedures used by ECCC, I point the reader to the *Manual of Surface Weather Observations* (Meteorological Service of Canada, 2015). CAMnet stations in the CMR are erected and managed as close to these industry standards as possible, yet occasionally environmental factors and operational conflicts result in deviations from such guidelines (see Hernández-Henríquez et al. (2018)).

2.2.1 Local meteorological stations

The Northern Hydrometeorology Group (NHG), a weather and climate research group based at the University of Northern British Columbia (UNBC), began the installation of the CAMnet array of meteorological stations in 2006 (Hernández-Henríquez et al., 2018). As of October 2018 there are 15 stations in operation, seven of which are utilized in this study (see Figure 2.1.1, and Tables 1 and 2). These use propeller anemometers and wind vanes to record mean wind speed and direction every 15 minutes. The array covers a large elevation range, with lake-level stations at $\sim$ 728 masl contrasted with the station near the summit of Browntop Mountain at 2031 masl. A primary motivation for expanding the network since 2016 has been to contribute wind data from sites around Quesnel Lake to this wind climatology study, and to any future research and modelling.

Weather observations recorded to the standards of the World Meteorological Organisation

Table 1: Meteorological station metadata

Station name	Managed by:	Lat (N)	Lon (W)	Elevation (masl)	Anemometer height (m)
Browntop Mountain	NHG	52°42′28″	121°20′24″	2031	2.4
Plato Point	NHG	52°29′14″	121°17′03″	728	2.7
Long Creek	NHG	52°40′07″	120°57′34″	728	3.2
Dock Point	NHG	52°35′48″	120°30′03″	728	2.4
Goose Point	NHG	52°45′13″	120°50′04″	728	3.1
Raft Creek	NHG	52°30′34″	121°30′46″	728	2.8
Williams Lake A	ECCC	52°10′59″	122°03′15″	939	10.0
Prince George A	ECCC	53°53′27″	122°40′44″	691	10.0
Quesnel A	ECCC	53°01′34″	122°30′36″	545	10.0
Kamloops A	ECCC	50°42′08″	120°26′31″	345	10.0

Note: ECCC stations are named as per their ECCC designation

Table 2: CAMnet station data

Station name	Operating period	Temporal resolution
Raft Creek	Aug 2018 - present	15 min
Plato Point	Aug 2016 - present	15 min
Long Creek	Jun 2017 - present	15 min
Goose Point	Aug 2018 - present	15 min
Dock Point	Jun 2018 - present	15 min
Browntop Mountain	Aug 2006 - present	15 min

(WMO) are collected at ECCC stations in many metropolitan areas in BC. Often these locations are at airports or aerodromes. I have used data from four such sites bordering the CMR: Prince George, Quesnel, Williams Lake, and Kamloops (see Figure 2.1.2, and Tables 1 and 3). Wind data used in this study are hourly recordings in kilometres per hour (km hr^{-1}), taken from a 2 minute average on the hour. Anemometer types are either a U2A cup anemometer and wind vane, or a 78D anemometer (which is essentially a digitized U2A system), mounted on a 10 metre tower. Wan et al. (2010) provide a comprehensive overview of the history of ECCC wind data recording and current operating

procedures. Extrapolating these long-term data to predict wind conditions within the CMR is difficult, due to the spatially variable nature of wind and the strong effect topography and boundary layer stability have on the near-surface wind field (Stull, 1988). However, I have considered an analysis of data from these four ECCC stations to be the most appropriate method to estimate the climatological values and any long-term trends in wind data for the CMR due to their proximity to the study area and the length of the datasets available. Data for ECCC stations are accessed via the ECCC *Historical Data* webpage (http://climate.weather.gc.ca/historical_data) (Government of Canada, 2017).

Table 3: ECCC station hourly data

Station name	Climate ID	Operating period	Longest homogeneous period
Kamloops A	1163780	Jan 1953 - present	Jan 1953 - Jun 2013
Williams Lake A	1098940	Jan 1961 - present	Jan 1961 - Dec 2012
Quesnel A	1096630	Jan 1953 - present	Jan 1953 - Feb 2006
Prince George A	1096450	Jan 1953 - present	Jan 1953 - Oct 2009

Climate IDs are the unique identifiers for each station assigned by ECCC

Data from a meteorological tower at the Likely Aerodrome (52°36′05″ N, 121°30′48″ W, 1046 masl), situated near the QRRC, was supplied by the BC Forest Service for the years 1991 to 2016. However, due to icing of the anemometer during winter months (see section 2.2.3) the dataset has large temporal gaps and was not of sufficient quality for use in this study. Hourly data from the ECCC station in Blue River (Blue River A, 52°07′44″ N, 119°17′22″ W, 690 masl) was also initially included for analysis. However, due to 14% of the dataset being null entries, in particular during the early 2000's (some months were missing up to 54% of hourly values), the dataset was also abandoned from this study.

2.2.2 Accuracy of instruments

RM Young propeller anemometers used at the majority of CAMnet sites have a wind speed accuracy of $\pm$ 0.3 m s^{-1}, or 1% of the reading, whichever is greater. The direction recorded by these instruments is accurate to $\pm$ 3° (Campbell Scientific, 2017). HOBO weather stations are used at CAMnet's Dock Point, Goose Point, and Raft Creek sites. These three-cup anemometers have a wind speed accuracy of $\pm$ 1.1 m s^{-1}, or 4% of the reading, and the direction recorded by these instruments is accurate to $\pm$ 5° (Onset computer corporation, 2017). The U2A and 78D anemometer systems used at ECCC stations report wind speed to the nearest statute mile per hour (mile hr^{-1}), which is then converted into the nearest kilometre per hour (km hr^{-1}) for data archiving (Wan et al., 2010). This results in an accuracy of $\pm$1.3 km hr^{-1}. Due to the method of reporting wind directions in 10's of degrees (i.e., 130° is recorded as 13), direction at these stations are accurate to $\pm$ 5° (Meteorological Service of Canada, 2015). The precision of ECCC wind data is therefore a result of the reporting method and irrespective of the accuracy of the equipment, which is not stated in any available literature.

2.2.3 Quality control

The quality control process begins with the filtering of data within reasonable values. Wind directions are constrained to values between 0° and 360°. Wind speeds must be greater than 0.0 m s^{-1} or km hr^{-1}, but the upper limit depends on the station's site, which required a preliminary analysis of the data. Other meteorological parameters (e.g., station pressure, wind direction, temperature/humidity) can be used to verify extraordinarily high wind speeds, where the passage of a storm or frontal system may be evident. No outliers in the data were identified, or therefore excluded. Missing values have been left as NANs. The degree of inaccuracy in interpolating between known data points outweighs any advantage gained

by including what could be an erroneous value. Periodic station checks at CAMnet sites throughout the study period assist in ensuring there is no external influence on recording of wind data (e.g., encroaching tree branches or tilting of the station).

Figure 2.2.1: Meteorological station at Plato Point, Quesnel Lake (facing north). Image courtesy of Stephen Déry (2016)

Occasionally, inconsistencies in wind data are due to external mechanisms. An example of this is data from Browntop Mountain, where the station's anemometer had been accidentally rotated during a station visit in 2012. This equipment fault was corrected during a site inspection in the summer of 2017. The four years (11 Aug 2012 - 26 Jun 2017) of erroneous wind direction values have been revised by rotating the wind vector clockwise by 140°. This is an example why it is important to keep good metadata records and

photographic evidence (Hernández-Henríquez et al., 2018).

Finally, two reasons that a station may have missing values for extended periods of time are:

1. Power failure of the weather station's battery/solar panel system, causing the data-logger to stop recording values. (An anemometer is self-energized, but requires a powered unit to interpret the voltage readings and to record the data.)

2. Ice accretion on the anemometer during sub-freezing periods can reduce wind speed values, sometimes down to 0.0 m s^{-1}. Ice loading will also reduce wind vane movement, corrupting wind direction recordings; therefore a heavily rimed or iced station may produce inaccurate wind data during winter months, until a thaw occurs (Meteorological Service of Canada, 2015).

Both of these complications predominantly occur at stations in wilderness environments, where site visits and inspections are sporadic or rare in the winter months.

3 Wind Seasonality

3.1 Introduction

Wind climate research is becoming more extensive due to the increase in wind-power generation and resource management (Petersen, 1993; Lavagnini et al., 2006; Greene et al., 2010). Investigators that subjectively choose to include seasonality in their wind climate analysis, commonly do so using pre-defined periods of the year. Examples include Bakri et al. (2017b) using summer as June to August and winter as December to February, excluding all other months due to their transitional nature. This is in contrast to Tuller (2004) who covers all periods of the year by using spring: March to May; summer: June to August; autumn: September to November; and winter: December to February. This approach is also popular in other climatology research that focuses on temperature and precipitation (e.g., Sharma and Déry, 2016). In previous limnology research Gardner et al. (2006) limited their analysis to the open-water season of Great Slave Lake, due to the reduction of wind-forcing when the water body was ice-covered. Although appropriate for that location, I will attempt to provide a year-round climatology for Quesnel Lake that includes the winter months.

Long-term wind data (25 years) obtained from stations bordering the CMR will be used to infer the wind seasons of the area, by identifying months that are either above or below the mean annual wind speed. There is precedence for assuming that a seasonality may exist in wind data from a particular site: this has been shown for the Isthmus of Tehuantepec in Mexico, by Romero-Centeno et al. (2003), and over a large portion of the United Arab Emirates by Naizghi and Ouarda (2017).

A comparison of the long-term ECCC mean with data from two CAMnet stations within the CMR will be performed. This will be used to infer if a seasonal signal is also present

at the mountainous locations.

3.2 Data

Data were obtained from four ECCC stations listed in Tables 1 and 3. Overlapping periods of continuous data in the ECCC datasets are limited due to changes in the station location or ownership. Even within seemingly continuous datasets, Wan et al. (2010) identified inhomogeneities due to tower height adjustments, changes in instrumentation, and even shifts in recording methods (e.g., the change from a 1-min mean to 2-min mean in 1996). Since the purpose of using the ECCC long-term data is to analyze if a seasonality exists, the resolving of potential discontinuities is not attempted here.

The primary consideration for using the long-term ECCC data is to avoid any inter-annual variability in the CAMnet data biasing a seasonal signal, as the CAMnet stations have datasets that cover a shorter time-span (see Tables 2 and 3). Secondly, the lake-level stations are prone to anemometer icing during late fall and winter, therefore such long-term continuous datasets are difficult to obtain in wilderness environments.

From a potential 219,000 hourly observations, Williams Lake A, Prince George A, and Kamloops A were missing less than 1% of hourly observations. Quesnel A was missing 9.4% (20,694 observations) spread sporadically throughout the timeseries. Days with at least 10 hourly wind speed and direction observations were averaged to create a dataset of mean daily values. This approach was to ensure that daily values were based on sufficient data. Although the subjectively chosen amount of 10 hourly values appears arbitrary, it is more stringent than the minimum amount of 3 hourly observations used by Wan et al. (2010). This approach resulted in both Prince George A and Quesnel A missing 5 days of data, while all other stations had a continuous daily record. Monthly averages of wind speed and direction were then derived from the daily datasets. All months contained at

least 25 days of observations, which I considered to be sufficient for this study.

3.3 Methods

3.3.1 Wind data statistics

To begin understanding the nature of the CMR wind climate, the mean, standard deviation, and coefficient of variation values for wind speeds were calculated from the monthly datasets. The mean and standard deviation values for wind directions were calculated from the monthly datasets using circular statistics. Histograms of the wind speed distributions were constructed for each station using 1 km hr^{-1} wind speed bins. Windroses using 2 km hr^{-1} wind speed bins and 16 directional bins (covering 22.5° per bin) were produced to show the relationship between wind speed and direction at each location (Fig 3.4.1). Note the averaging of wind speed values first by day then by month results in the absence of calms and produces smoothed distributions and windroses that somewhat distort the actual wind conditions that may be experienced at each site.s center hours

Monthly wind speed values were plotted, and a linear regression trend analysis performed for each of the four ECCC stations. Although variations of the Mann-Kendall trend analysis are popular in hydrometeorology, Naizghi and Ouarda (2017) used both linear regression and a modified Mann-Kendall test and found that they each gave similar results when examining long-term wind data. I have used a probability value (p-value) threshold of 0.05 to test for the statistical significance of the linear regression trend.

Note that many similar studies have analyzed the scale (C) and shape (k) parameters of the Weibull distribution (of wind speeds), rather than the mean and the standard deviation (Tuller and Brett, 1984; Lun and Lam, 2000; Gryning et al., 2016). Despite wind speed data often fitting a Weibull distribution, I found that if the distribution of values does not con-

form to a Weibull distribution then nonsensical parameter values were returned, meaning any conclusions from such an analysis would have been incorrect. These false parameter values were observed when stations experienced calm conditions and had numerous recordings of 0.0 km hr^{-1}(i.e., any recording below the anemometer cutoff speed of 1.5 km hr^{-1}). The return of incorrect Weibull distribution parameters occurred in up to 25% of the time for some datasets (75 out of 300 months for the Quesnel A station). Therefore, an analysis of C values was discarded and mean and standard deviation values were used to analyze the long term trends in the ECCC data.

3.3.2 Creating a monthly climatology timeseries

Each monthly wind speed timeseries was detrended by removing the magnitude of the trend identified in Table 5. The mean and standard deviation for each month of the year during the 25-year period was then calculated, providing a 12-month (January to December) climatology for each station (Fig. 3.4.3). The climatology values were standardized to produce a final 12-month (January to December) detrended, standardized timeseries. The final datasets have a mean of zero and standard deviation of one, derived for each month of the year using:

$$U = \frac{u - \bar{u}}{\sigma}, \tag{3.1}$$

where U is the new detrended, standardized climatology value, u is the pre-standardized climatology value, $\bar{u}$ is the mean of the 12 monthly climatology values, and σ is the standard deviation of the 12 monthly climatology values.

3.3.3 Seasonality in the climatology values

To compare the seasonal signal present at each station, the final standardized climatology datasets were plotted to view the occurrence of positive and negative wind speed anomalies. A covariance matrix was constructed to investigate how the seasonal signal at each station varies throughout the year compared with the other three locations. A value of 1 indicates two samples that vary at the same time in the same direction, -1 indicates variance at the same time but in the opposite direction (i.e., opposite sign), and a value of 0 indicates the samples do not vary together in time at all.

Months above and below the annual mean were identified as *active* and *calm* months, respectively. The original monthly timeseries (i.e., the data before the detrending and standardization was performed) was partitioned into these active and calm months, then analyzed using boxplots, windroses, and descriptive statistics. The Mann-Whitney U test, a Python implementation of the Wilcoxon-Mann-Whitney test, is a non-parametric rank-sum test that indicates if there is a statistically significant difference between the means of two samples, with the null hypothesis being that both samples are drawn from the same distribution. A strength of this test is that the samples do not have to be the same size (but should have a minimum of 20 observations) (Wilks, 2011). This test was performed to investigate if the mean wind speeds during calm months were different than during active months at each station.

3.3.4 Comparison to CAMnet data

Finally, 12 months of data from two CAMnet stations (Plato Point and Browntop Mountain, Tables 1 and 2) were obtained for the period 1 October 2016 to 30 September 2017. Mean daily values were derived from the original 15-minute timeseries, then averaged over each month and standardized to create a 12-month dataset in the same form as the ECCC

climatology values. The CAMnet data were then plotted against the mean of the ECCC climatology values, and a covariance matrix constructed to compare the seasonal signal.

3.4 Results

3.4.1 The general wind climate

Descriptive statistics for the 25-year period are provided for the four ECCC stations (Table 4 and Fig. 3.4.1). Mean wind speeds range from 6.2 km hr^{-1} at Quesnel A to 10.2 km hr^{-1} at Kamloops A. The standard deviation in wind speeds is greatest at Williams Lake A at 2.6 km $hr^{-1}$and lowest at Quesnel A with a value of 1.8 km hr^{-1}. However, the standard deviation of wind speed is typically weighted by the mean wind speed, and therefore a better indicator of the variability in wind speed is provided by the coefficient of variation (CV) (Wilks, 2011). The CV is defined as the ratio of the standard deviation to the mean. The range of CV values is small (0.23 to 0.28), but they exhibit an inverse correlation to the mean wind speed across the four stations (Table 4).

Table 4: Descriptive statistics of mean monthly wind data from four ECCC stations bordering the Cariboo Mountain Region for the period 1981 to 2005

Station	Mean wind speed (km hr^{-1})	Wind speed σ (km hr^{-1})	Wind speed CV	Mean wind direction (degrees)	Wind direction σ (degrees)
Kamloops A	10.18	2.36	0.23	138.0	43.3
Williams Lake A	9.79	2.61	0.27	158.7	70.0
Quesnel A	6.24	1.78	0.28	194.0	88.6
Prince George A	9.42	2.30	0.24	218.4	54.0

Wind directions have little variation across the four stations, with all sites experiencing a mean wind direction with a strong southerly influence (Fig. 3.4.1). Mean monthly wind directions range from 138.0° ($\sim$ southeasterly) at Kamloops A to 218.4° ($\sim$ southwesterly)

at Prince George A (Table 4). The variability in wind direction (the circular standard deviation) is not influenced by the mean direction, but is inversely proportional to the mean wind speed observed at each station. This is shown by the standard deviation in wind direction ranges from 43.3° at Kamloops A to 88.6° at Quesnel A.

The linear regression trend analysis for mean monthly wind speeds shows only Kamloops A to have a significant increasing trend over the 25-year period (Fig. 3.4.2). Prince George A also displays an increasing, yet not statistically significant, trend, while Williams Lake A and Quesnel A both have non-significant decreasing trends (Table 5).

These trends are in contrast to previous studies using long-term monthly wind data in western Canada, where a significant decrease in mean wind speeds has been observed (Tuller and Brett, 1984; Wan et al., 2010). However, differences include the shorter timeseries used in this analysis, and the lack of correction for possible discontinuities especially when compared to Wan et al. (2010). Note Tuller (2004) did not perform any data homogenization or corrections. The exploration of these trends (or lack thereof) is beyond the scope of this text, where long-term ECCC data are being leveraged to infer the wind seasons of the CMR.

Table 5: Long-term trends in mean monthly wind speeds at ECCC stations

Station	Change per decade (km hr^{-1})	Overall change (km hr^{-1})
Kamloops A	**0.366**	**0.914**
Williams Lake A	-0.373	-0.933
Quesnel A	-0.166	-0.416
Prince George A	0.053	0.132

Bold text indicates significance at $p < 0.05$

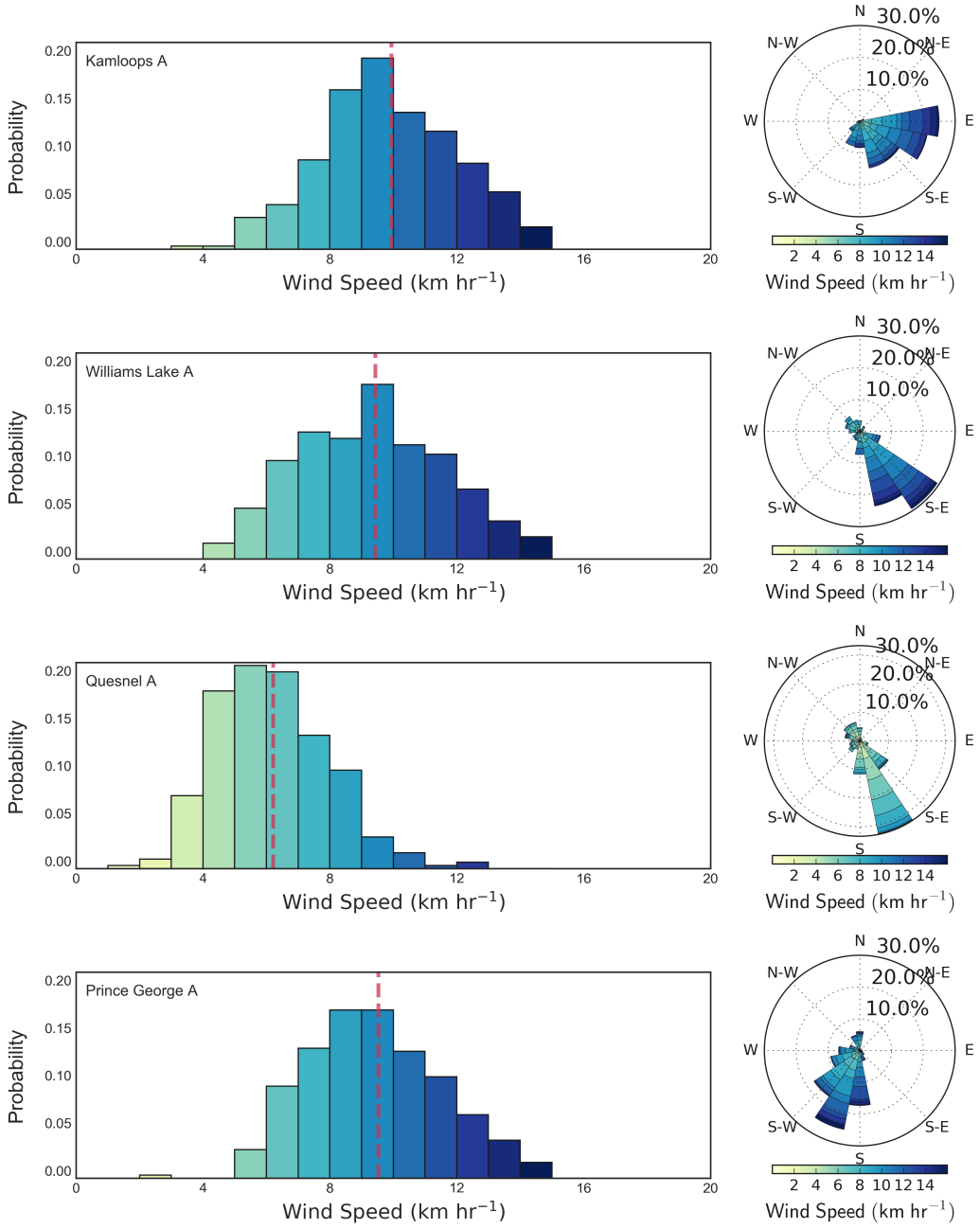

Figure 3.4.1: Mean monthly wind speed distributions (left) and mean monthly wind speed and direction windroses (right) from four ECCC stations bordering the Cariboo Mountain Region for the period 1981-2005. n = 300 for each station. The dashed red line in each histogram (left) indicates the mean wind speed

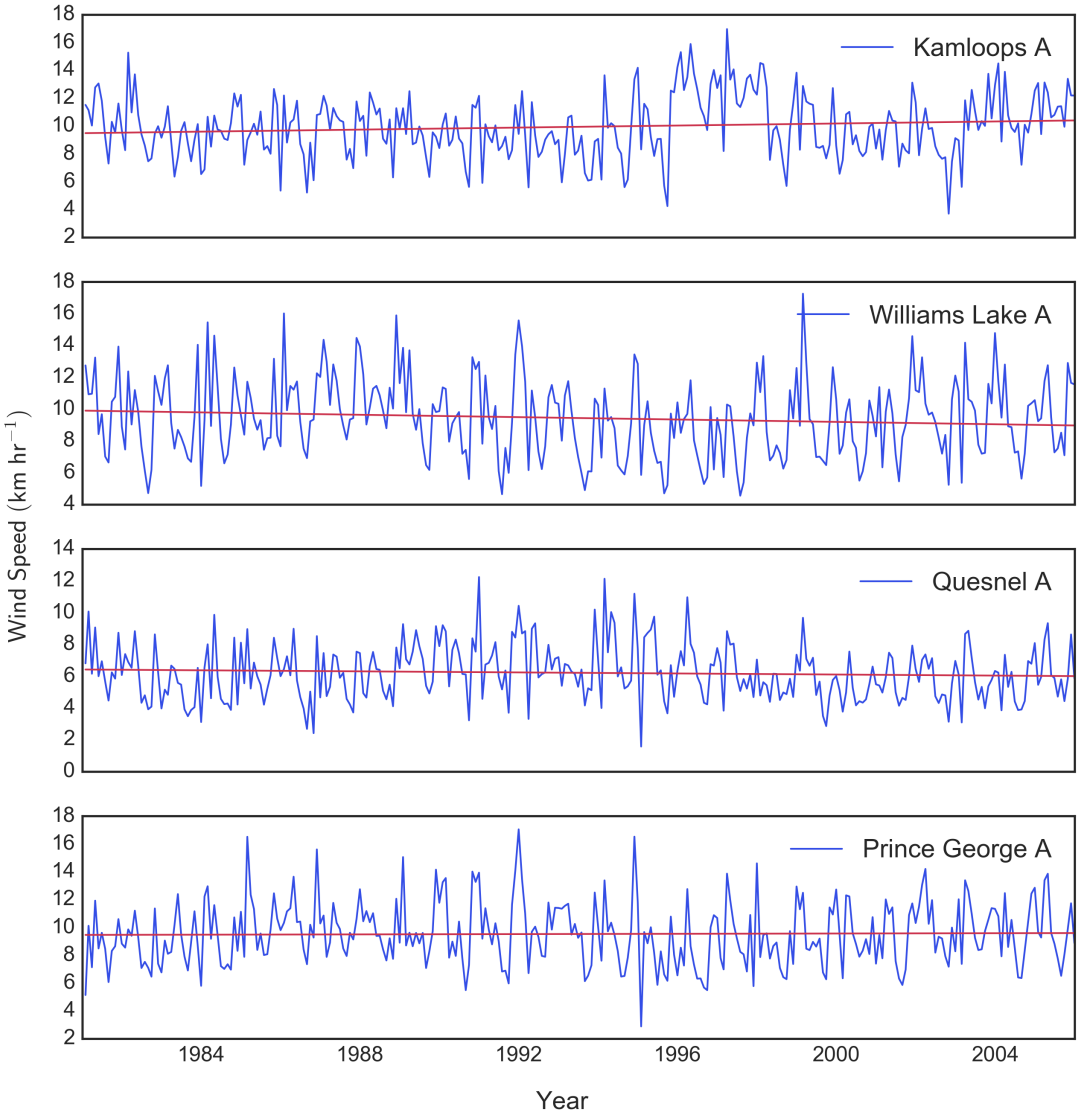

Figure 3.4.2: Mean monthly wind speeds (from mean daily values) at ECCC stations bordering the Cariboo Mountain Region for the period 1981-2005. Red lines indicate the trend of monthly values over the 25-year period

3.4.2 Seasonality in ECCC data

The monthly wind speed climatology values are analyzed to identify if any seasonal signal exists. All four sites experience a bi-modal temporal distribution of wind speeds, with the standard deviation being proportional to the mean of each month (Fig 3.4.3).

Williams Lake A experiences its first peak in February, and has below average wind speeds for May to September, with a minimum in August. Kamloops A wind speeds peak in March, followed by a below average period from June to October encapsulating a minimum also in August. Prince George A sees peak wind speeds between March and April and experiences minimum wind speeds in August, with a below average period running from May to September. Finally, Quesnel A has a peak in April and below average winds during May to October, with minimum mean monthly wind speeds occurring during September. All stations experience their second peak in wind speeds in November. All stations experience above average wind speeds during the northern-hemisphere winter (December to February), with the exception of Quesnel A that dips below average for the month of January (Fig. 3.4.4).

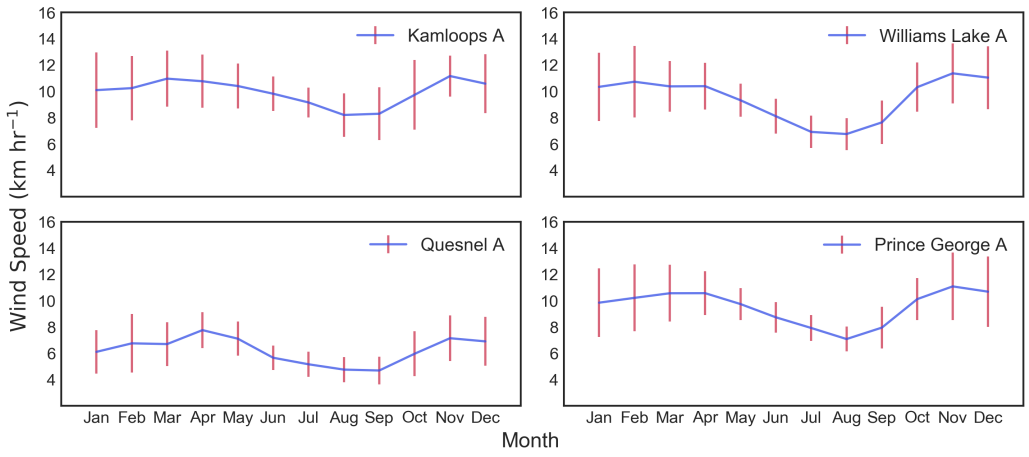

Figure 3.4.3: Monthly wind speeds at four ECCC stations bordering the Cariboo Mountain Region over the period 1981-2005. Error bars represent one standard deviation

The climatological mean for the four stations (represented by the black dashed line in Fig. 3.4.4) clarifies this seasonal signal with a change from above average to below average wind speeds occurring between May and June, and opposite transition occurring around September and October. Utilizing a mean value to represent the seasonal signal observed at all four sites is justified by the strong covariance seen between the datasets (Table 6).

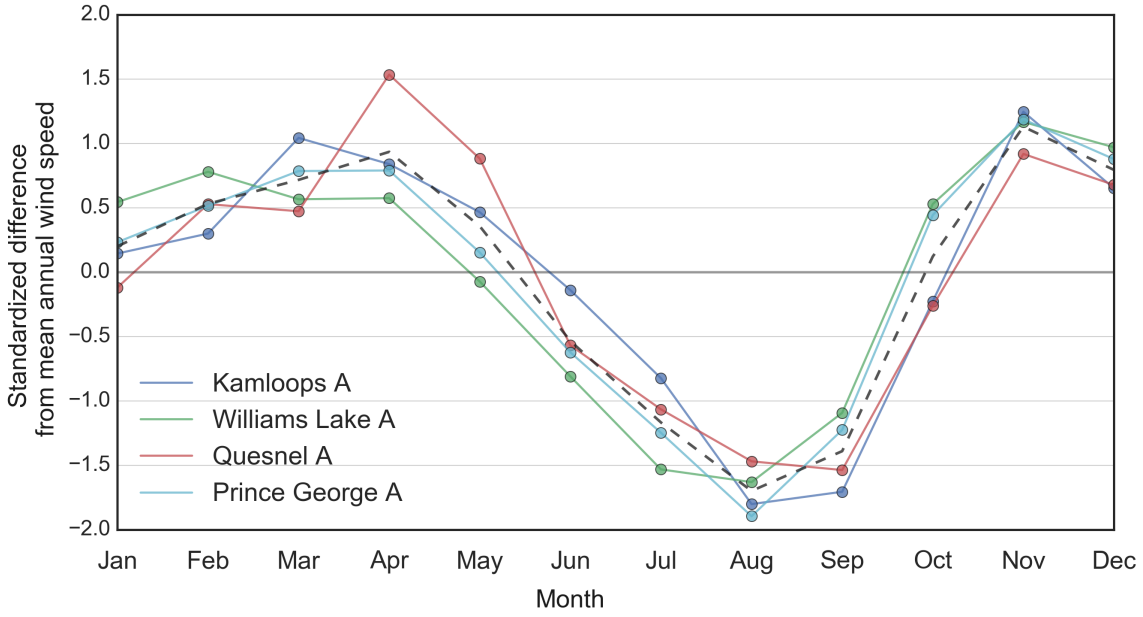

Figure 3.4.4: Standardized monthly wind speeds at four ECCC stations bordering the Cariboo Mountain Region for the period 1981-2005. The climatological mean of all four stations is indicated by the dashed black curve

This ranges from 0.83 between Quesnel A and Williams Lake A, to 0.98 between Prince George A and Williams Lake A.

Table 6: Covariance of monthly standardized wind speeds between four ECCC stations bordering the Cariboo Mountain Region for the period 1981-2005

Station	Kamloops A	Williams Lake A	Quesnel A	Prince George A
Kamloops A	-	0.84	0.93	0.90
Williams Lake A	0.84	-	0.83	0.98
Quesnel A	0.93	0.83	-	0.88
Prince George A	0.90	0.98	0.88	-

* All results are statistically significant at $p < 0.05$

Therefore, from this point onwards, June, July, August, and September will be classified as calm months, given the usually weaker winds and lower wind speed variability. The bi-modal shape to Fig. 3.4.3 indicates the months of October to May could be split further

into two separate seasons, one centred around the wind speed peak in March (i.e., January to May), and another around the peak in November (i.e., October to December). However, applying the Mann-Whitney U test to the two active seasons illustrates that they do not have statistically different mean wind speeds, and therefore will all be classified together as active months until further support for delineating these seasons becomes available.

When the original 25-year monthly timeseries is separated into active and calm months, differences in the distribution of wind speeds are observed. Box-and-whisker plots show the greater variability in wind speeds during the active months by the larger interquartile range and longer 'whiskers', especially evident for Quesnel A (Fig 3.4.5). There are also fewer outliers in the calm months, with Kamloops A having two, Williams Lake A one, and Quesnel A and Prince George A having no outliers.

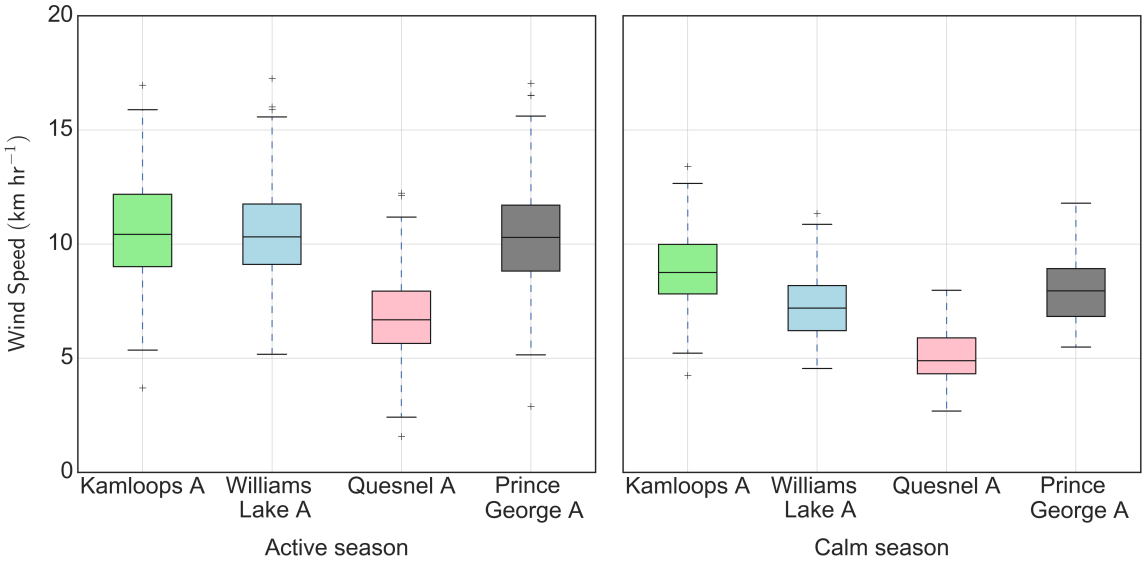

Figure 3.4.5: Box-and-whisker plots of active months (October to May) and calm months (June to Sept) observed at ECCC stations. Distributions are of mean monthly wind speeds (km hr^{-1}) for the period 1981-2005. Upper and lower box boundaries represent the 75th and 25th percentiles, while the centre line marks the median. Whiskers span 1.5 times the interquartile range, crosses outside of this range represent outliers

The 25 years of calm months result in a sample size of n = 100, while the active months have

a sample size of n = 200. Applying the Mann-Whitney U test to each of the distributions illustrated in Fig. 3.4.5 indicated that a significant difference ($p < 0.05$) exists between the calm and active mean monthly wind speeds (Table 7). CV values also appear lower during calm months, indicating lower wind speed variability during June to September. This is in contrast to the original data, where lower wind speeds observed higher CV values. This change indicates a synoptic control on the wind climate that results in higher mean wind speeds coupled with greater wind speed variability during October to May, such as the passage of mid-latitude cyclones. Due to the small number of stations and non-normal distribution of CV values, a test to indicate the significance of this difference was not applied.

Table 7: Descriptive statistics of mean monthly wind data separated into calm and active months*, from four ECCC stations bordering the Cariboo Mountain Region during the period 1981-2005

Station	Mean wind speed (km hr^{-1})	Wind speed σ (km hr^{-1})	Wind speed CV	Mean wind direction (degrees)	Wind direction σ (degrees)
Calm season:					
Kamloops A	8.85	1.68	0.19	165.5	39.8
Williams Lake A	7.33	1.48	0.20	287.2	108.1
Quesnel A	5.04	1.03	0.20	263.4	90.9
Prince George A	7.90	1.32	0.16	233.5	33.8
Active season:					
Kamloops A	10.72	2.40	0.22	119.0	34.2
Williams Lake A	10.82	2.36	0.22	148.9	38.3
Quesnel A	6.81	1.80	0.26	163.7	55.9
Prince George A	10.25	2.23	0.21	206.8	66.4

*Calm months: May to September; active months: October to May

Mean and standard deviation values for wind directions differ between the calm and active months (Table 7). However, I will focus on analysing the windroses presented in Figure 3.4.6 rather than relying on the descriptive statistics. At Kamloops A, southeasterly winds

dominate during calm months, with occasional southerly and southwesterly winds. These give way in active months to strong easterly winds, with the occasional southerly. Prince George A predominantly sees south to southwest winds throughout the year, with an increase in intensity and a small influence from some northerly winds at times during the active months. The Quesnel A station experiences winds from a broad range of directions during calm months with northwesterlies being dominant, but a shift to the south-southeast is clearly visible and becomes the prevailing direction during active months. Finally, at Williams Lake A, winds during calm months are almost isotropic, with a distinct shift in active months to strong southeasterlies that have low variability.

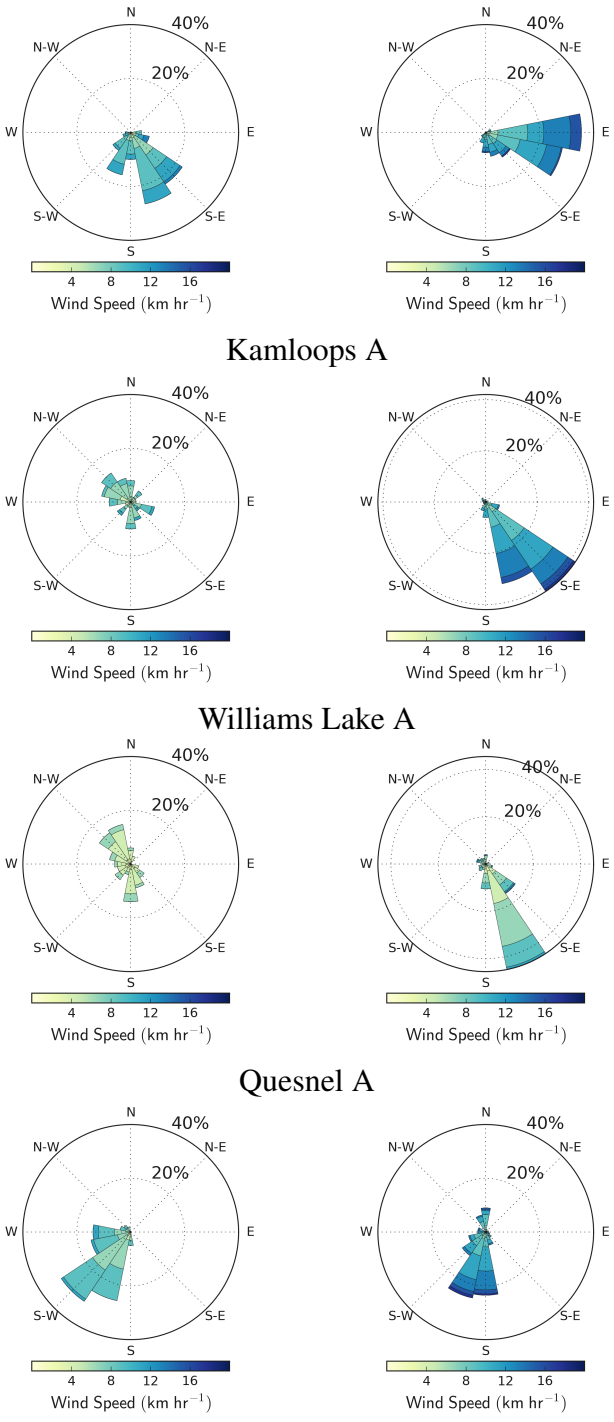

Figure 3.4.6: Windroses for calm months (left) and active months (right), for four ECCC stations bordering the Cariboo Mountain Region for the period 1981-2005. Active months (October to May) are compiled from 200 monthly values, calm months (June to September) are compiled from 100 monthly values

3.4.3 Comparison of ECCC and CAMnet data

The standardization of both the ECCC and the CAMnet datasets allows for a comparison of the seasonal signal, despite the differences in recording methods, anemometer heights, and even the unit of measurement (km hr^{-1} versus m s^{-1}).

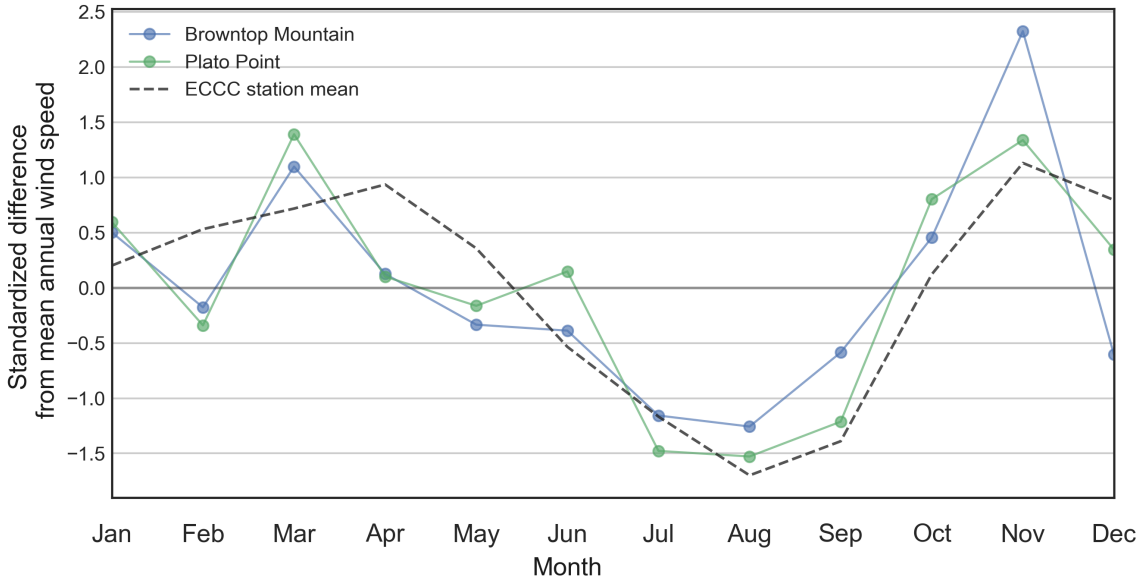

Figure 3.4.7: Standardized monthly wind speeds at two CAMnet stations within the Cariboo Mountain Region. CAMnet data cover the period 1 October 2016 to 30 September 2017, but is presented similar to Fig. 3.4.4 for comparison. The climatological mean of four nearby ECCC stations from January 1981 to December 2005 is indicated by the dashed black curve, identical to Fig. 3.4.4

Figure 3.4.7 displays the seasonal signal identified by the ECCC mean along with two CAMnet stations situated within the mountainous topography of the CMR. The CAMnet stations differ from the long-term ECCC mean by experiencing below average wind speeds during February and May. The Plato Point station also experiences above average wind speeds during June. However, both sites observe a trend of wind speeds being generally lower during the calm months of June to September, along with August having the lowest mean monthly wind speed. All datasets show above average wind speeds during October

and November, and then again in March and April. The mean monthly wind speeds during November are particularly notable for their difference from the annual mean.

Table 8: Covariance of standardized monthly wind speed data between two CAMnet stations and the climatological mean from four nearby ECCC stations, for the period 1 October 2016 to 30 September 2017

Station	Plato Point	Browntop Mountain	ECCC mean
Plato Point	-	0.86	0.78
Browntop Mountain	0.86	-	0.66
ECCC mean	0.78	0.66	-

* All results are statistically significant at p = 0.05.

Covariance between Plato Point data and the ECCC mean is moderate at 0.66, with Browntop data and the ECCC mean being slightly stronger at 0.78. The two CAMnet stations have a covariance of 0.86 (Table 8).

3.5 Discussion

The 25 years of continuous monthly wind data derived from four ECCC stations bordering the CMR strongly indicate a seasonal pattern across the region. From this analysis, I propose that there are three wind seasons that affect the CMR. Below average (compared to the annual mean) winds are observed during the months of June to September, which form the calm Summer season. Lowest mean monthly wind speeds are observed in August. Above average (compared to the annual mean) winds occur from October to May, thus creating active months, which in turn can be separated further into an active Fall (October to December) and an active Winter/Spring (January to May). The active Winter/Spring sees a local maximum in mean monthly wind speed around March or April, depending on the location. The active Fall season experiences the strongest winds of the year with a peak in mean monthly wind speeds during November.

Strong covariance of the seasonal signal at all stations supports the adoption of these seasons over the use of traditional climatological seasons, with regards to winds in the CMR. An example of this is seen in Fall (Autumn), which would usually group the months of September to November together. Here, the difference between mean monthly wind speeds during September and November is pronounced. The significance tests performed on monthly wind speeds during calm months and active months confirm the differences observed in the plotted data. However, no statistical difference exists between the mean monthly wind speeds observed during the two active seasons.

Although the latitudinal range of the four ECCC stations was just over 3° ($\sim$ 400 km), no attempt has been made to resolve any spatial variation or latitudinal dependence between the datasets. At each location, the wind data recorded will be influenced by the surrounding topography, land use changes, and densification of local urban areas. The primary objective was to explore the similarities in data, rather than highlight the differences.

When compared to 12 months of data from two meteorological stations within the CMR the proposed seasons explain a large portion of the observed intra-annual variability. Logistical challenges prevent instrumentation at these wilderness locations being serviced and maintained to the same standards as federally operated sites, therefore limiting the availability of long term data. It is therefore suggested that the mountainous terrain at the heart of the CMR also experiences the same seasonal signal identified in the four ECCC datasets.

4 Synotpic climatology

4.1 Introduction

This chapter is centred around a synoptic climatology of strong wind episodes at Quesnel Lake. These strong wind episodes are defined by periods of 36 hours or more in duration where the square of the wind speed (henceforth, wind stress) is above the 80th percentile of hourly wind stress observations. Firstly, strong wind episodes are identified, categorized, and quantified. Secondly, a synoptic climatology of the typical atmospheric states that drive these episodes is compiled. This is initially performed manually, followed by an exploratory investigation in the use of a Self Organising Map (SOM).

The study of synoptic climatology is outlined by Yarnal (1993) as research methods that relate the atmospheric circulation to the surface environment (p.5). Such methods are commonly employed to classify various synoptic-scale states of the atmosphere, which in turn explain an environmental response at the surface. This popular tool is known as a circulation-to-environment study (Yarnal, 1993). Locally, this approach was taken by Stahl et al. (2006) to classify 13 synoptic types influencing BC's wintertime precipitation and temperature.

However, using a sub-set of methods from Yarnal (1993), it is also possible to conduct an environment-to-circulation investigation, where pre-defined events are identified (e.g., episodes of strong wind stress), and the related synoptic patterns are organised into categories or clusters. This organisation can be performed manually by an investigator (which Yarnal (1993) recommends for students and early career meteorologists), or autonomously using pre-packaged software or a statistical programming language. The use of a SOM as a computer-assisted method for synoptic pattern clustering is gaining in popularity (Sheridan and Lee, 2011; Hewitson and Crane, 2002). Here, a continuum of synoptic states can be

represented on a two-dimensional grid of nodes, where patterns that are similar are grouped together, and dissimilar patterns are spaced further apart. Despite the advancements in these processes, some subjective choices are still required by the investigator such as the number of nodes, and the shape of the map. Both of which affect how partitioned the synoptic states will be.

The majority of SOM applications in climatology utilize the power of the underlying algorithm to sort large quantities of input vectors, sometimes decades of daily observations (i.e., Schuenemann and Cassano, 2010). However, these would be generally regarded as climate-to-environment climatologies, and the SOM method has less coverage in the environment-to-climate literature. Whereas the former requires investigators to use various metrics in evaluating the performance of the SOM, usually by trial and error, the smaller number of observations used in this study allow for a general premise of what the ideal output of the SOM should be. With this in mind, I will evaluate the SOM's performance in relation to the manual investigation, rather than expecting the algorithm to reveal new information. This will be a novel test for the use of a SOM in synoptic climatology: to project the synoptic states of a low observation environment-to-climate study, in a meaningful way.

While a review of synoptic climatology literature provides insight to the breadth of investigations, no published research to date has employed an environment-to-climate study in regards to the forcing of hydrodynamic processes in lakes in western Canada. However, the motivation for creating a synoptic climatology of strong wind events at Quesnel Lake comes from the success of Rabinovich and Monserrat (1998) and de Jong and Battjes (2004), who identified that large-scale atmospheric patterns and frontal-activity could excite internal seiche modes in coastal marine environments.

A regionally-pertinent example of literature connecting synoptic features to localized strong

winds is provided by Bakri et al. (2017a), where the relationship between gap winds along the West Coast of BC and the associated synoptic states were examined using mean sea level pressure and 500 hPa geopotential height patterns. These recent findings agree with Brewer et al. (2012) who identified the seasonal dependence of synoptic features such as the west coast thermal trough.

4.2 Data and Methods

4.2.1 Near-surface data

Data used for identifying strong wind episodes originate from a CAMnet station at Plato Point (Figs. 2.1.1 and 2.2.1), which provides the longest record of 15-minute interval lake-level wind observations. Wind data from nearby Browntop Mountain were analyzed for the same purpose but the station appears to suffer from intermittent icing, indicated by prolonged periods of 0.0 m s^{-1} winds during November to April, therefore rendering the dataset unusable in this study. I have used the 15-minute wind data from Plato Point station under the assumption that they represent wind conditions in the main basin of Quesnel Lake, and over longer time-scales (e.g., daily averages) can be representative of wind conditions over the entire lake. Consequently, a two-year timeseries from 1 October 2016 to 30 September 2018 is chosen to maintain continuity with the previous chapter's identification of three wind seasons. There were no missing values from the raw 15-minute dataset covering this period, resulting in 17,520 observations.

The 15-minute wind speed observations in the raw wind speed dataset were squared and then averaged by the hour to derive a timeseries of mean hourly values that were proportional to τ (see equation 1.1) with units of m^2 s^{-2}. This was smoothed by a 36-hour moving average, similar to Laval et al. (2008). The smoothed hourly timeseries will from hereon be known as the wind stress, and denoted U^2. Wind stress or U^2 values are preferred as

they highlight periods of greater forcing for wind-driven hydrodynamic processes better than raw wind speeds alone.

4.2.2 Identifying periods of strong winds at Quesnel Lake

For environment-to-climate synoptic climatologies, meteorological events at or near the surface first have to be identified. An investigator may have many subjective choices to make in regards to what parameters are important for the study, and how to filter and identify such events (Yarnal et al., 2001). The methods I have developed for delineating strong wind episodes at Quesnel Lake are motivated by similar work examining mid-latitude storm occurrence in Perth, Australia (Breckling, 1989). For an episode to be recorded, wind stress values must exceed the 80th percentile of the mean annual wind stress (12.5 m^2 s^{-2}) for a continuous period of 36 hours or more. The 80th percentile was chosen after trials with various thresholds. The aim was to identify a value low enough that allowed sufficient episodes to be identified, while high enough to justify that episodes could have an effect on lake hydrodynamics. The minimum episode duration of 36 hours originates from work by Laval et al. (2008), where they identified a required forcing duration of 1.5 days. For episode timing, it is important to note that all CAMnet stations operate on Pacific Daylight Time (PDT), which is 7 hours behind Coordinated Universal Time (UTC).

Figure 4.2.1 shows the method in practice identifying a strong wind episode from the U^2 timeseries. The values derived for each episode were:

1. Start Date/Time (PDT)
2. End Date/Time (PDT)
3. Duration (hours)
4. Date/Time of maximum U^2 (PDT)

5. Mean wind direction (degrees)

6. Wind direction standard deviation (degrees)

7. Wind steadiness (S)

8. Mean U^2 ($m^2\ s^{-2}$)

9. Total U^2 ($m^2\ s^{-2}$)

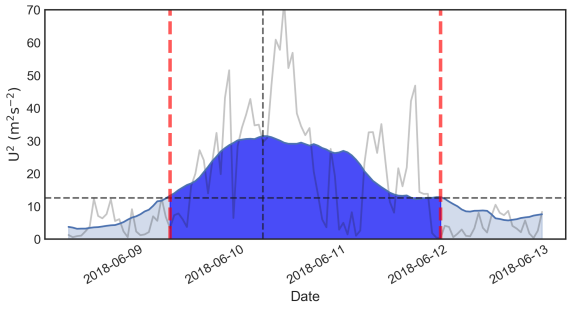

Figure 4.2.1: An example of applying the described methods of identifying strong wind episodes to data from Plato Point, during the period 8 June 2018 to 13 June 2018. Red dashed lines mark the beginning and end times of the event. The vertical black dashed line represents the time of maximum wind stress. The horizontal black dashed line represents the 80th percentile threshold. Blue shading indicates the total stress integrated over the episode. The background light grey trace is the hourly wind stress timeseries before applying the 36-hour moving average.

The total U^2 was calculated by summing the hourly U^2 values over the duration of the episode. Although this is not an exact representation of the area under the curve, nor a physical parameter commonly derived in similar research, it is intended to be a value that can assist in statistically comparing the various episodes within this study alone. One limitation of these methods is that averaging the wind directions over each episode did not account for wind shifts during the event, which may dampen the response of the lake to the resultant wind stress; however, manual analysis of the strong wind episodes revealed that winds shifts were usually minimal, or occurred at or near the end of the episode. To validate

this further, wind steadiness (S) has been included to provide a measure of the constancy of the direction during each event. First published by Singer (1967), S is derived by taking a linear transformation of the wind constancy (k), which is calculated by dividing the mean hourly wind vector by the mean hourly wind speed (scalar). A value of 1.0 denotes that wind directions are constant over the period (low wind direction variability), whereas a value of zero represents a 180° symmetrical distribution of wind directions (high wind direction variability) (Singer, 1967). Hourly values of S were averaged over each episode to obtain a mean S for each event. Appendix A provides a complete table of the filtered episodes.

4.2.3 Quantifying strong winds at Quesnel Lake

The filtered episodes were then categorized using two main criteria: (i) by the three wind seasons identified in Chapter 3, and (ii) by the mean wind direction during each episode. This was to investigate whether differences exist in the frequency or impact of these episodes based on these two categories. The fraction of episode occurrences per month is also provided.

Accurate significance testing of episode variables was limited due to the small sample sizes. However, where applicable, I have used Welch's t-test that allows for differences in the variance between each sample (and therefore differing sample sizes), where the standard student t-test does not (Delacre et al., 2017).

4.2.4 Reanalysis data

To understand the large-scale atmospheric forcing for each strong wind event, synoptic data of geopotential height at 925, 800, and 500 hPa were downloaded from the European Centre for Medium Range Weather Forecasts' (ECMWF) ERA-Interim reanalysis archive

(http://www.ecmwf.int/research/era). The ERA-Interim product runs from January 1979 to the present, has a spatial resolution of 1.25°, and is available on 60 vertical pressure and model levels (Berrisford et al., 2009; Dee et al., 2011). Data are provided at the synoptic hours of 0000 UTC, 0600 UTC, 1200 UTC, and 1800 UTC. The ERA-Interim has recently been used for large-scale wind power and global-scale wind stress investigations (Lavagnini et al., 2006; Hanley et al., 2010), providing confidence for its use within this study.

The timings used for this study correlate to the strong wind episodes by specifying the time of maximum wind stress as T-0 (Fig. 4.2.1). ERA-Interim data were obtained for the synoptic hours closest to T-0, and for the synoptic times 24 and 48 hours prior (T-24 and T-48, respectively). If T-0 fell in between synoptic hours (e.g., 0900 UTC), the time was rounded forward to the next synoptic hour, thus capturing as much of the event as possible. That is, T-0 would occur some time after the occurrence of maximum wind stress. Initially, data at 72 hours prior to the episode were also included, however, it was found that some events were close enough in time that independence of the data could not be guaranteed, and the T-72 time-step was discarded.

Data were initially downloaded covering a domain of 25°–70° N, and 80°–190° W, at resolutions of $1.5° \times 1.5°$ (2400 grid points) and at $2.5° \times 2.5°$ (855 grid points). This is a larger domain than used by Bakri et al. (2017a) and Stahl et al. (2006), however, the long duration of a number of the strong wind episodes meant that a larger 'upstream' view was required. This would allow adequate visualization of the synoptic patterns in the Northeastern Pacific basin. To facilitate the use of a SOM it was discovered that a domain covering 47.0°–57.5° N, and 112.5°–130° W at resolution of $1.5° \times 1.5°$ (117 grid points) improved performance. This change also located Quesnel Lake at the centre of the domain (see section 4.3).

The pressure levels of 925 and 800 hPa were selected because they approximately intersect

the surface at Quesnel Lake and Browntop Mountain, respectively. The 500 hPa level was used to represent the mid-troposphere, where wind flow is assumed to be geostrophic. The geopotential height gradient at each grid point was calculated to provide datasets of pressure gradient.

4.2.5 Manual analysis of the synoptic maps

A manual analysis of synoptic patterns related to each strong wind event was performed to examine if reoccurring patterns were identifiable, and to provide an understanding of the variety in atmospheric states. I conducted the analysis using maps of 925, 800, and 500 hPa geopotential heights covering the large domain and time steps outlined in section 4.2.4. The procedure was analogous to the manual methods recommended by Yarnal (1993), whereby maps of similar composition were clustered together depending on their synoptic features such as the locations of low pressure systems, short-wave troughs, and high pressure ridges. Advances in computer graphics since the conception of manual analysis methods meant that images were shuffled around on a computer monitor rather than printed copies on a table. It was found that the clearest differences in synoptic states could be seen at T-0 (time of maximum U^2) in the 925 hPa and 500 hPa geopotential height patterns. I hypothesized that the clustering of maps could also be performed based on either the wind season in which the event occurred, or the mean wind direction at Plato Point during the episode. For mean wind directions I started by using four 90° windows centred on the four cardinal points of North, South, East, and West. This was amended when differences in the synoptic maps did not appear to be aligned with these wind direction windows, and new delineations of 0° to 179° for Easterly winds, and 180° to 359° for Westerly winds were used instead. Composite maps were constructed using the mean geopotential height values from all of the episodes in each classification, in this case, by mean wind direction.

The manual analysis of synoptic maps is a subjective procedure, and as such is open to investigator bias (Yarnal et al., 2001). It is therefore possible that another researcher may have grouped synoptic patterns in a different manner, or that other trends in the synoptic patterns may be evident that I had not identified. I was particularly concerned that the seasonality in occurrence of events (Fig. 4.3.2) had been overlooked during the manual analysis. Yarnal et al. (2001) provide evidence that confirmation of the manual clustering of synoptic patterns can be obtained by utilizing a computer-assisted procedure. This removes the subjective nature of the manual analysis, and provides an alternative outlook on the similarities or differences between the atmospheric states observed for each strong wind event. With advice from colleagues and a burgeoning body of literature (see Skific and Francis, 2018; Sheridan and Lee, 2011; Hewitson and Crane, 2002), I chose to use a SOM to project the various clusters of synoptic patterns.

4.2.6 The Self Organizing Map

The general principle that governs a SOM is that input vectors are clustered at nodes where the Euclidean distance is the lowest (Sheridan and Lee, 2011). In this study, an input vector (also known as an observation) is the synoptic state at a specified time. An advantage a SOM has over other clustering methods is its ability to handle multi-dimensional data, therefore the input vector can contain information about multiple variables (e.g., pressure, temperature, precipitation). This allows for a more detailed description of the state of the atmosphere. Since the primary driver for wind in the atmosphere is the spatial gradient of atmospheric pressure, the pressure patterns at multiple levels have been coupled together to describe the synoptic state in greater detail.

The first step taken to create an observation was to reshape the M$\times$N grid of ERA-Interim data to a single dimensional vector, that would be of length M$\times$N. These were standardized

over the spatial domain (all the values in each vector) to obtain vectors of geopotential height anomalies, which removes the magnitude and reduces the disproportionate influence of a single variable or outlier (Schuenemann and Cassano, 2010). Each vector point was then area-weighted by multiplying it by the cosine of the square of the latitude that it originated from. This is due to a standard latitude/longitude grid not being uniform in shape, which results in grid points near the equator accounting for greater area than grid points near the poles (Loikith et al., 2017).

Standardized, area weighted vectors from the 925 and 500 hPa levels at each T-0 were concatenated together to form an input vector that was of length M×N×2. These would be used to represent the synoptic state at the peak of each strong wind event. For many episodes the 925 and 800 hPa patterns appeared very similar, so including the 800 hPa level would have only lengthened the processing time, and increased the possibility of an unstable learning process (Sheridan and Lee, 2011). The final form of the 47 input vectors made up of M×N×2 grids points then resembled:

$$Vector_i = [X_1^{925}, X_2^{925}, X_3^{925} \ldots \ X_{M\times N}^{925}, \ X_1^{500}, X_2^{500}, X_3^{500} \ldots \ X_{M\times N}^{500}] \tag{4.1}$$

The final method and successful values used for the learning rate, neighbourhood distance decay, and number of iterations (all outlined by Hewitson and Crane, 2002), will be discussed in Section 4.3.

4.2.7 Comparison with known periods of interest

Previous literature and continuing research by a physical limnology team at The UBC have allowed for two periods of interesting hydrodynamic response to wind forcing to be investigated. Here, I am able to compare the methods used to identify the strong wind episodes

with the timing of one of the case studies. The synoptic patterns for both cases will be evaluated against both the manual analysis and the SOM results. The synoptic data will then be transformed into new input vectors for the master SOM, and their node location considered as a measure of success for using the SOM method.

4.3 Results

4.3.1 Strong wind episodes

During the 24-month period from 1 October 2016 to 30 September 2018, 47 strong wind episodes were identified using the methods outlined in Section 4.2.2 (Fig. 4.3.1). The monthly distribution of episodes correlates to the seasonal signal in Section 3.4., where a peak in episode occurrence is observed in March, and again in November (Fig. 4.3.2).

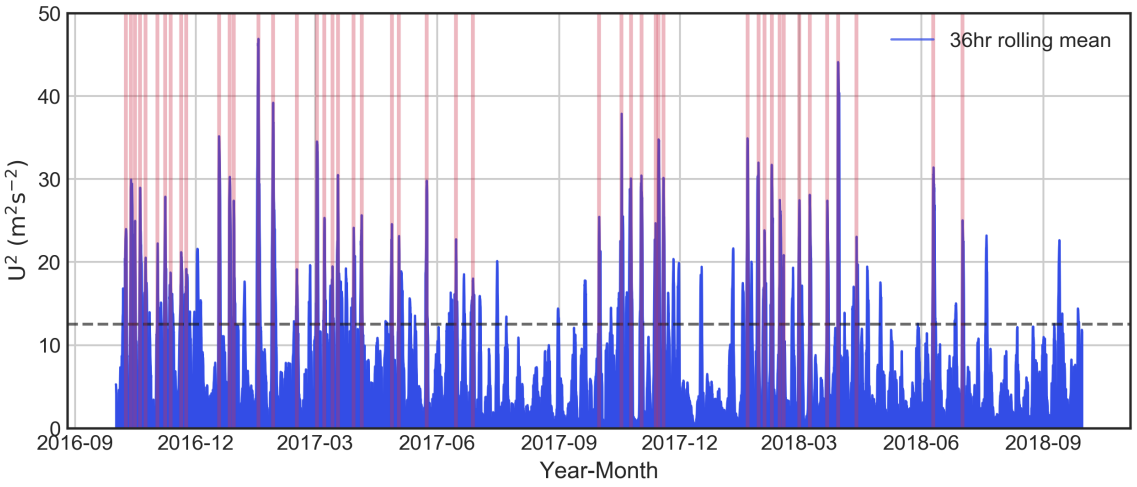

Figure 4.3.1: 36-hour rolling average U^2 timeseries, derived from 15-minute wind data collected at Plato Point during 1 October 2016 to 30 September 2018. The black dashed line indicates the 80th percentile of U^2 values (12.5 m^2 s^{-2}). Light red shading indicates periods of strong wind episodes with a duration of 36 hours or more

The lower frequency of strong wind events during the summer months (June to September) also contributes to the observed lower mean winds speeds. Westerlies and easterlies have

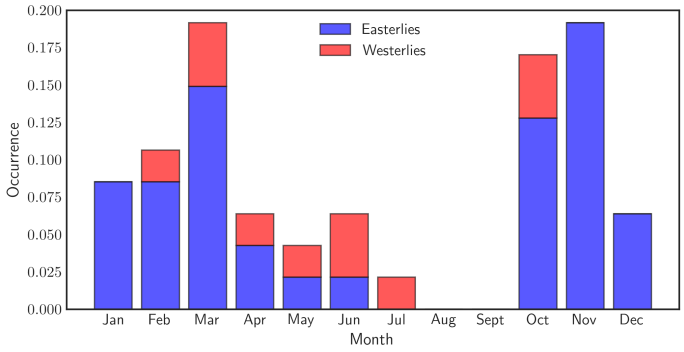

Figure 4.3.2: Monthly occurrences of strong wind events at Plato Point over the period 1 October 2016 to 30 September 2018, stratified by wind direction. Easterlies are between 0° and 179°, westerlies between 180° and 359°. The number of episodes has been standardized by the number of total occurrences

been defined as episodes where the mean wind direction for the duration of the event was less than 180°, or greater than 180° degrees, respectively. Easterly episodes account for the majority of cases, with 37 (79%) during the two years. November is not only a peak for events in general, but is also comprised exclusively of easterly events. This points towards a single synoptic mechanism driving episodes during this month, such as the mid-latitude cyclones that approach BC from the Northeastern Pacific basin during this time of the year (Bakri et al., 2017a). Ten westerly events occurred (21%), distributed over the months of February to October, with a peak occurrence in June. The median duration of easterly events was 49 hours compared to westerly events that lasted 41 hours, however, this difference was not statistically significant (Welch's *t*-test: stat = -1.755, p = 0.095). This difference in duration also leads to a difference in the median total U^2 derived during each event, with easterlies recording 1028 $m^2\ s^{-2}$ compared to the westerlies value of 918 $m^2\ s^{-2}$ (Table 9). Again, this difference was not statistically significant (Welch's *t*-test: stat = -1.04, p = 0.309). No statistical tests were applied to the columns in Table 9 to examine the differences between wind seasons, due to the disparity between sample sizes. However, events during the calmer summer season appear to last the same length of time as events

during the more active months, yet have a lower average wind stress and therefore lower total U^2 values. The mean wind direction during the summer is 218°, compared to 125° and 135° during fall and winter/spring, respectively. This indicates a different synoptic mechanism is involved during the summer, most likely the influence of the Pacific high as it builds off the coast of North America during the warmer months. This high pressure then creates the required west-to-east pressure gradient across central BC.

Table 9: Median and standard deviation (in brackets) values* for quantities calculated during strong wind episodes at Quesnel Lake during 1 October 2016 to 30 September 2018

	Occurrences	Duration (hours)	Mean wind direction (degrees)	Mean U^2 (m^2 s^{-2})	Total U^2 (m^2 s^{-2})
Winter/Spring	23	46.0 (13.9)	135 (48)	21.4 (4.6)	1028 (398)
Summer	4	48.0 (12.2)	218 (56)	18.8 (3.3)	917 (268)
Fall	20	48.0 (9.8)	125 (35)	21.1 (3.2)	997 (263)
Easterlies	37	49.0 (12.6)	118 (20)	20.2 (3.7)	1028 (357)
Westerlies	10	41.0 (9.0)	229 (14)	21.8 (5.1)	918 (244)

*Mean wind direction values are given as circular mean and circular standard deviation.

Fig. 4.3.3 displays the events delineated by wind season. For each episode, the radius (y-axis) of the windrose represents mean U^2, the angle represents the mean wind direction, and the area of each bubble is proportional to the total U^2 value. All events appear to be constrained to an average wind direction between 90° and 270°. This is partly due to the synoptic forcing and the resulting pressure gradient (Fig 4.3.6), but also evidence of wind channelling by the surrounding topography. The southern shoreline of the main basin approaches Plato Point from the west around $\sim 230°$ (SW to NE), and the bay to the east of Plato Point is aligned at $\sim 105°$ (NW to SW). The grouping of stronger episodes (larger bubbles) around 15 m^2 s^{-2} to 30 m^2 s^{-2} from the direction of $\sim 120°$, indicates that the synoptic patterns related to these episodes may not have a large amount of inter-event

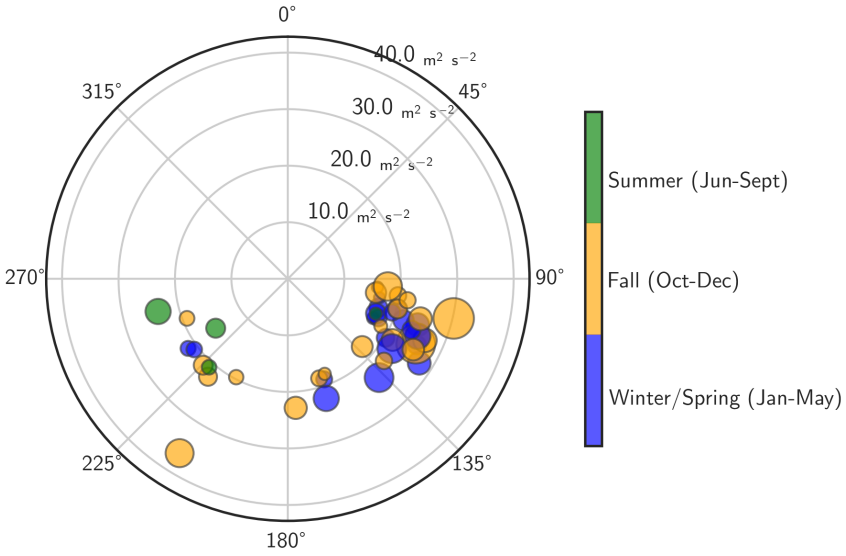

Figure 4.3.3: Windrose of 47 strong wind events recorded during 1 October 2016 to 30 September 2018. Directions follow standard meteorological convention. The radial axis of the windrose represents the mean wind stress during the episode. The size of each bubble represents the total wind stress during the episode, but sizes have been altered to allow for easier comparisons: the smallest bubble represents 613 m^2 s^{-2} while the largest represents 2204 m^2 s^{-2}. Intermediate values follow a linear scale

variability.

4.3.2 Manual synoptic analysis and composites

There were few significant differences between the map patterns based on the month of year, or the season of occurrence. That is, a mid-latitude cyclone approaching the coast of BC looks similar regardless of which month or season it occurs in. However, distinct contrasts were apparent between map patterns that related to westerly events compared to the easterly events.

The westerlies composite at T-0 (time of maximum hourly wind stress at Lake-level) is dominated by a broad mid-level (500 hPa) ridge sitting west of the BC coast, extending northwards into the Gulf of Alaska (Fig. 4.3.4). This correlates to the lower level pattern

(925 and 800 hPa) where a closed high (bottom of image) is situated off the coast of California. The ridge axis in all three levels follows the line of longitude at $\sim 140^{\circ}$. The ridge develops over the 48-hour period by the building high pressure off the coast of California migrating northwards, especially evident in the 800 hPa series.

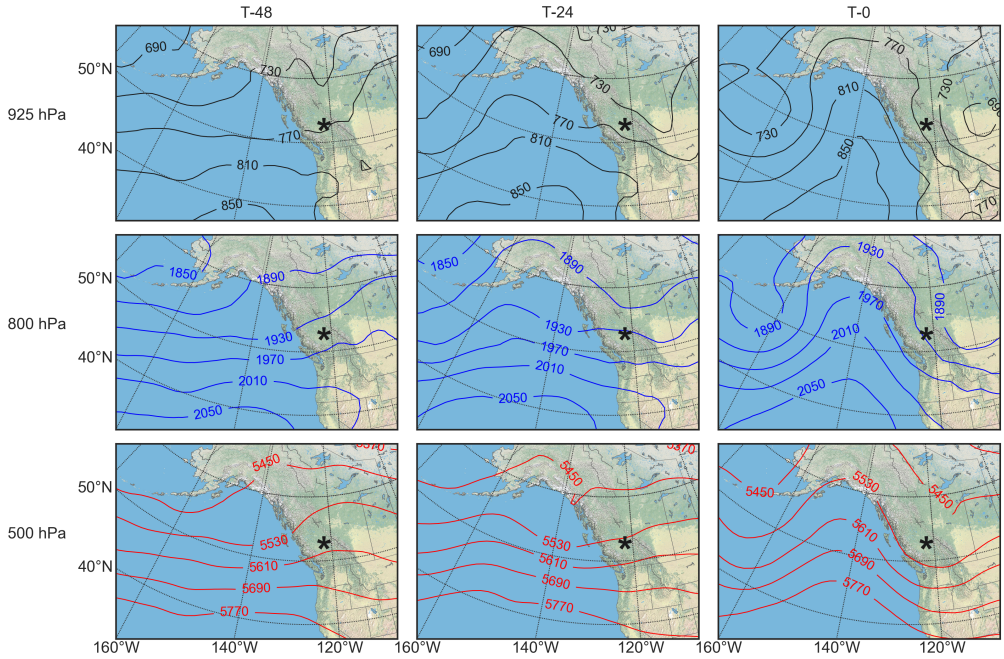

Figure 4.3.4: Composites of geopotential height patterns for 10 strong westerly wind events at Quesnel Lake identified during 1 October 2016 to 30 September 2018. All heights are in metres (m). Panels step forward in time left-to-right, and go up in pressure level from top-to-bottom. Quesnel Lake is denoted by the black asterisk (*)

The T-0 500 hPa panel shows Quesnel Lake sitting just to the west of the axis of a mid-level shortwave trough (i.e., the trough has passed Quesnel Lake), located downstream of the ridge. This location of the ridge and trough axis contributes to the southwest-to-northeast pressure gradient over Quesnel Lake. The westerly episodes do not begin until the surface trough has passed over the region, with the passage of an accompanying mid-level trough during the event. The lower frequency of westerly events contributed to less variation observed during the manual analysis of the westerly patterns compared to the easterly

patterns, although some differences were observed in the 925 hPa and 800 hPa maps due to the influence of topography. In all westerly cases, some form of the mid-level ridge seen in Fig.4.3.4 dominated the pattern, with the major variation between events being the broadness of this ridge and the extent to which it would extend northwards before breaking down or migrating eastwards.

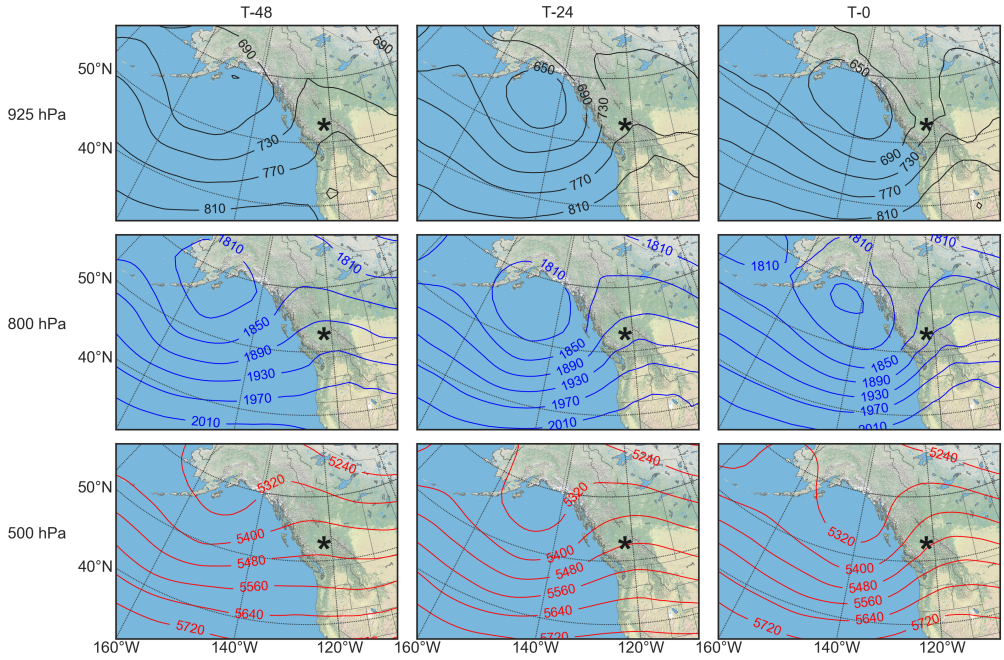

Figure 4.3.5: Same as Fig. 4.3.4 for 37 easterly events

Although the easterly episodes displayed greater variance when examined manually, they can all be attributed to the development of mid-latitude cyclones in the Northeastern Pacific basin. Therefore, the easterlies composite displays a typical scenario of a surface closed low in the region of the Aleutian low, migrating southeast towards the BC coast (Fig. 4.3.5). This (usually) deepening low is supported by the amplification of the mid-level shortwave trough over the 48-hour period. At T-0 the now clearly formed mid-latitude cyclone and associated mid-level trough are still offshore of BC. This is important as it shows that strong easterly winds at Quesnel Lake can be induced by synoptic features 1000 km (or

more) away. If the low pressure centre makes landfall along the mountainous coast of BC, the system loses its westward tilt with height, and begins to fill. This is seen in the majority of easterly events. Once the mid-level trough has either weakened or migrated sufficiently eastwards, the pressure gradient over Quesnel Lake relaxes and no longer supports the strong easterly flow.

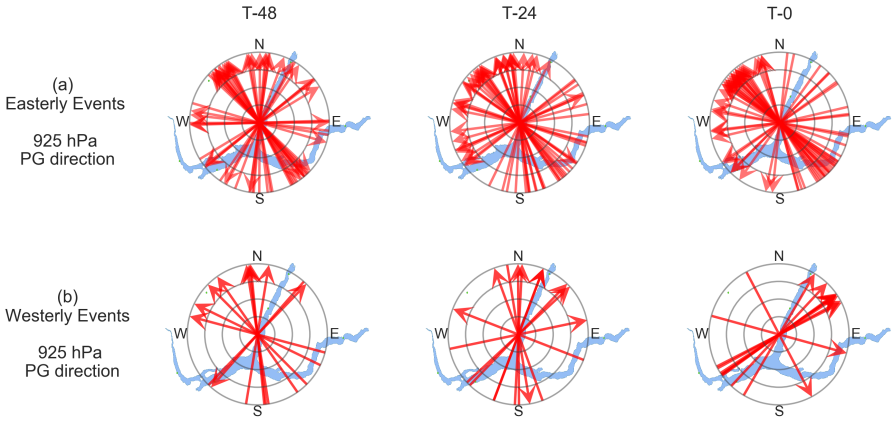

Figure 4.3.6: The direction of the 925 hPa geopotential height gradient over Quesnel Lake during (a) 37 easterly events, and (b) 10 westerly events identified during 1 October 2016 to 30 September 2018. Arrows indicate direction only, not magnitude

Although it can be inferred that easterly episodes occur while Quesnel Lake is located in the warm sector of a passing system, the passage of an intact mid-latitude system is rare due to the orography of the coastal mountains. This reduces the likelihood of strong wind shifts during the events, and again highlights the effect these systems have as they form and migrate southeastwards along the coast.

4.3.3 The projection of synoptic patterns using a self-organizing map

The SOM method described in section 4.2.6 was applied to the larger domain outlined in section 4.2.4. This domain is the area covered in Figs. 4.3.4 and 4.3.5. Trials were conducted to establish if the SOM could classify map patterns by either of the two previously

mentioned criteria: (i) by season, or (ii) by mean wind direction. For each trial, the SOM neighbourhood function was always set to 'Gaussian', and the number of iterations was set to 500 times the length of the input vector, as per Skific and Francis (2018). Other SOM parameters such as the learning rate, neighbourhood distance decay, the training method, and the initial weights, were all adjusted during the multiple trials within guidance from the literature and online sources.

The size and shape of the SOM was also manipulated to observe its influence on SOM performance. I define a saturated SOM as one whereby multiple input vectors are clustered onto a smaller number of nodes than there are vectors. This is the typical way many SOM projections are used when there are hundreds or thousands of observations. However, another method is to use a sparsely populated SOM, where there are more nodes than input vectors. This allows the investigator to observe the spatial clustering of observations in a clearer fashion.

The SOM failed to classify the larger domain synoptic patterns with any type of success based on the above two criteria. Figure 4.3.7 shows the spatial distribution on a sparsely populated SOM whereby the observations are labelled by the mean wind direction during the events, and colour-coded depending on the season in which the event occurred. Westerly events are distributed along the right-hand edge, and through the middle section on the left of the map. Little coherence is observed in this pattern and the 10 westerly events are scattered among the easterly events. As expected, the SOM did not cluster events by season, as colours appear distributed across the map arbitrarily. The grey-scale shading used on each node is known as the distance map. Here, each node is compared to the surrounding nodes and the similarity measured as a form of distance. It can be interpreted by areas on the map where the white or light grey represent clusters that are similar, and the darker grey areas represent the division between these clusters.

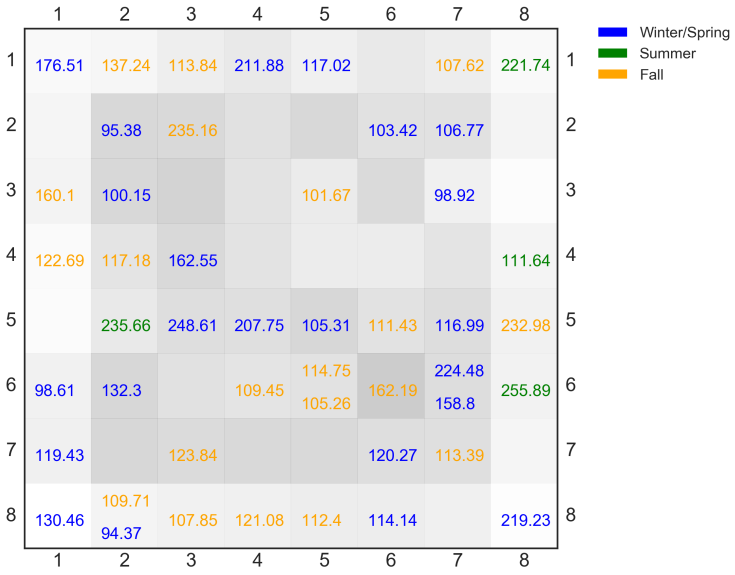

Figure 4.3.7: An attempt to cluster 47 input vectors derived from 925 and 500 hPa geopotential height anomalies using a sparsely populated 8×8 SOM, using the larger domain outlined in section 4.2.4. Input vectors are labelled by the mean wind direction during each event, text colour represents the wind season in which the event occurred. Grey-scale shading on each node represents the SOM distance map, where darker shading indicates larger differences between adjacent node weights and light shading indicates smaller differences between adjacent node weights

It was decided the approach used to this point, which followed many climate-to-environment examples provided in the literature, was not appropriate for a low-observation environment-to-climate analysis. Since the primary influence on the mean wind direction during each episode was the direction of the pressure gradient over Quesnel Lake, it was decided to place Quesnel Lake at the centre of a smaller domain. The size of the domain was influenced by the fact that a SOM performs best when there are fewer data-points and more observations. Changing from the larger domain to the smaller domain decreased the number of data-points from 1710 (using the $2.5^\circ \times 2.5^\circ$ grid) to 234 (using a $1.5^\circ \times 1.5^\circ$ grid). The SOM also requires iteration values in the order of 500 times the length of an input vector, therefore using a smaller domain was also less computationally intensive.

Multiple trials were conducted with the new input vectors to test a variety of input param-

eters and SOM dimensions. The successful 4×3 SOM used a learning rate of 0.35 and a distance decay value of 1.0. Applying random initial weights gave better results than using weights derived from a principal component analysis (PCA), as did using a random training method in place of the batch training method. The trained SOM will be referred to as the master SOM from hereon. This is common practice as many other SOM variations can be derived from the successful master SOM configuration. The nodes are designated by row and column locations on the map, making the top left node (1,1) and the bottom right node (4,3).

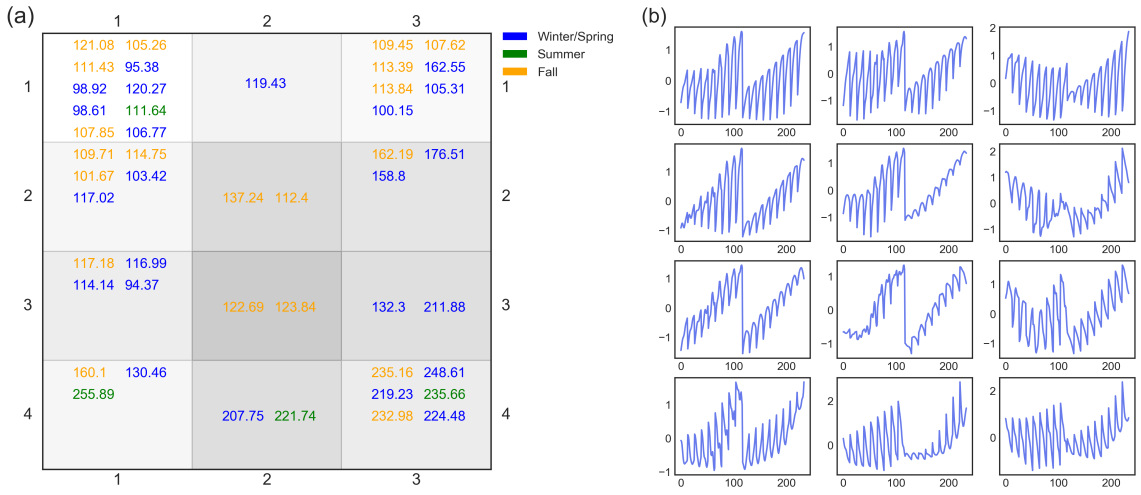

Figure 4.3.8: Two views of the 4×3 master SOM for 925 and 500 hPa geopotential height anomalies during 47 strong wind events. (a) Input vectors are labelled by the mean wind direction during each event. Text colour represents the season in which the event occurred. (b) The resultant output vector is the mean of the input vectors clustered at each node. The discontinuity midway through each output vector arises from the concatenation of the 925 and 500 hPa geopotential height anomaly fields

Fig.4.3.8a illustrates how the (subjective) success of the master SOM was measured. There is a clear distinction between easterly events, clustered primarily along the left and top of the map, and the westerly events that are clustered to the bottom right. Again, the seasonality of events is not captured by the SOM, but this was expected after the manual classification. Therefore, the SOM is not revealing new information, but allowing the projection of

all the possible synoptic states that drive strong wind events at Quesnel Lake, classifying them by the alignment of the pressure gradient over the region. Where events are clustered together on nodes (e.g., nodes (1,1), (1,3), (2,1), and (4,3)) the SOM has determined that the input vectors are similar.

To visualize the cluster of events at each node of the SOM, the output vectors are derived by taking the mean of the input vectors situated at each location. These output vectors are displayed in Fig. 4.3.8b. The vectors are split into two, $1.5^\circ \times 1.5^\circ$ grids of 925 and 500 hPa geopotential height anomalies are reconstructed from the two output vector components (Fig. 4.3.9).

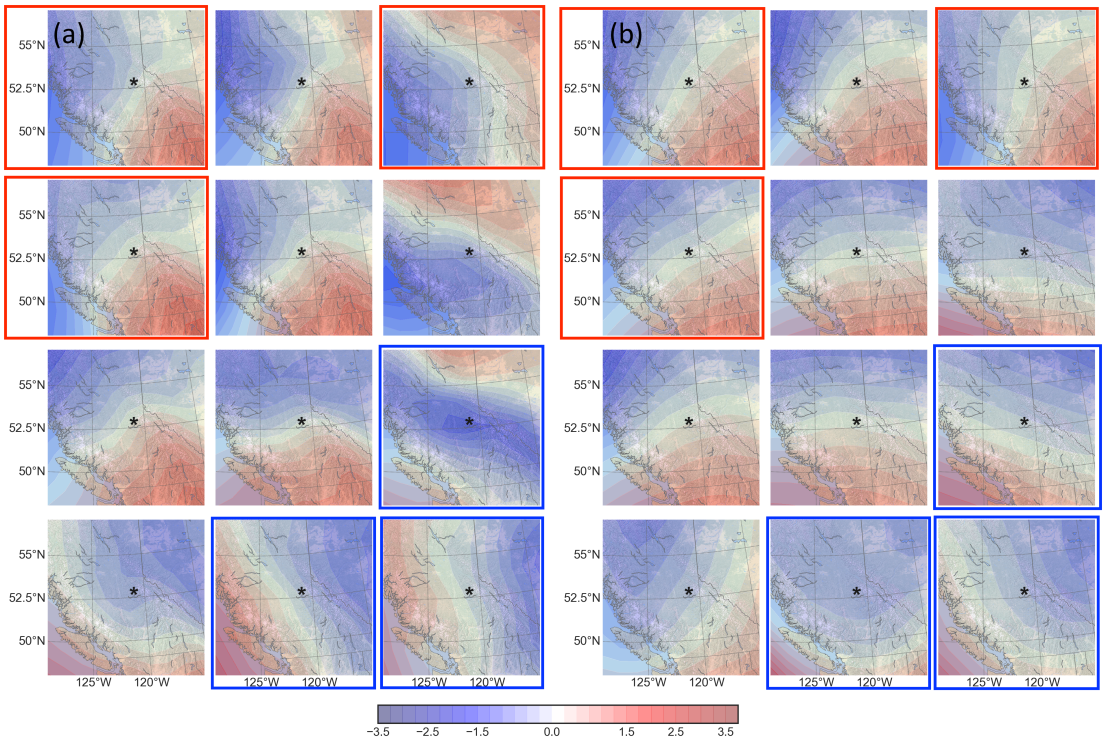

Figure 4.3.9: The 4×3 master SOM of (a) 925 hPa, and (b) 500 hPa geopotential height anomalies, derived from the output vectors displayed in Figure 4.3.8. Anomaly increments (unitless) are 0.25 per shaded contour. Red boxes indicate clusters of multiple easterly wind episodes, blue boxes represent the same for westerly events

To quantify the amount of variance explained by the output vectors, the number of easterly

0.270	0.027	0.189
0.135	0.054	0.081
0.108	0.054	0.027 0.100
0.054 0.100	0.200	0.600

Figure 4.3.10: Fraction of events clustered at each node in the 4×3 master SOM, partitioned into easterlies (red) and westerlies (blue)

and/or westerly events at each node was divided by the total number easterly or westerly events, respectively (Fig. 4.3.10). Red (for easterlies) and blue (for westerlies) boxes are used from Fig. 4.3.9 onward to denote the three nodes that account for the greatest number of events per classification. Nodes (1,1) (27.0%), (1,3) (18.9%), and (2,1) (13.5%), account for a total of 59.4% of the variance in easterly episodes. The rest of the easterly events are distributed across the remainder of the SOM except at nodes (1,3) and (2,1). The output vectors at nodes (4,2) and (4,3) represent 80% of the total variance of the westerly events, with the vectors at nodes (4,1) and (3,3) representing 10% each. I have given more weight to the westerly event at node (3,3) due to the lower amount of easterly events assigned to the same node, hence the inclusion of a blue box here but not at node (4,1).

The synoptic patterns of the larger domain were then projected onto a 4×3 grid using the master SOM as a template. Figs. 4.3.11 to 4.3.13 display the mean of synoptic patterns clustered at each node, for the three pressure levels of 925, 800, and 500 hPa. The focus of this exercise was to project the variety of larger-domain patterns that contribute to each type of strong wind event. The resultant three SOMs of synoptic patterns cover the entire continuum of the input data, rather than a limited number of discrete realizations. This output is analogous to the result of a manual analysis, however, the variance in the location

of synoptic features can be visualized by the reader more efficiently than deciphering the text usually associated with a manual classification.

As described in Section 4.3.2., the three main easterly nodes ((1,1), (1,3) and (2,1)) are all dominated by a closed low off the coast of BC at 925 and 800 hPa (Figs. 4.3.11 and 4.3.12), with an associated shortwave trough at 500 hPa (Fig. 4.3.13). Ridging to the west of BC that is fundamental for the west-east pressure gradient associated with strong westerly events is evident at all three levels in the three westerly nodes ((3,3), (4,2) and (4,3)) (Fig. 4.3.11). Nodes that do not have red or blue boxes around them represent outliers or patterns that defy physical interpretation. For example, node (1,2) represents a strong low-pressure system that although realistic, has low probability of occurrence (i.e., 1 out of 47). Whereas the averaging of easterly and westerly events at node (4,1) results in a pattern that is unlikely in real-world atmospheric flow.

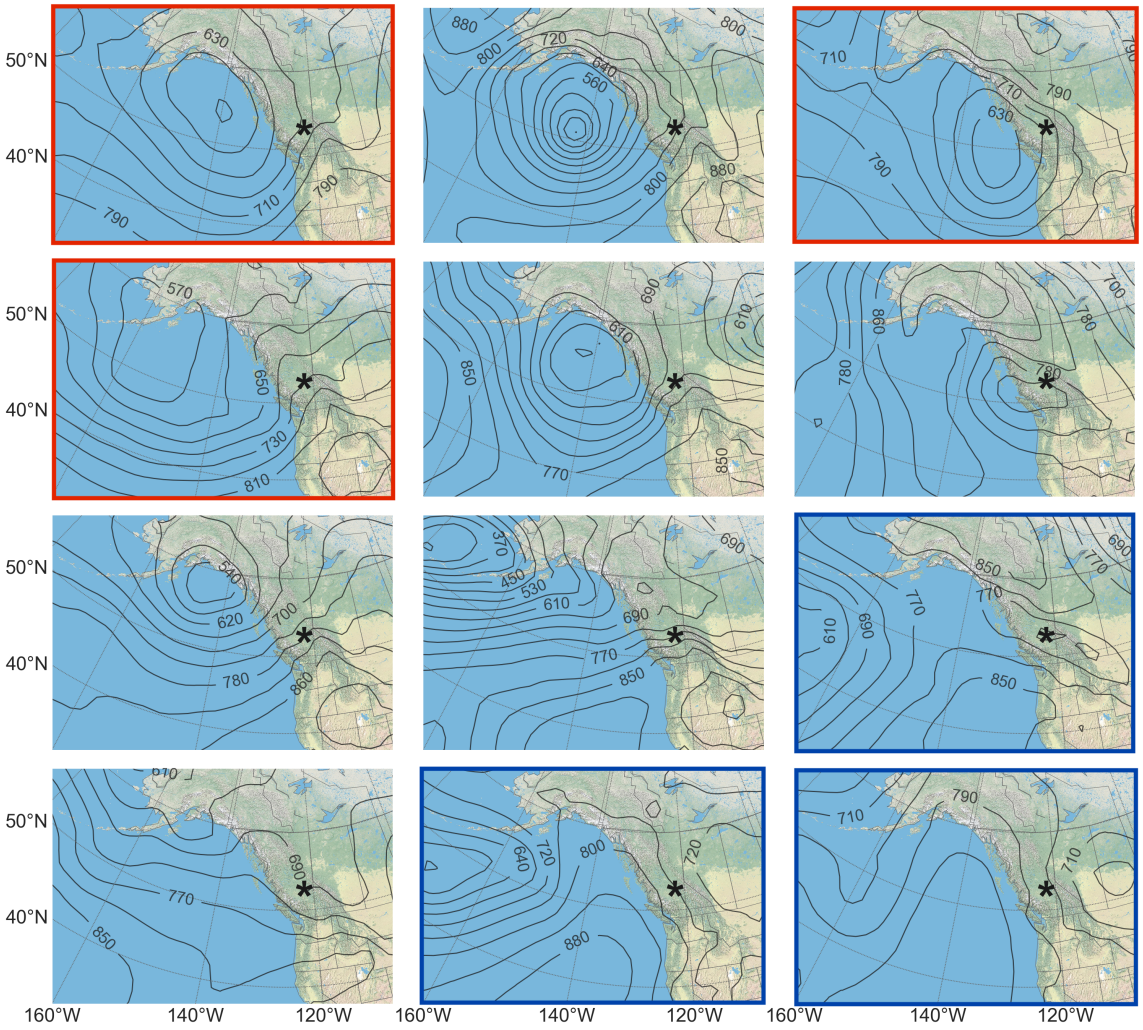

Figure 4.3.11: The projection of clustered 925 hPa geopotential height patterns using the master SOM template. All heights are in metres (m). Panels outlined in red (easterlies) and blue (westerlies) represent patterns that explain the majority of the input variance, as outlined in section 4.3.3

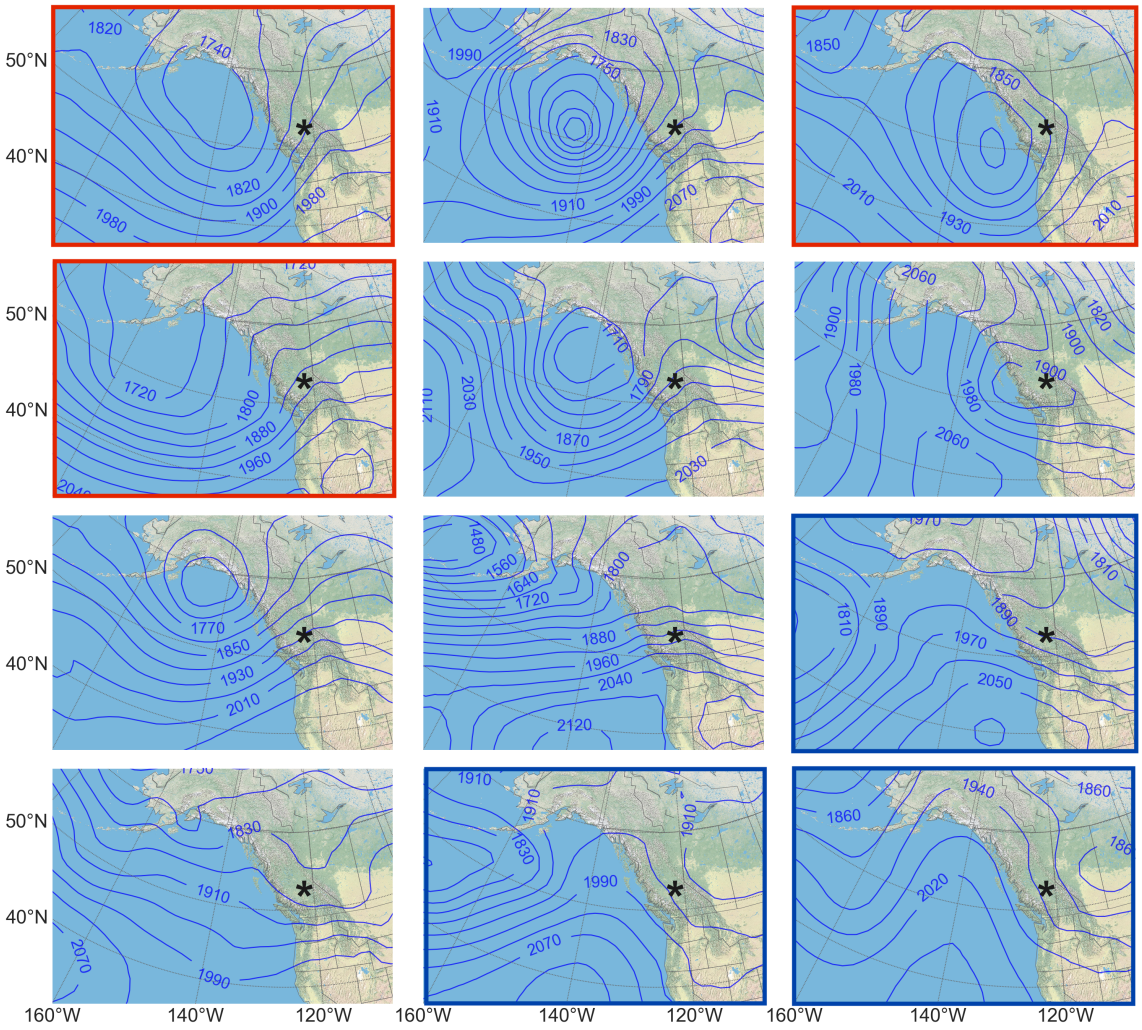

Figure 4.3.12: As Fig. 4.3.11 using 800 hPa geopotential height patterns

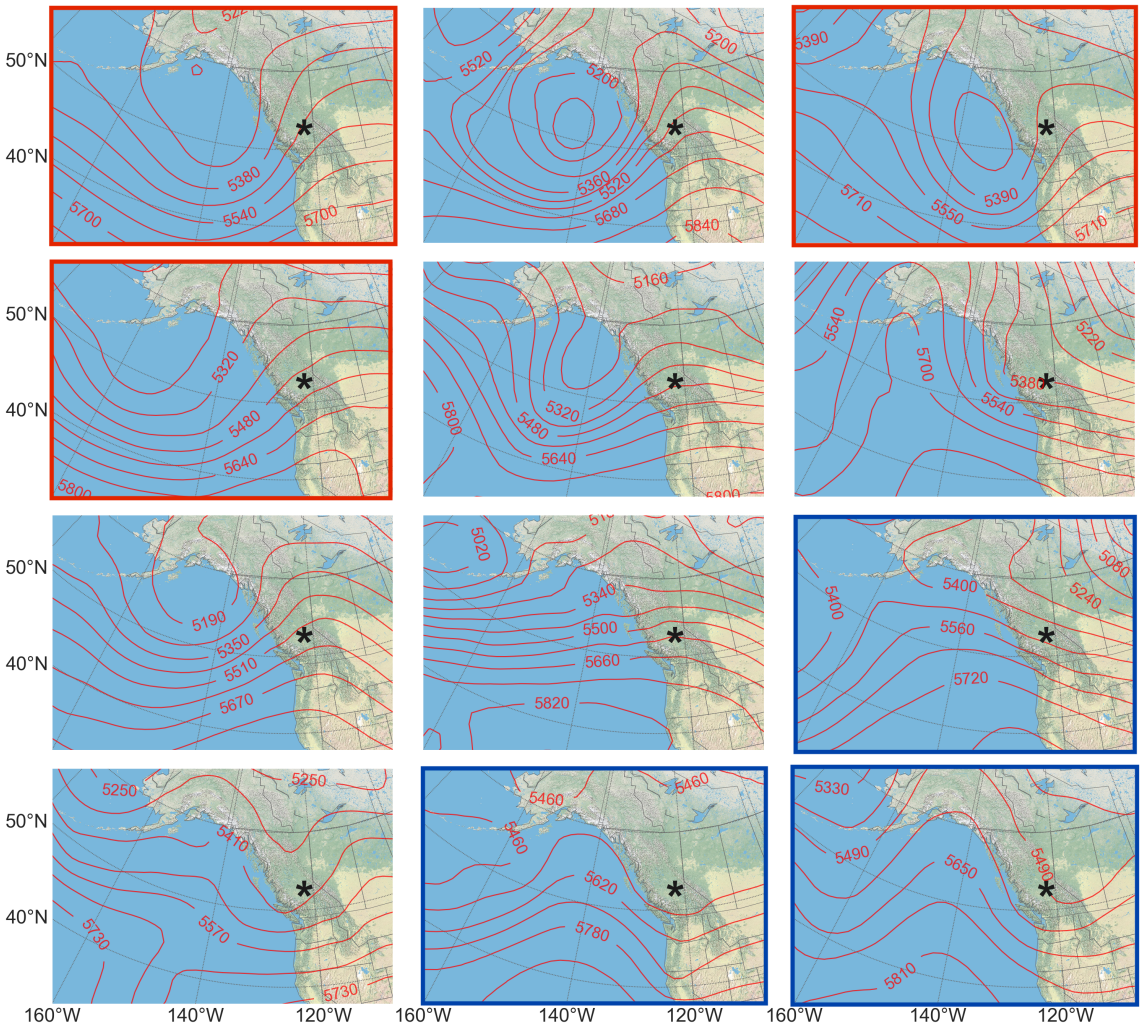

Figure 4.3.13: As Fig. 4.3.11 using 500 hPa geopotential height patterns

4.3.4 Case studies of known periods of interest

Many subjective judgments have been employed in the detection and analysis of the strong wind episodes, the manual analysis of synoptic patterns, and the success of the master SOM. Therefore, an attempt at validating the methods used in this analysis has been performed by comparing the results to-date with two episodes of strong winds at Quesnel Lake that are known to have excited a hydrodynamic response.

The first case comes from previous research by Laval et al. (2008), where westerly winds generated a periodic baroclinic seiche response in the West Basin during August 2003. The date and timing of the wind episode are taken directly from the literature, which results in 0000 UTC 3 August 2003, as being T-0 (Fig. 4.3.14). Due to this being outside the analysis period, the methods for detecting strong wind episodes cannot be compared in this case.

The second case originates from high bottom layer velocities observed by a UBC research group in the West Basin of Quesnel Lake. Here, easterly winds are believed to have moved surface water towards the outlet of the Quesnel River creating currents at the bottom of the basin (B. Granger, personal communication, 29 September 2018). Peak bottom layer velocities were observed at 0800 UTC 26 November 2016. Therefore I will use the closest synoptic hour of 0600 UTC 26 November 2016, as T-0 (Fig. 4.3.15).

This event is identified by the data filtering method described in section 4.2.1, and is listed in Appendix A as episode # 10. Using the wind stress method the time for T-0 (maximum wind stress) was 0600 UTC 24 November 2016; 46 hours prior to the peak bottom layer velocities. The duration of the event was 64 hours, ending at 0800 UTC 25 November 2016, still 22 hours before the peak bottom layer velocities were observed. However, examining the physical relationship between the peak wind stress and the hydrodynamic response is

beyond the scope of this thesis.

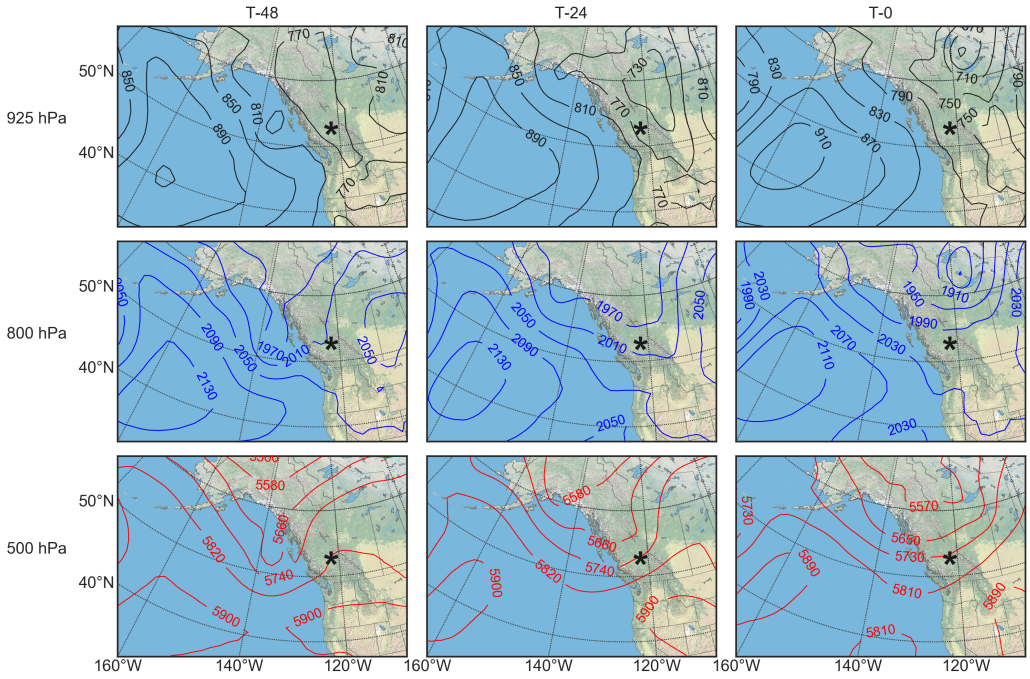

Figure 4.3.14: Synoptic patterns for a known strong westerly wind event at Quesnel Lake from 0000 UTC 1 August 2003 (T-48) to 0000 UTC 3 August 2003 (T-0). Panel arrangement is the same as per Figs. 4.3.4 and 4.3.5

The westerly event in August 2003 results from the combination of a weak high pressure system in the Gulf of Alaska and a closed low northeast of northern BC, observed at 925 hPa and 800 hPa (Fig. 4.3.14). This is supported in the mid-troposphere by the broad ridge west of the BC coast and the shortwave trough located above the surface low. These combinations induce a west-to-east pressure gradient observed over most of BC. The weakness of the ridge and length of the associated long wave are noticeably different to the other previously identified westerly events. However, the associated pressure gradient observed across the smaller domain is akin to the mean of patterns clustered at node (4,2) in the master SOM (Fig. 4.3.16).

The easterly event in November 2016 follows the pattern of an intense low pressure ap-

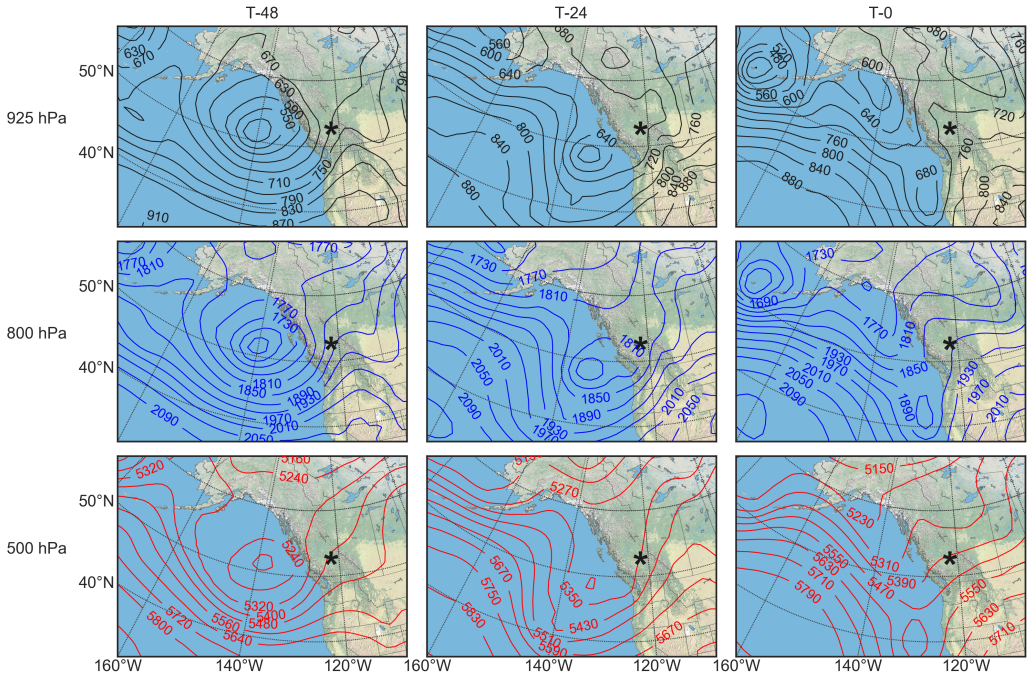

Figure 4.3.15: Same as Fig. 4.3.14 for a strong easterly event from 0600 UTC 24 November 2016 (T-48) to 0600 UTC 26 November 2016 (T-0)

proaching the coast of BC, either originating, or having been strengthened by, the Aleutian low (Fig. 4.3.15). In the 500 hPa pattern the surface low extends to the mid-troposphere at T-48, then weakens to a shortwave trough at T-24. Of note is the trajectory of the system, whereby the SE movement of the storm prevents it passing directly over central BC. This is important for the persistence of the strong wind episode, which otherwise would have had a shorter duration, and a probable wind shift after the passage of the cold front. The intensity of the pressure gradient surrounding the closed low at T-48 and T-24 compared to T-0 is also interesting considering that T-0 in this instance represents the occurrence of peak hydrodynamic response observed in the lake. At T-0 the low appears to have already begun to dissipate, possibly due orographic effects as the system made landfall, yet this time-lag raises pertinent questions about how the lake responds to wind forcing in the hours and days after its application.

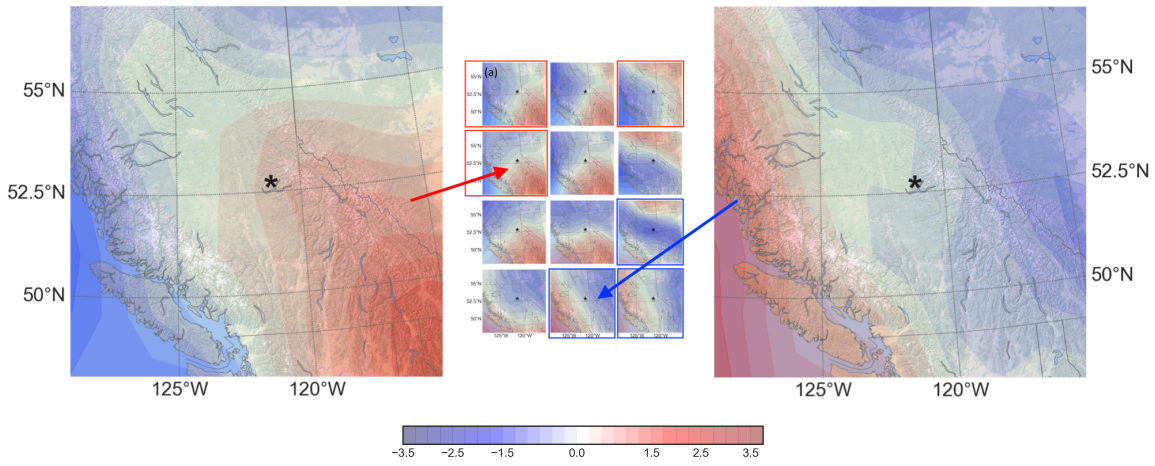

Figure 4.3.16: Winning nodes on the master SOM for the two case study events outlined in section 4.3.4. The easterly event (left) was allocated to node (2,1); the westerly event (right) to node (4,2). The centre image comes from Fig. 4.3.9a. All panels are of standardized 925 hPa geopotential height anomalies, and shaded contours are in 0.25 (unitless) increments

A trained master SOM can evaluate further data by assigning any new vectors to a 'winning' node on the map. This is achieved by the SOM computing which node has the smallest Euclidean distance from the new input vector. SOM input vectors for the two cases mentioned above were constructed using the methods described in section 4.2.6 (using the smaller domain). These were then evaluated by the master SOM and allocated to the appropriate nodes. This technique is not an infallible validation method, as the SOM will always allocate the new observation to a node on the map rather than reject it, complicating the analysis. However, the easterly event was allocated to node (2,1), and the westerly event to node (4,2) (Fig. 4.3.16), both of which had already been identified as significant in section 4.3.3.

4.4 Discussion

By filtering hourly wind stress data to identify episodes of strong winds at Quesnel Lake, I have been able to compile a synoptic climatology for the large-scale atmospheric patterns

that drive these events. Over a two-year period (1 October 2016 to 30 September 2018), there were 37 episodes of strong easterly winds, compared to 10 westerly events. Episodes last for an average duration of 47 hours. Easterly episodes are possible during all seasons, with peaks in the Spring (March) and Fall (November). Westerly events also occur throughout the year, but dominate during June and July. No events were observed during August or September. The mean wind direction of all episodes fall between 90° and 270°, highlighting the topographic effects of the surrounding Cariboo Mountains.

Manual analysis of the synoptic patterns at three time steps (T-48, T-24, and T-0) and three pressure levels (925, 800, and 500 hPa) was conducted, and composites assembled from the mean of each type of event (easterly versus westerly). The easterly composite reveals the influence of developing low pressure systems from the Gulf of Alaska have on the pressure gradient over central BC. The east-to-west set-up persists as the systems track southeast, allowing the wind stress on the lake to accrue. Westerly winds develop with strong ridging in the lower to mid troposphere, to the west of the BC coast. This is at times assisted by the passage of a shortwave trough over central BC, exacerbating the west-to-east pressure gradient.

To visualize the full array of atmospheric patterns a SOM was used to project the synoptic maps and to cluster episodes that the algorithm deemed similar. The resultant 4×3 master SOM is able to allocate every input vector to a node, therefore spanning the full data space of observations, an advantage the technique has over other non-hierarchical clustering methods. Two separate regions of nodes were identified as being significant for the easterly and westerly episodes, explaining 59% and 90% of the variances, respectively.

Finally, two case studies of strong wind events known to drive internal hydrodynamic processes within the lake are examined, and used to validate the data filtering, manual synoptic analysis, and SOM projection methods. The case studies allowed for an analysis of one

easterly and one westerly episode. The easterly event provided justification for the data filtering methods, yet also highlighted the further research required to couple the timing of peak wind stress with the lake's response. For both cases, the resulting synoptic patterns show good agreement with the manual analysis and the SOM results. Both events were able to be allocated to nodes on the SOM already highlighted for their significance in the ability to explain variance within the synoptic dataset.

5 Spatial and temporal variability

5.1 Introduction

The variability of wind in mountainous locations is governed by thermal and mechanical forcings on a variety of scales. Local thermally-induced circulations (typically) arise during summer periods, when synoptic forcing is weak and radiative effects are dominant. Superimposed on these small-scale winds may be regional-scale flows such as valley-mountain winds or mountain basin circulations. The diurnal cycle of these upslope/downslope flows on any scale may be disturbed by the passing of a larger-scale synoptic system (Whiteman, 2000).

While the wind field across the Quesnel Lake basin experiences some of the idealized mountain wind circulations as described by Whiteman (2000) and Barry (2008), the qualification of when and where these circulations occur is still unknown. In addition to this, the channelling of winds by the surrounding topography may have a profound effect on hydrodynamic circulations within the lake. Quesnel Lake's intersecting basins makes modelling the lake's response to wind forcing a complex task that relies on an appropriate representation of the wind stress across the lake surface (Hodges et al., 2000; Valerio et al., 2017; Brenner, 2017). This wind stress field throughout Quesnel Lake is also poorly understood.

A variety of topographic effects on the local wind field arises due to the complexity of the landscape surrounding Quesnel Lake. Elevations range from 728 masl at lake-level to 2597 masl at the peak of Mount Wotzke. This elevation range provides contrasting climatic environments in spring and early summer when snow is absent from the valley floors, yet is still present on the lee-side of ridge tops and high peaks (Déry et al., 2010; Sharma and Déry, 2016). The steeply sided valleys of the north and east arms exacerbate summer-time

radiative effects, and may interact with synoptic flows to enhance both forced channelling and pressure-gradient channelling along their lengths (see Ryan, 1977; Whiteman, 2000). This complexity of terrain is in contrast to the rolling hills leading to the southern shores of Quesnel Lake's main basin, which allow southerly winds to arrive at the lake relatively unimpeded.

This chapter will be a first attempt at resolving this spatial and temporal variability using data from late-summer and fall 2018. An absolute guide to the complete wind field of Quesnel Lake is not expected until at least a full 12 months of data can be collected from each region of the lake (see section 5.2). Although measurements from individual locations can only provide evidence for localized wind phenomena, they can contribute to the construction of a theoretical framework of the wind field, and eventually to the validation of numerical models.

5.2 Data and Methods

The analysis presented in this chapter utilizes data from six CAMnet stations in the vicinity of Quesnel Lake, over a period of 109 days from 4 August 2018 to 20 November 2018. Five of the stations are shore-based installations that create an array covering each portion of the lake. Using the local nomenclature adopted by other researchers at Quesnel Lake the various basins and their respective CAMnet stations are: (i) the East Arm (Dock Point), (ii) the North Arm (Long Creek, Goose Point), (iii) the Main Basin (Plato Point), and (iv) the West Basin (Raft Creek) (Figs. 2.1.1 and 5.3.2). Another region of interest is an area known as the Junction, located where the east and north arms intersect the main basin, however, it has been difficult to find a suitable location for installing a meteorological station in this area. I have included data for the same period from Browntop Mountain to allow a comparison with the lake-level datasets and to provide an estimate of above-ridgetop wind

conditions.

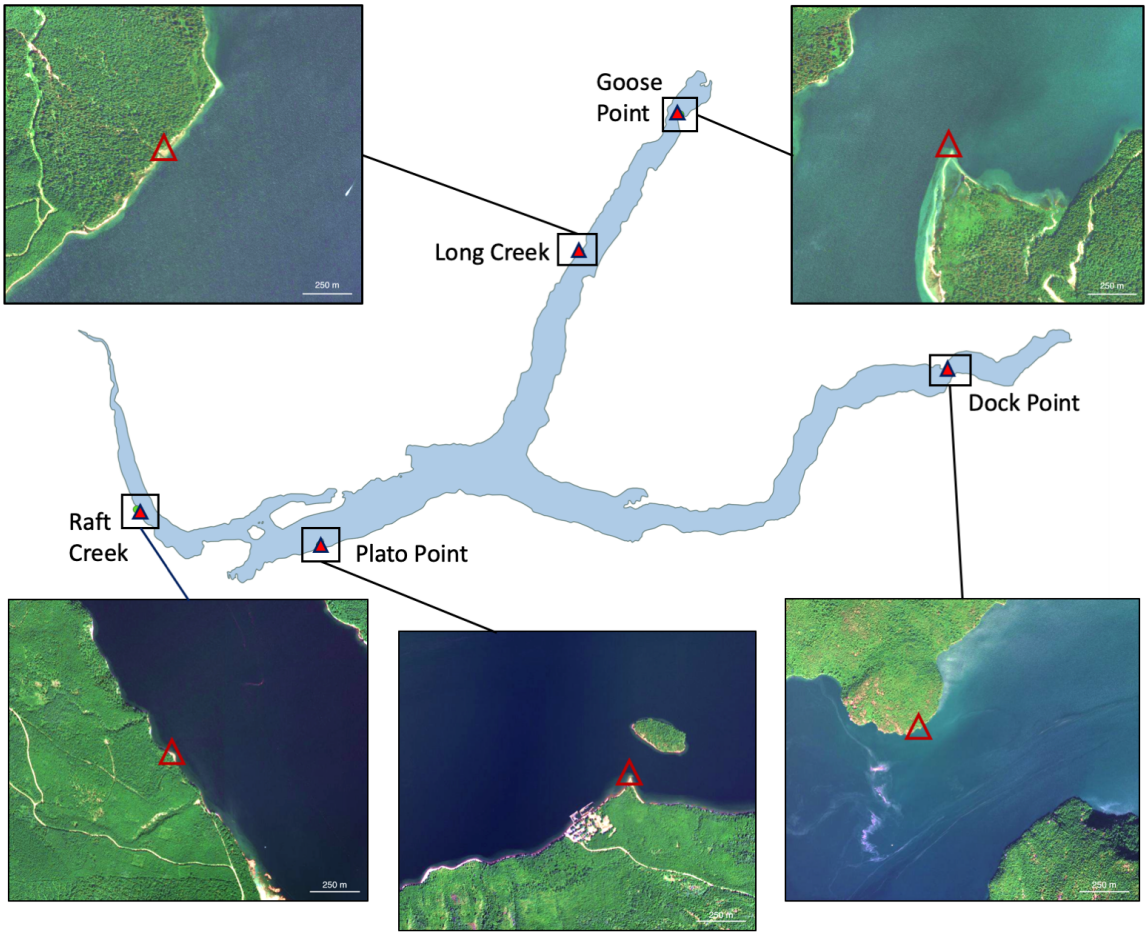

Figure 5.2.1: Enhanced true-colour satellite imagery of the five lake-level CAM-net stations. Red triangles denote the location of each station. Bing Maps screen shots reprinted with permission from Microsoft Corporation (2019). Retrieved from *https://www.bing.com/maps*

The Raft Creek station was unfortunately damaged during a suspected wildlife encounter on 12 October 2018. The resulting timeseries comprises 6624 observations covering the 69 days from 4 August 2018 to 11 October 2018. There is less than 0.1% of data missing from this dataset. Out of a potential 10,464 15-minute observations the other five stations were missing: Goose Point: 2.4%, Dock Point: 0.5%, Plato Point: 0.0%, Long Creek:

0.4%, and Browntop Mountain: 2.7%. Some of these data were removed manually when icing on the anemometer was suspected to have contributed to false recordings of 0.0 m s^{-1} (e.g., Browntop Mountain in mid-November). Calms are defined as periods of wind speeds less than 0.5 m s^{-1}, as per methods used by Tuller (2004) and Eckman (1998). Calms are retained in the dataset as they provide significant influence over the mean wind speed and CV values. The positioning and instrumentation of each station is not uniform across the six locations (see Table 1), therefore, intensive comparisons of the absolute magnitude and direction of the wind at each site is discouraged. The adjustment of wind speeds to a standard reference height has been common practise in similar studies (e.g., Rueda et al., 2009; Déry et al., 2010), however, due the diversity of surfaces and surrounding vegetation types it was not attempted here. The response at each location to increasing or decreasing wind speeds, and wind directions relative to the channel axis will be the primary focus throughout this chapter. Nonetheless, I will briefly summarize each location's site characteristics and relate these to the observed wind data to provide extra context for the reader.

The initial wind speed and direction analysis utilized wind speed histograms with 0.5 m s^{-1}bins (1 m $s^{-1}$for Browntop Mountain) and windroses constructed using the format outlined in section 3.3.1. Descriptive statistics (mean, standard deviation, and CV) of the 15-minute wind speed dataset were calculated for each station. The mean wind direction was calculated using circular statistics and the variability of wind directions is represented by the circular standard deviation. Where the wind direction distribution appears bi- or tri-modal the prominent peaks of the distribution have been reported.

Next, the 15-minute wind speed timeseries was smoothed using a 24-hour moving average to calculate the lead/lag Spearman-rank correlation coefficients between each station. The timeseries for each station was trimmed to match the dataset from Raft Creek when cor-

relation with this station was calculated. The lead/lag times are reported in hours and had been tested over a range of -12 to +12 hours.

I predicted that local-scale circulations as outlined by Whiteman (2000) could exist due to thermal forcing, interaction of the above-ridgetop winds with the topography, or a combination of the two. To examine this, each station's 15-minute wind speed timeseries was normalized by division of the period mean and the wind speed power spectra computed using a discrete Fourier transform. The resulting power spectra density plots span frequencies of 30 minutes to 106 days. To supplement the spectral analysis, the diurnal wind speed pattern was analyzed using a daily profile derived from the normalized timeseries. To explicitly view how wind speeds and directions varied over an average 24-hour period the continuous distributions were derived using a gaussian kernel density estimation and plotted as a function of the time of day.

Periods of weak synoptic forcing when thermally-induced local circulations were believed to be dominant have been analyzed in an attempt to describe the typical wind regimes at each location. The week of 27 August 2018 to 2 September 2018 is presented as an example of one such period. Finally, two episodes of (relatively) strong winds are investigated to explore the coherence in the basin-scale response to synoptic forcing. Directional vectors for the 925 hPa and 800 hPa geopotential height gradients from the ECMWF dataset outlined in Section 4.2.4 have been used to illustrate the synoptic forcing present during these strong wind events.

5.3 Results

5.3.1 Wind speeds and directions

Raft Creek

Raft Creek's low mean wind speed exemplifies the difficulty in locating ideal sites for meteorological stations along the shores of Quesnel Lake, with $\sim 180^{\circ}$ of the site's horizontal field-of-view (to the southwest) being mature forest. Despite this, the tri-directional distribution of the windrose indicates that multiple local circulations may be present at this location (Fig. 5.3.1). The largest percentage of winds originates from southwest to south-southwest, yet are always below 2 m s^{-1}. These directions are dominated by the forested slopes of the valley as they rise away from the lake shore. Winds of any greater velocity are observed to be channelled up the West Basin from the southeast, or down the basin from the northwest.

Plato Point

Plato Point experiences wind primarily from southerly aspects due to the gentler relief in the surrounding terrain, compared to the other lake-level stations. However, stronger winds (above 5 m s^{-1}) have a distinct westerly or easterly nature to them (see Section 4.3.1). Notable is the absence of any northerly winds despite the station facing the open water of the main basin (Fig. 5.3.2). This illustrates (i) the sheltering effects of the steep topography on the north side of the main basin, and (ii) the channelling of northwesterly winds down the west basin resulting in the westerly flow through the main basin observed by Laval et al. (2008). Wind speeds are marginally stronger than in the North Arm and West Basin, however, a CV of 0.91 is the same as both Long Creek and Raft Creek indicating that the wind regimes of the three sites may be similar (Table 10).

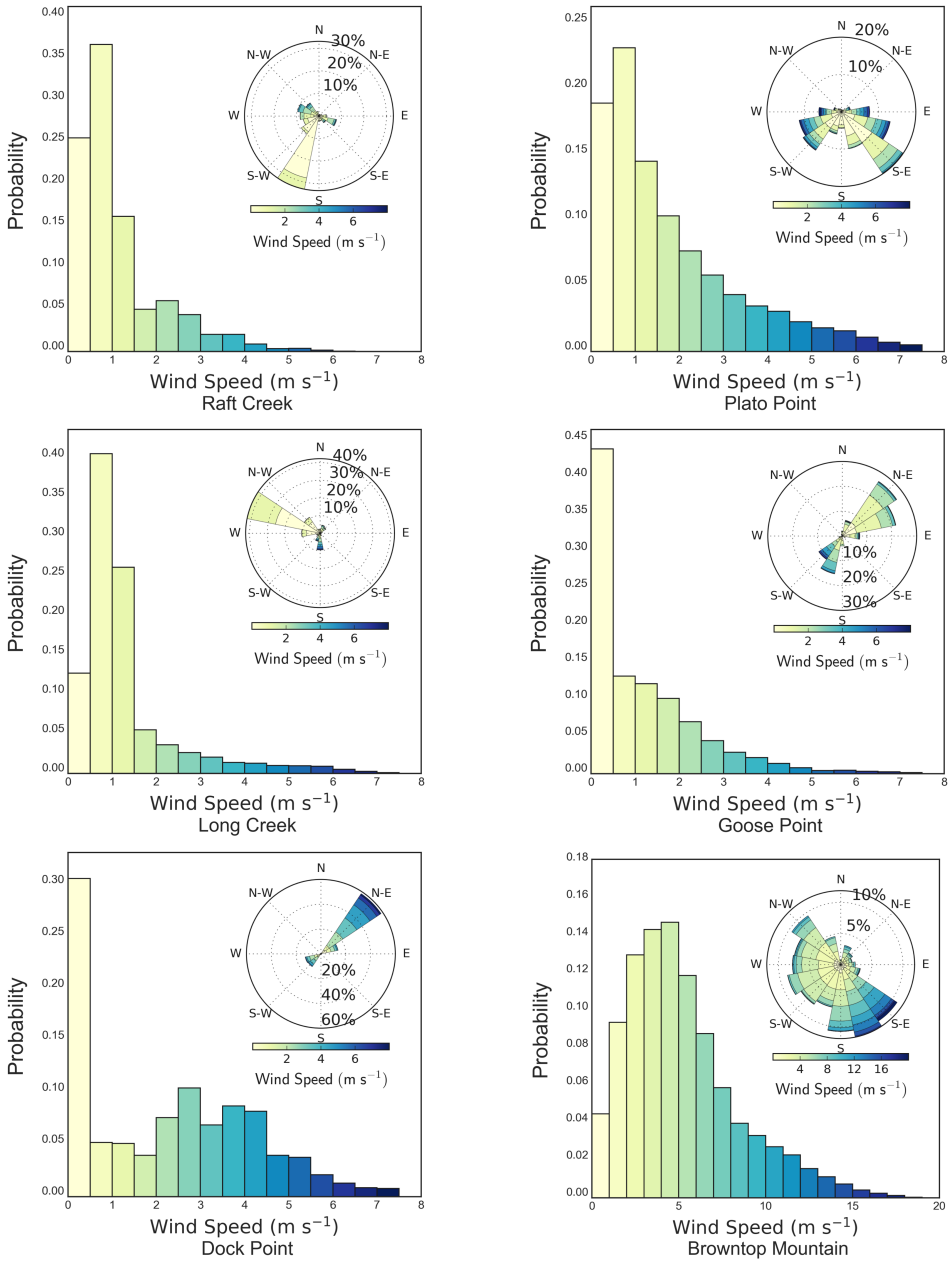

Figure 5.3.1: Wind speed distributions and windroses for six CAMnet stations neighbouring Quesnel Lake using 10,464 15-minute observations from 4 August 2018 to 20 November 2018 (6624 observations from 4 August 2018 to 11 October 2018 for Raft Creek). Note the higher wind speed scale (x-axis) for Browntop Mountain, and the differences in probability values (y-axis) across the six panels

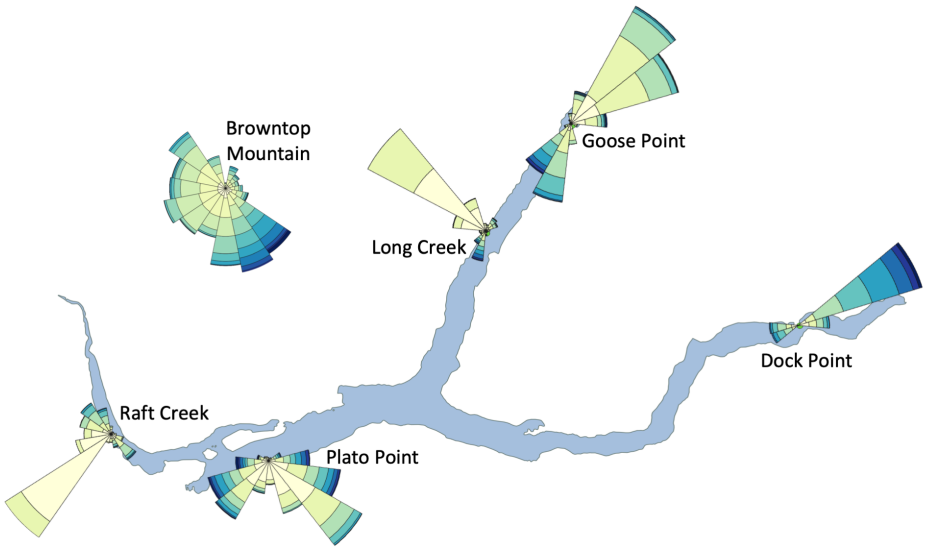

Figure 5.3.2: Windroses from Fig. 5.3.1 superimposed onto an outline of Quesnel Lake. Windroses are composed of 15-minute wind data collected from 4 August to 20 November 2018 (4 August 2018 to 11 October 2018 for Raft Creek)

Long Creek and Goose Point

The Long Creek wind speed and direction distributions display the prevalence of light downslope winds from the northwest, in the same manner as Raft Creek's persistent light southwesterlies. Stronger winds are rare as the wind speed distribution is positively skewed, however, when they do occur they are directed either up the North Arm from the south, or down the arm from the northeast. This correlates with the channelling also observed at Goose Point, which has a strongly bi-directional windrose. Here, the prevailing wind is from the northeast (Table 11), which represents the far end of the arm. This terrain forms a large natural amphitheatre which Goose Points sits at the bottom of. The strongest winds observed at Goose Point originate from the south-southwest and have a vast stretch ($\sim$30 km) of unobstructed fetch before encountering the point. Despite these strong winds and the exposed nature of the station site, the Goose Point dataset also contains the great-

est percentage of calms, at 43.6%, a paradox which contributes to the high CV value of 1.34.

Dock Point

The Dock Point installation is perched on a rocky outcrop at the narrowest constriction of the East Arm. The acceleration of the flow due to the Venturi effect at this location is evident by the higher mean wind speed observed and saw tooth profile of the timeseries. Dock Point experiences a dipole of either calm conditions (30% of the observations) or moderate to strong winds (2.5 m s^{-1} to 7 m s^{-1}). The site infrequently sees light winds (0.5 m $s^{-1}$to 2 m s^{-1}). The channelling effect of the steep valley walls limits wind directions to along-axis orientations. The constriction at this point in the East Arm is orientated northwest to southeast, resulting in northeasterlies being the prevailing wind with the occasional periods of southwesterlies. The strongest winds observed during the period were northeasterlies originating from the far end of the arm.

Table 10: Statistics of 15-minute wind speed data collected from six CAMnet stations neighbouring Quesnel Lake from 4 August to 20 November 2018 (4 August 2018 to 11 October 2018 for Raft Creek)

Station	Mean wind speed (m s^{-1})	Wind speed σ (m s^{-1})	Wind speed CV	Percentage of calms* (%)
Raft Creek	1.09	0.99	0.91	25.6
Plato Point	1.83	1.68	0.91	18.9
Long Creek	1.32	1.19	0.91	12.7
Goose Point	0.96	1.29	1.34	43.9
Dock Point	2.27	1.65	0.85	30.6
Browntop Mountain	5.22	3.42	0.65	2.3

*Calm observed if recorded wind speed below 0.5 m s^{-1}.

Table 11: Statistics of 15-minute wind direction data collected from six CAMnet stations neighbouring Quesnel Lake from 4 August to 20 November 2018 (4 August 2018 to 11 October 2018 for Raft Creek). NA represents table entries that are 'Non Applicable'

Station	Mean wind direction (degrees)	Wind direction σ (degrees)	Direction #1 (degrees)	Direction #2 (degrees)	Direction #3 (degrees)
Raft Creek	223.9	67.2	214.4	294.6	113.0
Plato Point	168.9	69.0	124.0	239.0	NA
Long Creek	286.8	59.8	293.0	33.0	187.0
Goose Point	77.9	82.9	55.0	210.0	NA
Dock Point	51.9	70.7	54.4	238.9	NA
Browntop Mountain	213.6	87.3	NA	NA	NA

Browntop Mountain

Browntop Mountain experiences higher wind speeds and greater directional variability than any of the shore-based stations, consistent with its ridgetop location (Fig 5.3.1). The prevailing wind directions range from southeasterly through the southerly sector to northwesterly, with very few occasions of winds outside of this range. The strongest winds originate from the southeast. The CV is lowest of all six stations, in part due to the lower incidence of calms and periods with low wind speeds. The elevation of the ridgetop and the exposed location of the station results in icing of the anemometer during late fall/early winter as found by Déry et al. (2010) (Fig. 5.3.3).

5.3.2 Lagged correlation

Spearman-rank correlation tests reveal a weak significant positive correlation between all stations, apart from Long Creek and Browntop Mountain, and between Dock Point and Raft Creek, where the correlations are weak and negative (Table 12). Goose Point and Long Creek have the maximum correlation between any two locations, but this is still moderate

at 0.28, and observed when Long Creek leads Goose Point by one hour. This is an expected result given the two North Arm stations are the only two in such close proximity.

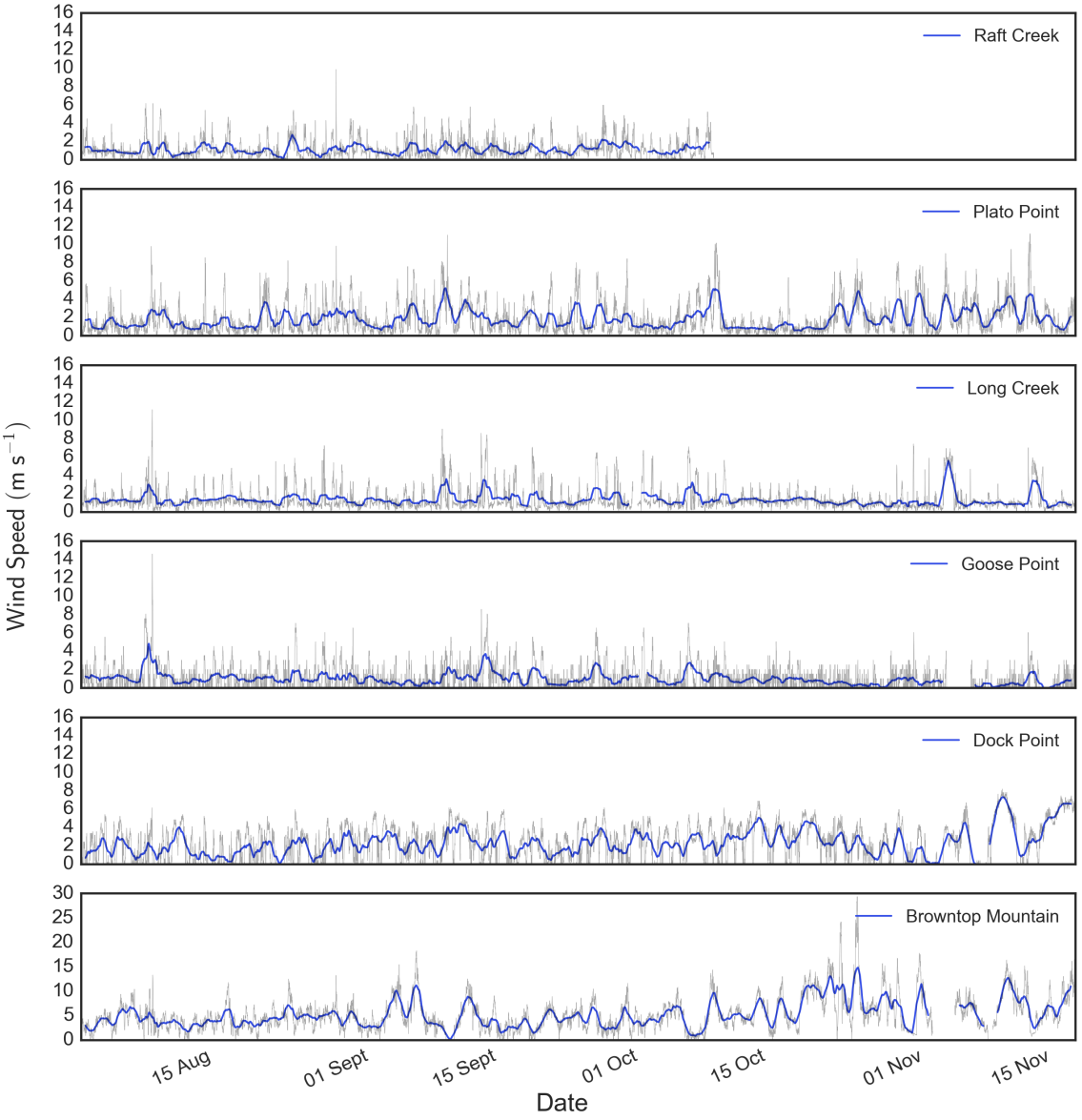

Figure 5.3.3: Wind speed timeseries from six stations in the vicinity of Quesnel Lake during 4 August 2018 to 20 November 2018. The grey trace displays the raw 15-minute wind speed data while the blue line represents a 24-hour moving average. Note the larger ordinate scale (y-axis) for Browntop Mountain due to the higher peak wind speeds

In a few isolated cases the lead/lag times associated with the correlation coefficients make

physical sense, while the remainder do not. For example, Plato Point is observed to lead Dock Point by 1.5 hours and Goose Point by 2 hours, which would be true for a hypothetical southeasterly wind. Dock Point leads Plato Point by 2 hours, also conceivable given an easterly wind. However, Long Creek leading Plato Point by 10.75 hours is most likely an artifact of the diurnal pattern rather than a representation of any physical relationship between the two sites. It is concluded that a simple lead/lag correlation test performed upon the smoothed timeseries is not an accurate method for deriving the physical relationship of the local wind field.

Table 12: Spearman-rank correlation coefficients (above the central diagonal), and the time lag of maximum correlation (below the central diagonal) for six CAMnet stations in the vicinity of Quesnel Lake

Station	Raft Creek	Goose Point	Dock Point	Plato Point	Long Creek	Browntop Mountain
Raft Creek	-	0.22	-0.10	0.11	0.21	0.24
Goose Point	-1.50	-	0.09	0.07	0.28	0.20
Dock Point	11.25	0.00	-	0.16	0.13	0.19
Plato Point	0.50	2.00	-1.00	-	0.15	0.12
Long Creek	-0.50	1.00	0.75	10.75	-	-0.13
Browntop Mountain	-8.25	3.75	0.0	-2.75	4.75	-

Note lead/lag times represent the amount of hours the station in each row either leads (positive value) or lags (negative value) the station in each column. I.e., Goose Point lags Raft Creek by 1.5 hours, whereas Plato Point leads Raft Creek by 0.50 hours. Data come from the 15-minute dataset smoothed using a moving average with a 24-hour window. Datasets have been trimmed when calculating the correlation with Raft Creek. All correlation values are significant at $p < 0.05$

5.3.3 Localized circulations

Spectral analysis of the normalized 15-minute timeseries shows that each of the lake-level stations has a peak in the power spectra density at a frequency of 1 day^{-1}, representing a cycle with a period of 24 hours (Fig. 5.3.4). Raft Creek and Dock Point also have sub-peaks at 2 day^{-1}, while both North Arm stations have sub-peaks at 2 day^{-1} and 3 day^{-1}, indicative of cycles with periods of 12 and 8 hours, respectively. The 24 and 12 hour peaks would be in agreement with Cremades et al. (1999) if they indicate a wind regime that contains two wind speed maxima per day (e.g., a land-lake breeze), however, here it is only Goose Point that follows this pattern therefore the sub-peaks observed in the Raft Creek and Dock Point datasets are most likely artifacts of the Fourier transform decomposition as identified by Déry et al. (2018). The addition of the 8 hour peak in the Long Creek spectrum could be related to the observed tri-modal shape of the wind direction distribution, but this third peak is not observed in the Raft Creek spectrum, which has a similar distribution. Browntop Mountain does not appear to show a peak at any frequency covered by this analysis.

The diurnal cycles observed at Raft Creek, Plato Point, Long Creek, and Goose Point are indicated by peak winds speeds occurring between 1200 PDT and 1600 PDT, with low wind speeds during 1800 PDT to 0600 PDT (Fig. 5.3.5). Goose point observes a secondary sub-peak in wind speeds around 0000 PDT (midnight). Wind speeds at Dock Point differ from the other four stations by building in intensity during the morning, with a peak around 1200 PDT, then decreasing during the afternoon and reaching a distinct minimum at 1800 PDT.

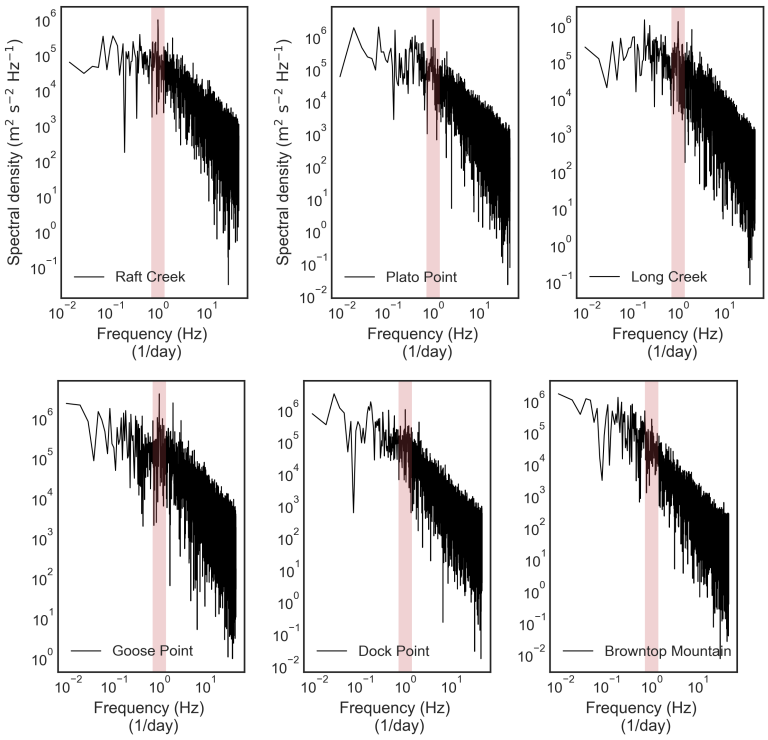

Figure 5.3.4: The wind speed power spectra density for six stations neighbouring Quesnel Lake. Input data come from the normalized 15-minute timeseries recorded at each station during 4 August 2018 to 20 November 2018 (4 August 2018 to 11 October 2018 for Raft Creek). The light red shading indicates the x-axis frequency value of 1 day^{-1}

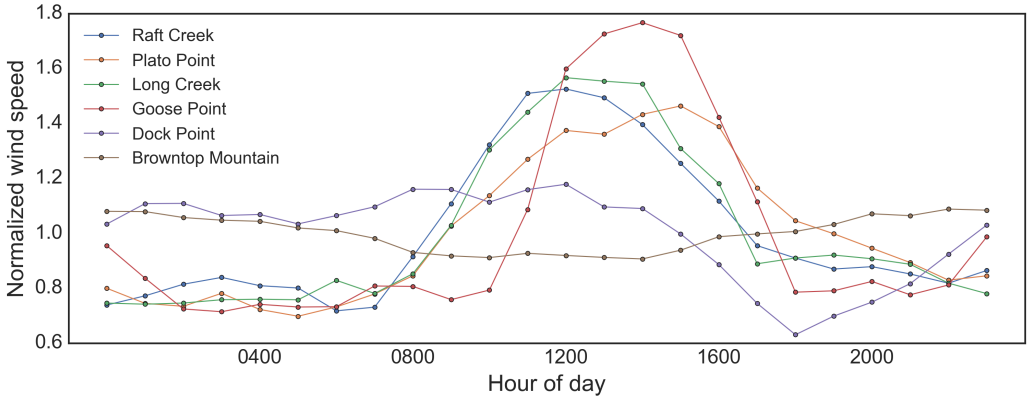

Figure 5.3.5: Profile of normalized mean hourly wind speeds from six stations in the vicinity of Quesnel Lake derived from 109 days of 15-minute observations from 4 August 2018 to 20 November 2018 (69 days from 4 August 2018 to 11 October 2018 for Raft Creek)

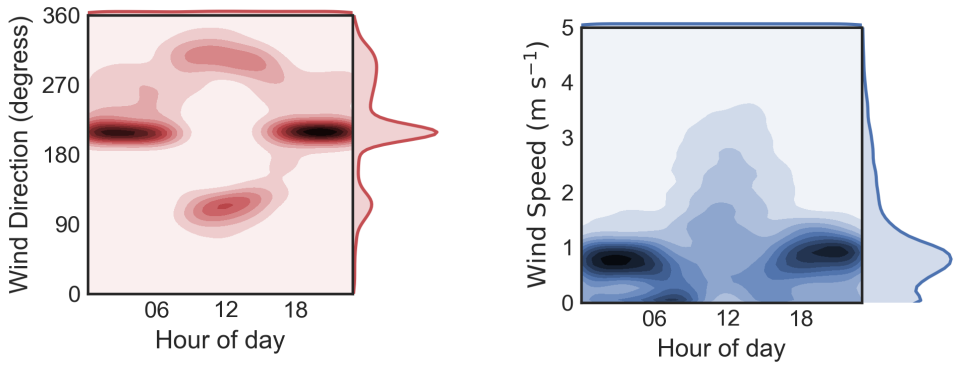

Raft Creek

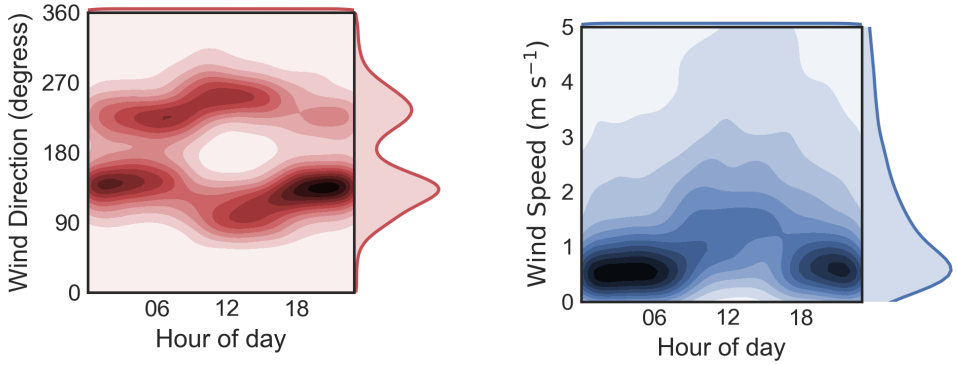

Plato Point

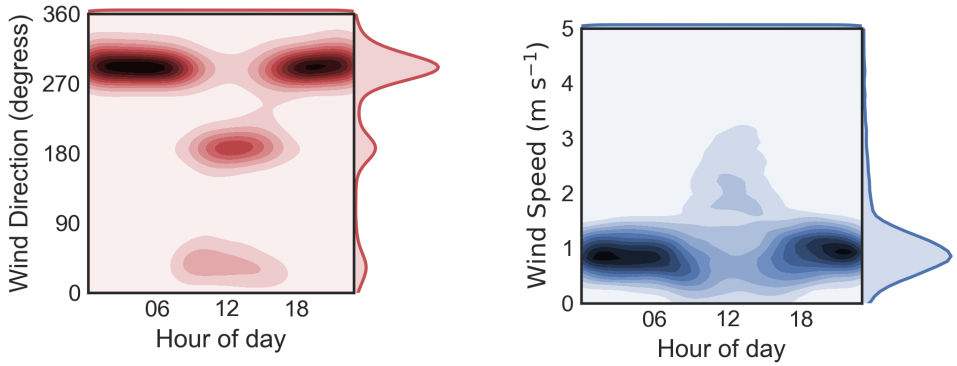

Long Creek

Figure 5.3.6: Frequency distributions of wind direction (left) and wind speed (right) plotted as a function of the local time of day (PDT). Darker shading indicates higher counts of occurrence at the time indicated on the x-axis. Kernel density estimations for the continuous distributions of each variable are along the right-hand axis of each plot. Results derive from 15-minute data collected at each station from 4 August 2018 to 20 November 2019 (4 August 2018 to 11 October 2018 for Raft Creek)

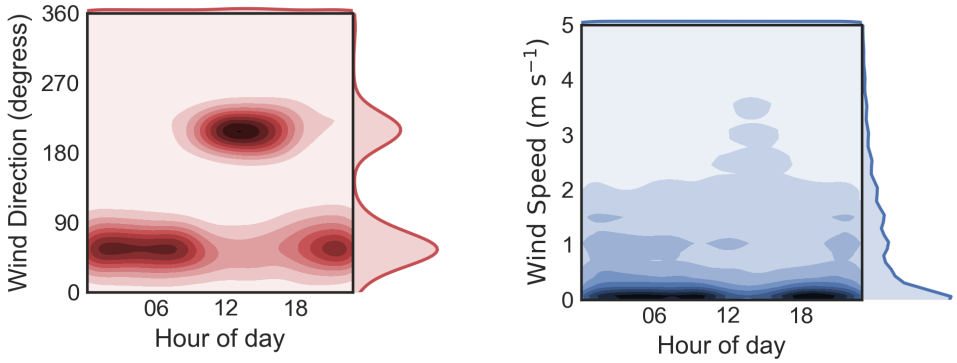

Goose Point

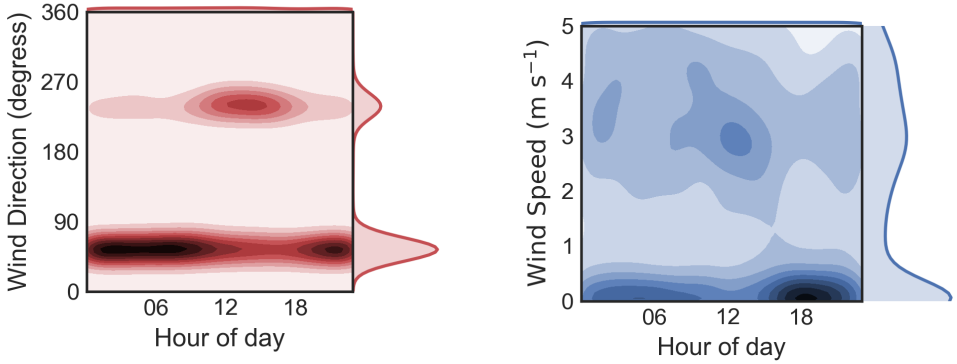

Dock Point

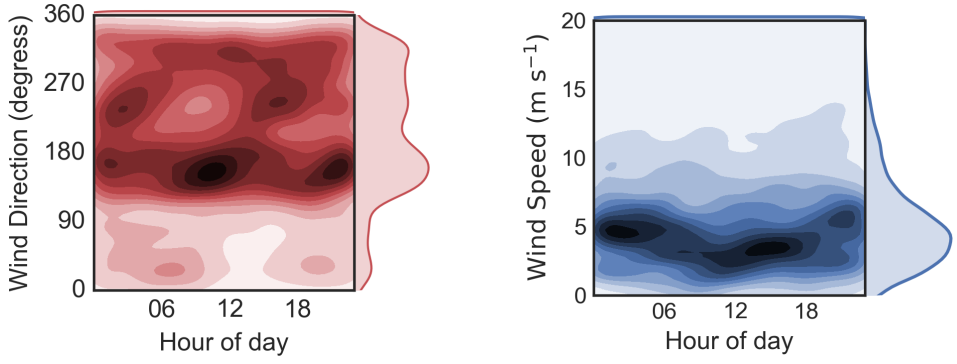

Browntop Mountain

Figure 5.3.7: Same as Fig. 5.3.6 for Goose Point , Dock Point, and Browntop Mountain

To characterize the relationships between the time-dependent wind speed and direction distributions (Figs. 5.3.6 and 5.3.7), spectral analyses, and the normalized wind speed profiles, I shall describe the inferred local circulations present at each site. The episodes of weak synoptic forcing as mentioned in Section 5.2 also contribute to this discussion:

Raft Creek

The high occurrence of light winds from the south-southwest (Fig. 5.3.1) appears to be a manifestation of a local-scale, nocturnal down-slope drainage wind, or katabatic wind. This persistent nighttime flow commences once daytime heating has ceased (Fig. 5.3.6), and the hills above the southern shoreline of the West Basin starts to cool due to longwave radiative loss. The drainage wind dies out once the basin begins to warm again after sunrise, and is replaced by along-channel flow from either the southeast or northwest. While daytime northwesterlies are more frequent than southeasterlies (Fig. 5.3.1), the direction of the daytime flow does not appear to be dependent on the wind speed; it is inferred from this that localized pressure field perturbations determine the direction of daytime winds in the absence of a stronger synoptic forcing. There is no thermally-induced up-slope wind (or anabatic wind) observed during the day at Raft Creek. Due to the timing of the katabatic wind corresponding with periods of reduced solar radiation at the site, it is difficult to discern the effects of thermal advection in the 15-minute temperature observations.

Plato Point

The nighttime regime at Plato Point is dominated by light winds form the south to south-east (Fig. 5.3.6). The angle of the terrain surrounding Plato Point is not as steep as in valleys such as the north or east arms. The variability of nighttime winds indicate they are a result of weak localized pressure differences caused by differential heating/cooling of dissimilar surfaces, rather than a gravity-induced flow. During the daytime, increases in the differential heating due to solar radiation strengthens these pressure gradients, however the

magnitude of daytime wind speeds appears to be irrespective of which direction the winds are from.

Long Creek

Data from Long Creek exhibit a similar pattern to the Raft Creek site, whereby the tri-directional windrose (Fig 5.3.1) displays the prominence of a nocturnal katabatic wind. In this instance, it represents air descending the east facing slopes above the western shoreline of the arm. The down-slope flow begins soon after sunset from the same process observed at Raft Creek, but persists longer into the morning than the winds observed in the West Basin (Fig, 5.3.6). The longer duration of the katabatic wind results in a shorter daytime window for along-channel flow that overruns the drainage winds. Despite this, the along-axis winds peak around the same time of day as detected at Raft Creek, from noon to early afternoon (Figs. 5.3.5 and 5.3.6). The direction of the daytime flow appears to be predominantly from the south, with the occasional northeasterly that blows down the North Arm. The same pattern exists in daytime winds at Goose Point, indicating the up-arm flow could be a component of a larger Mountain basin circulation that occurs due to daytime heating around the ridgetops at the head of the valley. The example period of 27 August 2018 to 3 September 2018 displays the coupling of the diurnal wind pattern and daily temperature trend when synoptic forcing is weak (Fig. 5.3.8).

Goose Point

A nighttime katabatic wind exists at Goose Point, although it is not as obvious from the wind direction distribution because the nocturnal flow is aligned with the channel axis (Fig. 5.3.1). Air draining down the south facing slopes that form the head of the North Arm result in a northeasterly flow across Goose Point. This wind consistently occurs at nighttime in the absence of any larger synoptic forcing and similar to the northeasterly flow at Long Creek, it persists into the morning well after sunrise (Fig. 5.3.7). Once

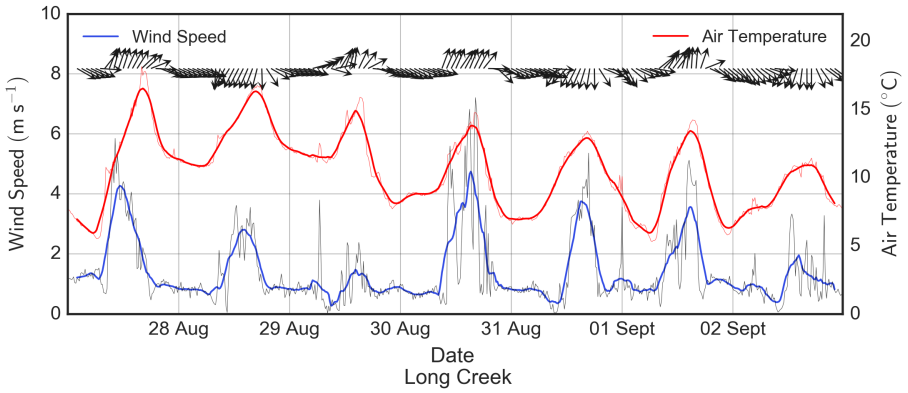

Figure 5.3.8: Wind and air temperature data recorded at Long Creek from 27 August 2018 to 3 September 2018. Light red and light grey traces represent 15-minute observations, while the bold blue and red lines are moving averages using a 4-hour window. Black arrows indicate the direction winds are blowing towards

daytime heating begins at the north end of the North Arm however, the flow reverses and a daytime thermally-induced anabatic wind is observed. This southerly flow is stronger than its nighttime counterpart, in agreement with Barry (2008), and also results in higher wind speeds than on days when the wind remains northeasterly. During the example period displayed in Fig. 5.3.9, the anabatic wind occurred on four out of the seven days, which is indicated by the daytime southwesterly flow being coupled with the mid-day peak in hourly wind speed. The combination of these alternating katabatic and anabatic winds creates a Mountain basin circulation as described by Whiteman (2000).

Dock Point

Dock Point observes a high occurrence of nighttime northeasterly winds (Fig. 5.3.7), indicating that a drainage wind extends out of the end of the East Arm due associated with longwave radiative cooling. Gravity-induced winds out of the Niagara Creek valley may also contribute to this outflow. A coherent diurnal signal is difficult to distinguish from the timeseries, yet can be partly inferred from the time-dependent distributions and the spectral analysis (Figs. 5.3.4 and 5.3.7). There is a pronounced minimum in wind speeds observed

around 1800 PDT (Fig. 5.3.5), which possibly indicates a change in the forcing regime between daytime and nighttime.

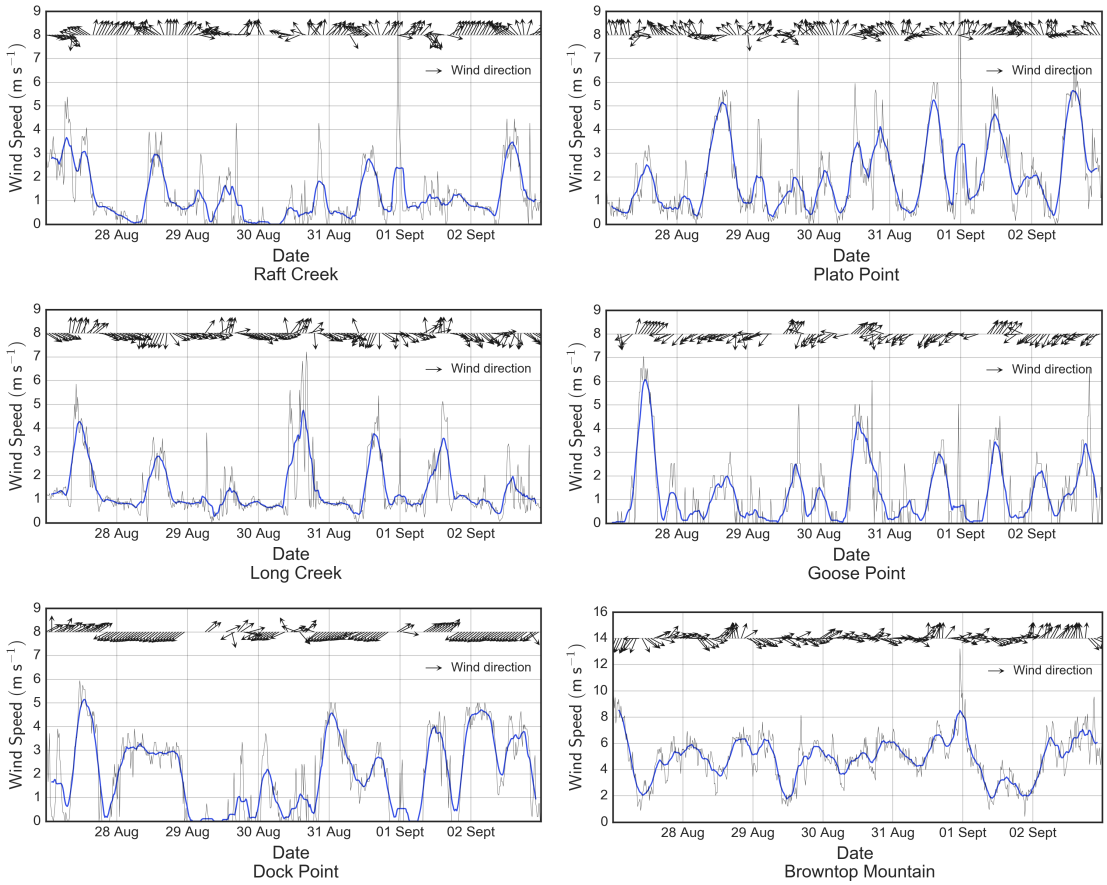

Figure 5.3.9: An example period of weak synoptic forcing when local circulations are present, from 27 August 2018 to 3 September 2018. The light grey trace is raw 15-minute data while the blue line represents a 4-hour moving average. Arrows represent the direction winds are blowing towards. Note the different scale used for Browntop Mountain due to the magnitude of peak wind speeds

5.3.4 Response to strong winds

Case study 1: The first episode of strong winds that will be investigated is a westerly event that resulted from the passage of a cold front during 12 and 13 September 2018. This particular event was identified by the timeseries filtering used in Section 4.2.2, but excluded from the analysis in Chapter 4 due to the episode length being 35 hours long - one hour short of the required duration. Since no episodes identified in Chapter 4 occurred while all five lake-level stations were operating, choosing this event as a case study was a straightforward decision.

The passing of the cold front is evident in temperature observations from the lake-level stations and from Browntop Mountain (not shown). Air temperature and relative humidity decrease sharply around 0900 PDT 12 September 2018 at Raft Creek, the first station the frontal system encounters in its west-east passage across the region. Similar temperature trends are observed at Dock Point 3 hours later (1200 PDT 12 September 2018), indicating that the front was moving at approximately 22 km hr^{-1} (6.1 m s^{-1}). Precipitation associated with the front is suspected to have caused icing on the anemometer at Browntop Mountain, resulting in the loss of wind data during this period (Fig. 5.3.11).

In the West Basin, Main Basin, and North Arm, wind speed steadily increases during and after the passage of the cold front, with peak wind speeds occurring approximately 6 hours after the front has passed. The response at Dock Point is more incremental, with a long build-up in intensity resulting in peak wind speeds occurring around 1400 PDT 13 September 2018. This peak in the East Arm corresponds to a second pulse of strong winds observed in the North Arm between 1200 and 1500 PDT 13 September 2018, likely a result of post-frontal convective activity.

Overall, throughout this strong wind event the wind-field can be described as a northwest-

erly flow down the West Basin that is then channelled as a southwesterly wind across the Main Basin. The flow diverges at the junction and traverses the lengths of the north and east arms. The differing wind directions are a result of forced channelling by the surrounding topography, although on some occasions the 800 hPa geopotential height gradient is aligned with one of the lake's sub-basins, which would induce pressure-driven channelling along that arm or basin. These observations are in agreement with wind data collected by Laval et al. (2008). The conceptual wind field derived from the lake-level surface observations (Fig. 5.3.10) is in agreement with the 800 hPa geopotential height gradient more so than the 925 hPa orientation. I suspect this is evidence of the ECMWF reanalysis model's inability to resolve the frontal system's interaction with the underlying topography at the 925 hPa level.

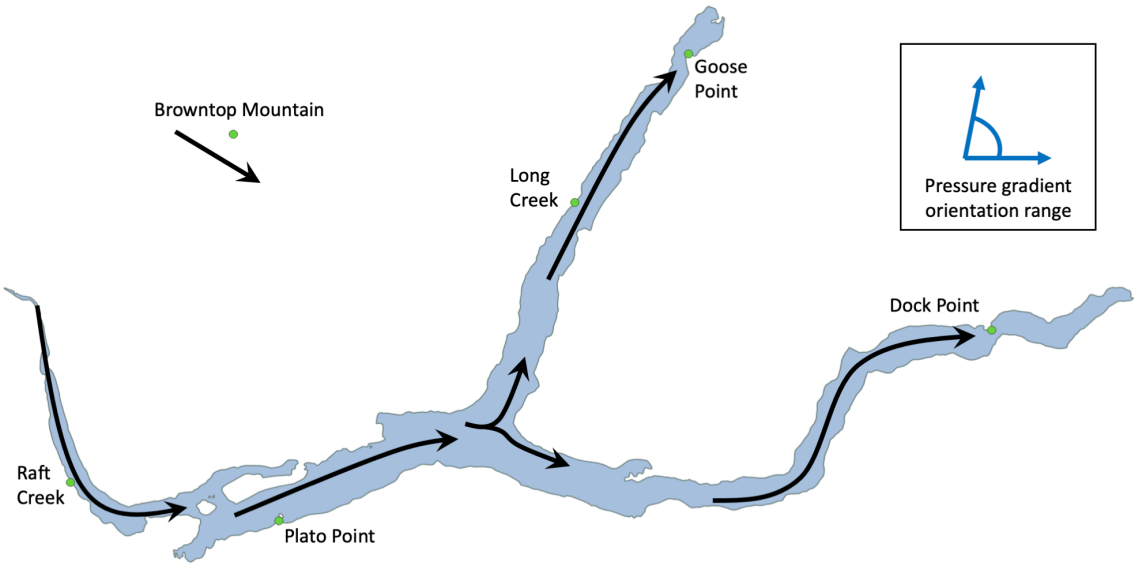

Figure 5.3.10: The conceptual wind field derived from 15-minute observations during the passage of a cold front over 12 and 13 September 2018. Black arrows denote the presumed channelized wind flow along each arm or basin of the lake. The range in orientation of the 800 hPa geopotential height gradient throughout the observation period is illustrated by the blue arrows in the upper-right corner of the figure

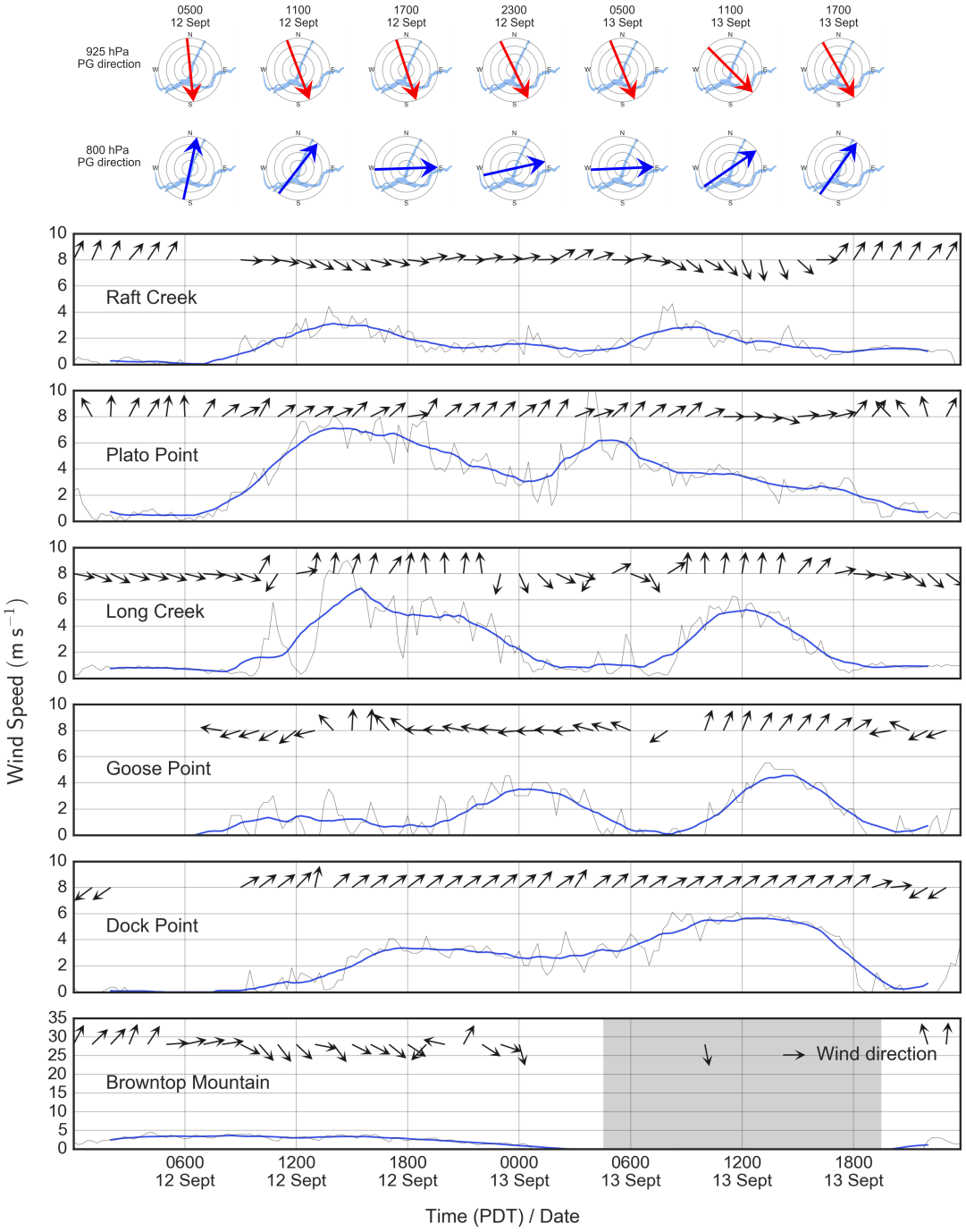

Figure 5.3.11: Top: Orientation of the 925 hPa (red) and 800 hPa (blue) geopotential height gradient across Quesnel Lake throughout a strong wind event during 12 and 13 September 2018. Bottom: The surface response to the wind event observed at six stations in the vicinity of Quesnel Lake. 15-minute wind speed data are shown by the grey trace, while the blue line represents the 4-hour moving average. Black arrows indicate the direction winds are blowing towards (hourly average). Grey shading on the Browntop Mountain panel represents the period of anemometer icing outlined in the text

Case study 2: The second event illustrates the wind regime during the passing of a warm front during 27 and 28 October 2018. The passage of the front at approximately 0000 PDT 28 October 2018 is evident in temperature data from all stations, but most acutely at Plato Point where an air temperature of 9.0°C was recorded at 0400 PDT 28 October 2018 (not shown). This particular event was chosen as it corresponds to the maximum wind speeds observed at Browntop Mountain during the 109 day analysis period. At Browntop Mountain, southeasterly winds steadily increase in intensity from 1200 PDT 27 October 2018 to a peak 15-minute wind speed of 29.3 m s^{-1} (over 105 km hr^{-1}), recorded at 0215 PDT 28 October 2018. Winds then diminish over the following 6 to 8 hours (Fig. 5.3.13).

Pressure-driven channelling of the wind field along the east-west axis of Quesnel Lake is evident for the East Arm and Main Basin throughout this southeasterly/easterly event. Dock Point and Plato Point experience increasing wind speeds that begin at 0900 PDT 27 October 2018, following a similar pattern to the Browntop Mountain observations. Both lake-level stations then have another local maximum in the four-hour moving average observed during the following day (28 October 2018). This is in contrast to Browntop Mountain where winds have subsided by this time. The discrepancy in timing could be related to the passing of the front, yet evidence in the temperature and relative humidity data was not sufficient to draw any conclusions about the speed and movement of the system.

Unfortunately, the Raft Creek station was not operating over this period therefore the wind conditions in the West Basin are unknown. The response in the North Arm appears muted due to the orientation of the geopotential height gradient compared to the arm axis. The pressure gradient being perpendicular to the channel results in minimal forcing along the length of the North Arm. Additionally, a statically-stable near-surface layer appears to be trapped in the channel until the front has passed. Air temperature observations at 0200 PDT

28 October 2018 of 3°C at Goose point (728 masl), and -3°C at Browntop Mountain (2031 masl) result in an environmental lapse rate of 4.6°C km^{-1}. This stability in the ABL could have inhibited the downwards flux of momentum from the above-ridgetop wind field, and remains in place until after the passage of the front when winds at Browntop Mountain abate. For reference, the air temperature at Plato Point (728 masl) at 0200 PDT 28 October 2018 was 8.5°C, representing an environmental lapse rate of 8.8°C.

The orientation of the 925 and 800 hPa geopotential height gradients are in better agreement with each other than during the cold front/westerly event of case #1. Both levels appear to accurately represent the pressure gradient forcing for the observed winds that have then contributed to the development of the conceptual wind field in Fig. 5.3.12.

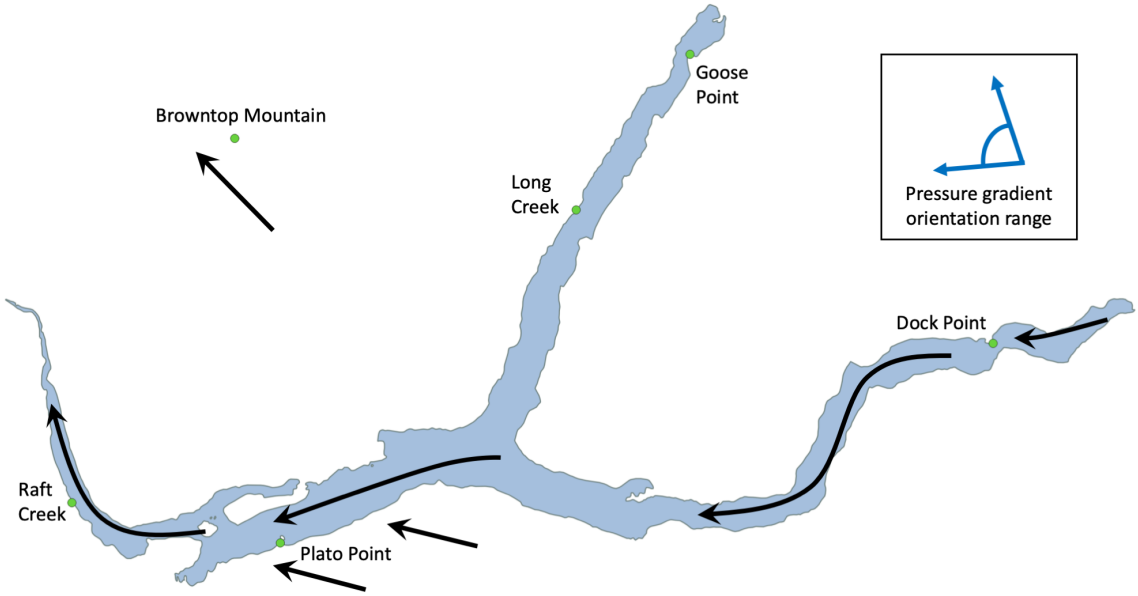

Figure 5.3.12: The conceptual wind field derived from 15-minute observations throughout the passage of a warm front during 27 and 28 October 2018. Black arrows denote the presumed channelized wind flow along each arm or basin of the lake. The range in orientation of the 800 hPa geopotential height gradient throughout the observation period is illustrated by blue arrows in the upper-right corner of the figure

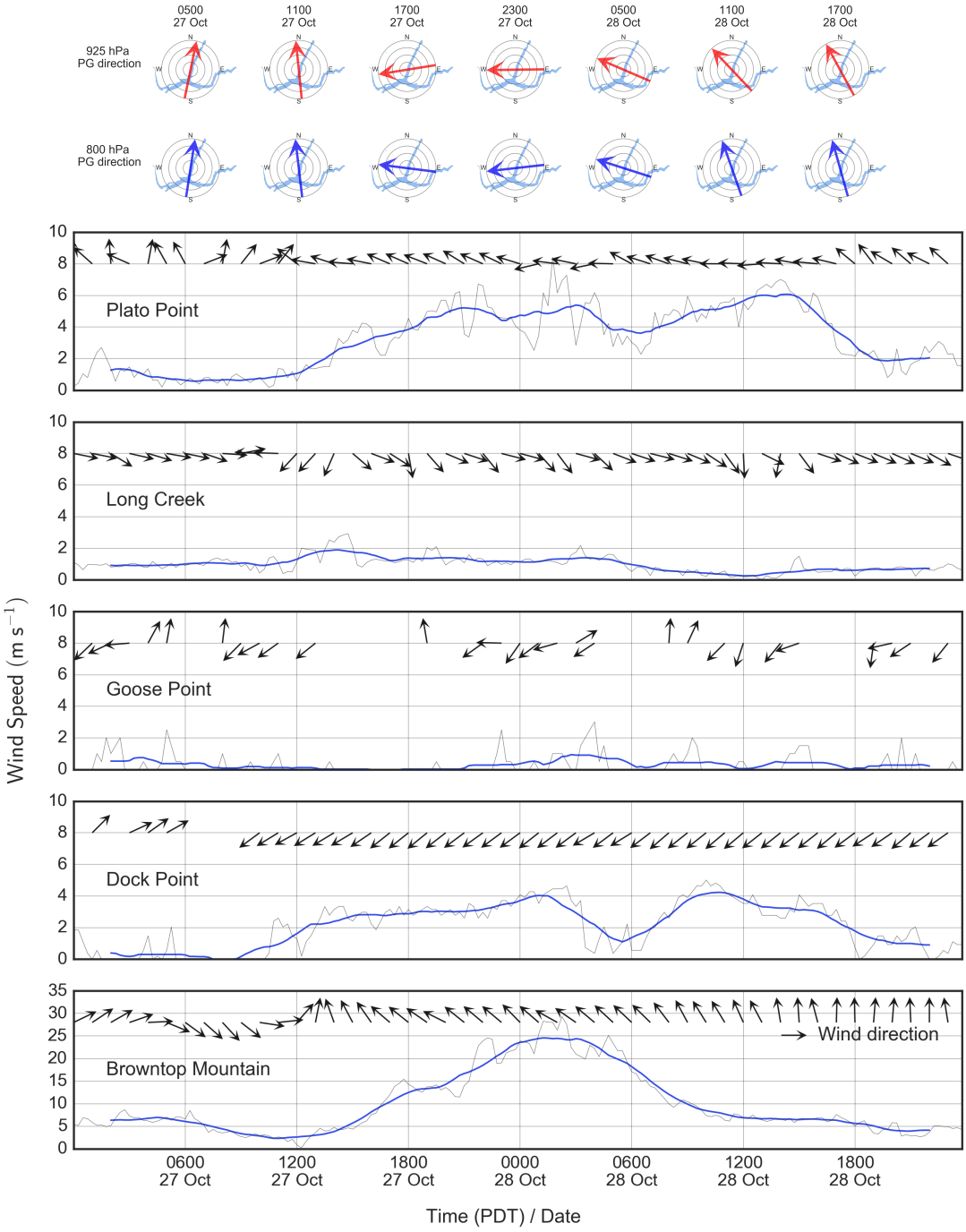

Figure 5.3.13: Top: Orientation of the 925 hPa (red) and 800 hPa (blue) geopotential height gradient across Quesnel Lake throughout a strong wind event during 27 and 28 October 2018. Bottom: The surface response to the wind event observed at six stations in the vicinity of Quesnel Lake. 15-minute wind speed data are shown by the grey trace, while the blue line represents the 4-hour moving average. Black arrows indicate the direction winds are blowing towards (hourly average)

5.4 Discussion

Data collected simultaneously from six meteorological stations in the vicinity of Quesnel Lake have provided valuable information regarding the spatial and temporal variability of winds across the lake basin. This variability is controlled by a combination of topographic channelling, radiative effects, localized circulations, and regional pressure gradients.

In the absence of large-scale synoptic forcing, local thermally-induced circulations affect many areas of the lake. The intensity of these small-scale flows is dependent on the time of day that they occur. Weak, down-slope, gravity induced winds are observed at nighttime when the forested slopes of the elongated valleys experience longwave radiative cooling. Stronger daytime circulations are dependent on the orientation of the sub-basin of the lake and the amount of solar radiative forcing present. This is evident in the North Arm when a reversible diurnal Mountain basin circulation has been observed when conditions are appropriate and are in agreement with previous research and current theoretical models. Without a discernible large-scale forcing winds in each sub-basin of the lake appear to respond to local pressure perturbations independently, however, this could be a result of the low spatial resolution of the available data and definitive conclusions about the synchronization across the entire wind field will require a more substantive dataset.

The interaction of synoptic-scale systems with the mountainous topography that surrounds Quesnel Lake creates wind-field orientations that are contingent on the direction of the regional pressure gradient field. A coherent lake-wide response is most likely when the lake is exposed to a large-scale west-to-east pressure gradient, whereby the orientation of each arm of the lake is favourable to channelling wind with a westerly component. When the region is under the influence of an east-to-west pressure gradient lake-level winds are observed to be substantially different in both intensity and direction from the above-

ridgetop flow.

Uncertainties in the initial analysis of wind variability coupled with the periods of inoperable equipment highlight the importance of continued data collection, and justify the expansion of the CAMnet instrumentation array if operational circumstances allow.

6 Conclusions

6.1 Summary

Using three discrete temporal and spatial scales, this study represents a compilation of wind conditions at Quesnel Lake, British Columbia. Beginning with a 25-year period of monthly ECCC data, Chapter 3 outlines the wind seasons that can be expected throughout the year by identifying periods above and below the mean annual wind speed. A peak in mean monthly wind speeds in March and again in November indicate the midpoints for the fall (October to December) and winter/spring (January to May) storm periods, and separates them from the calm summer months of June to September.

Chapter 4 presents the synoptic influence on the wind seasonality by examining strong wind events observed at Quesnel Lake. With the motivation of providing further background for limnologists investigating wind-forced seiche modes in the lake, episodes of strong wind stress that persisted for a prescribed duration were identified and tabulated. The active seasons of fall and winter/spring experience the majority of strong wind events, with the wind direction most likely to be easterly. The summer calm season occasionally observes wind storms that can be either easterly or westerly in nature, with a minimum in both mean monthly wind speeds and storm occurrences, during August. It was found that despite the seasonality of strong wind episodes, there is no statistically significant difference between either the duration, or the total wind stress imparted to the lake across all three seasons.

Chapter 4 also focuses on an environment-to-climate synoptic climatology using the strong wind episodes to represent the surface response to a given synoptic configuration. From this climatology, a method for projecting a limited number of synoptic states using a self organising map (SOM) has been proposed. The resulting SOM nodes can be tagged with

a variety of parameters to allow the practitioner to evaluate the success of the procedure. In this case the SOM was tested in its ability to classify the synoptic patterns associated with the strong wind events by either (i) the mean wind direction during the episode, or (ii) the season the event occurred in. Results were analogous to the manual classification that delineated synoptic patterns based on whether the winds at lake-level were easterly or westerly driven.

In Chapter 5, an initial investigation into the spatial and temporal variability of the wind field across Quesnel Lake was performed using 109 days of 15-minute observations from six stations in the vicinity of the lake. Diurnal signals in wind speed datasets were present, and identified by their peaks in the power spectra density. Two locations in particular experience nocturnal katabatic flows that descend the slopes that border each station. These light yet persistent winds are overrun during the daytime by stronger along-channel flow.

Also in Chapter 5, two case studies investigated the basin-scale response to the passage of larger synoptic-scale systems. Strong westerly winds associated with the passing of a cold front in September occurred during and after the front had moved across the region. This is in contrast to the easterly winds associated with a warm front later in October that precede the front and continue until it has passed, at which point wind intensity diminishes. Noticeably, the orientation of Quesnel Lake's sub-basins, especially the North Arm, allow the forced channelling of westerly winds to excite all reaches of the lake. Whereas, the easterly case study provided an ideal example of the synoptic pressure gradient field being perpendicular to the North Arm. Combined with a statically stable ABL, the lack of an along-axis pressure gradient resulted in calm conditions in the North Arm while Browntop Mountain experiences wind speeds in excess of 105 km hr^{-1}. I describe this spatial and temporal variability analysis as a first attempt because the current array of stations used for this chapter has yet to collect data throughout an entire calendar year. Therefore, more

detailed conclusions regarding the variability may be proposed in the future as data become available.

The first research objective outlined in Section 1.2 of this thesis is achieved by combining the results of Chapters 3 and 5, whereby wind conditions in each region of the lake may be estimated by considering the wind seasonality and, if synoptic forcing is weak, the time of day. If synoptic-scale pressure gradients over Quesnel Lake intensify, then the orientation of the pressure gradient over the domain of the lake will become the dominant factor dictating the lake-level response. This is particularly evident when the wind field of the North Arm appears to be de-coupled from the synoptic flow in the presence of an east-west pressure gradient. It is also an important observation when considering the conclusions of Brenner (2017) who identified the potential for various seiche modes to be activated by a spatially variable wind field. While the conceptual wind field derived from strong southwesterly winds agrees with results from Laval et al. (2008), I am also able to conclude that this wind pattern is less likely than its easterly/southeasterly driven counterpart. With this in mind, the occurrence of an east-west seiche set-up should be carefully considered in future limnological research.

The spectrum of synoptic-scale atmospheric patterns that lead to strong wind events at Quesnel Lake is displayed using a SOM, fulfilling the second objective of Section 1.2. While it is not a probabilistic determination of what will excite seiche modes in the lake, the clustering of these strong wind events in spring and fall does coincide with seasonal overturning and observed sediment resuspension in the West Basin. The quantification of the total wind stress during these events may provide a tool for comparing one forcing episode to another.

The broader ecological investigations into the impacts of the Mount Polley mine spill require a robust understanding of the physical processes that affect the chemical and biolog-

ical systems of Quesnel Lake. With wind forcing responsible for the movement of surface water and the transfer of energy from the ABL to the water column, this thesis provides insight into one of these physical drivers. The timing and intensity of strong wind episodes can now be viewed in the context of how these episodes relate to seiche activity, and to other ecological processes such as the salmon run, or algae blooms. While this thesis does not approach the topic of the long-term effects from the Mount Polley mine spill, it will contribute to our understanding of the physical mechanisms that may lead to sediment resuspension and the mixing of mine tailings in the water column.

6.2 Future work

While this study provides an outline of the general wind climate, seasons, and coarsely-resolved wind field observed at Quesnel Lake, there are aspects that require further investigation to be of maximum benefit to audiences outside of the meteorological community.

6.2.1 Synoptic climatology

The synoptic climatology presented was based upon an assumption that strong wind events observed in the Main Basin of Quesnel Lake, that persist for 36 hours or more, may excite a basin-scale hydrodynamic response in the lake. To refine this further, the coupling of water column temperature data with the associated near-surface wind forcing as outlined by Brenner (2017), and illustrated by Laval et al. (2008), would enhance the conclusions derived from such a study. That is, the exact date and times of seiche action could replace the timing of peak wind stress used in Section 4.2.2. To date, no published literature has used the environment-to-climate method to describe the synoptic forcing for wind induced seiche activity. The SOM method outlined in Section 4.3.3 would provide the visualization tool for displaying the large-scale atmospheric patterns. It is understood however,

the geometry of Quesnel Lake introduces a multitude of complexities to understanding the forced response, and that resolving the uncertainties in the hydrodynamic processes will be the priority for limnologists for the immediate future.

6.2.2 Modelling

The current array of five lake-level stations, coupled with the neighbouring sites of other CAMnet installations, means that Quesnel Lake is quite possibly one of the more intensely monitored bodies of water in British Columbia, from a meteorological viewpoint. Despite this, the complex topography of the Cariboo Mountains, and multiple intersecting basins of the lake will result in a relatively coarse understanding of the near-surface wind field, regardless of the amount of data collected. Recent work by Valerio et al. (2017) used the Weather Research and Forecasting (WRF) model to evaluate the wind field over a similarly complex pre-alpine lake. In conjunction with this modelling approach could be the employment of remote-sensing tools to estimate parameters such the sheltering effect of the surrounding landforms, and the roughness length of the underlying surface (Rueda et al., 2009; Van Den Hoek et al., 2015).

Regardless of the direction of future investigations, the continued technical and logistical support to maintain the lake-level stations will be of vital importance. Whether it be a derivation of the near-surface wind field from observations, or the validation of numerical modelling attempts, data obtained from shore-based locations will undoubtedly play a role in further research. From a technical point-of-view, the connection of the furthest stations (i.e., Long Creek, Goose Point, Dock Point) to a satellite or cellular network would reduce the time and expenditure of visiting the sites to manually download the data. This would also improve safety for field staff and reduce the project's carbon footprint by decreasing the amount of fuel required to access the stations. It is recommend by the author

that the current array be maintained, and the value to the project be ultimately determined by its ability to validate future modelling efforts. The locations currently used for site installations are the few that could be found after extended reconnaissance of the shoreline. Increasing the spatial density of the lake-level network is unlikely, unless the use of moored instruments is employed in the future.

7 Appendices

7.1 Appendix A

Table of strong wind episodes identified using the methods outlined in section 4.2.2.

Table 13: Filtered episode data

Index	Start date/time (PDT)	End date/time (PDT)	Duration (hours)	Mean wind direction (degrees)	Wind steadiness (S)	Mean wind stress (m^2 s^{-2})	Total wind stress (m^2 s^{-2})
1	2016-10-08 10:00:00	2016-10-09 23:00:00	37	235.2	0.80	21.5	818.6
2	2016-10-12 12:00:00	2016-10-14 14:00:00	50	109.4	0.90	24.4	1243.5
3	2016-10-14 19:00:00	2016-10-16 18:00:00	47	121.1	0.79	20.2	970.7
4	2016-10-19 08:00:00	2016-10-21 10:00:00	50	109.7	0.84	21.8	1109.6
5	2016-10-22 21:00:00	2016-10-25 07:00:00	58	107.6	0.88	16.8	993.1
6	2016-11-01 18:00:00	2016-11-03 08:00:00	38	114.7	0.79	16.6	647.3
7	2016-11-06 22:00:00	2016-11-08 23:00:00	49	105.3	0.79	20.0	1000.9
8	2016-11-10 22:00:00	2016-11-12 10:00:00	36	101.7	0.82	16.6	613.5
9	2016-11-18 23:00:00	2016-11-21 02:00:00	51	113.4	0.88	17.5	908.8
10	2016-11-22 08:00:00	2016-11-25 00:00:00	64	111.4	0.83	16.8	1090.2
11	2016-12-17 23:00:00	2016-12-19 19:00:00	44	122.7	0.84	27.6	1244.0

Index	Start date/time (PDT)	End date/time (PDT)	Duration (hours)	Mean wind direction (degrees)	Wind steadiness (S)	Mean wind stress (m^2 s^{-2})	Total wind stress (m^2 s^{-2})
12	2016-12-25 22:00:00	2016-12-27 12:00:00	38	117.2	0.91	25.7	1002.2
13	2016-12-28 22:00:00	2016-12-30 19:00:00	45	160.1	0.85	18.9	869.9
14	2017-01-15 19:00:00	2017-01-18 19:00:00	72	103.4	0.86	30.2	2204.3
15	2017-01-27 03:00:00	2017-01-30 13:00:00	82	117.0	0.86	25.4	2110.6
16	2017-02-14 09:00:00	2017-02-15 23:00:00	38	95.4	0.83	15.9	621.8
17	2017-03-01 10:00:00	2017-03-03 09:00:00	47	114.1	0.76	26.6	1277.8
18	2017-03-07 03:00:00	2017-03-09 01:00:00	46	162.6	0.78	18.5	867.3
19	2017-03-12 04:00:00	2017-03-15 01:00:00	69	98.9	0.82	15.8	1106.0
20	2017-03-17 04:00:00	2017-03-19 10:00:00	54	120.3	0.79	21.5	1180.8
21	2017-03-29 15:00:00	2017-03-31 06:00:00	39	207.7	0.80	19.7	786.3
22	2017-04-03 21:00:00	2017-04-05 18:00:00	45	98.6	0.85	19.7	907.1
23	2017-04-26 17:00:00	2017-04-28 10:00:00	41	248.6	0.76	19.2	805.9

Index	Start date/time (PDT)	End date/time (PDT)	Duration (hours)	Mean wind direction (degrees)	Wind steadiness (S)	Mean wind stress (m^2 s^{-2})	Total wind stress (m^2 s^{-2})
24	2017-05-02 12:00:00	2017-05-06 02:00:00	86	94.4	0.84	17.8	1545.0
25	2017-05-23 01:00:00	2017-05-24 20:00:00	43	219.2	0.74	22.4	984.3
26	2017-06-14 16:00:00	2017-06-16 07:00:00	39	111.6	0.85	16.8	670.0
27	2017-06-26 06:00:00	2017-06-29 00:00:00	66	235.7	0.83	15.5	1037.7
28	2017-09-30 14:00:00	2017-10-02 06:00:00	40	233.0	0.80	20.8	851.8
29	2017-10-16 16:00:00	2017-10-19 09:00:00	65	137.2	0.76	23.8	1570.4
30	2017-10-23 06:00:00	2017-10-26 04:00:00	70	123.8	0.84	22.2	1574.6
31	2017-10-31 14:00:00	2017-11-03 03:00:00	61	162.2	0.73	22.2	1377.8
32	2017-11-11 09:00:00	2017-11-13 06:00:00	45	107.8	0.85	19.4	892.7
33	2017-11-13 20:00:00	2017-11-16 02:00:00	54	113.8	0.81	25.2	1383.3
34	2017-11-17 20:00:00	2017-11-19 13:00:00	41	112.4	0.86	23.7	994.8
35	2018-01-20 00:00:00	2018-01-22 02:00:00	50	106.8	0.83	24.5	1250.6

Index	Start date/time (PDT)	End date/time (PDT)	Duration (hours)	Mean wind direction (degrees)	Wind steadiness (S)	Mean wind stress (m^2 s^{-2})	Total wind stress (m^2 s^{-2})
36	2018-01-27 21:00:00	2018-01-29 18:00:00	45	119.4	0.86	25.5	1173.1
37	2018-02-01 11:00:00	2018-02-04 02:00:00	63	132.3	0.83	17.8	1139.7
38	2018-02-07 05:00:00	2018-02-09 09:00:00	52	176.5	0.85	22.9	1211.9
39	2018-02-13 17:00:00	2018-02-15 16:00:00	47	224.5	0.78	21.4	1027.9
40	2018-02-15 21:00:00	2018-02-17 09:00:00	36	158.8	0.84	18.0	667.1
41	2018-02-28 03:00:00	2018-03-02 05:00:00	50	105.3	0.82	20.2	1028.7
42	2018-03-08 10:00:00	2018-03-10 01:00:00	39	130.5	0.87	22.4	895.0
43	2018-03-21 13:00:00	2018-03-23 05:00:00	40	100.2	0.83	21.5	883.2
44	2018-03-29 17:00:00	2018-03-31 10:00:00	41	211.9	0.83	36.3	1525.0
45	2018-04-12 21:00:00	2018-04-14 10:00:00	37	117.0	0.74	18.5	702.1
46	2018-06-09 06:00:00	2018-06-11 15:00:00	57	255.9	0.82	23.7	1374.9
47	2018-07-01 14:00:00	2018-07-03 03:00:00	37	221.7	0.74	21.0	796.6

References

Abraham, E. R. (1997). Seiche modes of Wellington Harbour, New Zealand. *New Zealand Journal of Marine and Freshwater Research*, 31(2):191–200.

Agrawal, Y. C., Terray, E. A., Donelan, M. A., Hwang, P. A., Williams, A. J., Drennan, W. M., Kahma, K. K., and Krtaigorodskii, S. A. (1992). Enhanced dissipation of kinetic energy beneath surface waves. *Nature*, 359(6392):219–220.

Andrew, F. J. and Geen, G. H. (1960). *Sockeye and Pink Salmon Production in Relation to Proposed Dams in the Fraser River System*. International Pacific Salmon Fisheries Commission, New Westminster, 266pp.

Antenucci, J. P. and Imberger, J. (2003). The seasonal evolution of wind/internal wave resonance in Lake Kinneret. *Limnology and Oceanography*, 48(5):2055–2061.

Bakri, T., Jackson, P., and Doherty, F. (2017a). A synoptic climatology of strong along-channel winds on the Coast of British Columbia, Canada. *International Journal of Climatology*, 37(5):2398–2412.

Bakri, T., Jackson, P., and Doherty, F. (2017b). Along-channel winds in Howe Sound: climatological analysis and case studies. *Atmosphere - Ocean*, 55(1):12–30.

Banner, M. L. and Peirson, W. L. (1998). Tangential stress beneath wind-driven air–water interfaces. *Journal of Fluid Mechanics*, 364:115–145.

Barry, R. G. (2008). *Mountain Weather and Climate*. Cambridge University Press, Cambridge, 493pp.

Beedle, M. J., Menounos, B., Luckman, B. H., and Wheate, R. (2009). Annual push moraines as climate proxy. *Geophysical Research Letters*, 36(20):2–6.

Beedle, M. J., Menounos, B., and Wheate, R. (2015). Glacier change in the Cariboo Mountains, British Columbia, Canada (1952-2005). *Cryosphere*, 9(1):65–80.

Berrisford, P., Dee, D., Poli, P., Brugge, R., Fielding, K., Fuentes, M., Kallberg, P., Kobayashi, S., Uppala, S., and Simmons, A. (2009). The ERA-Interim Archive Version 2.0. Technical report.

Breckling, J., editor (1989). *The Analysis of Directional Time Series: Applications to Wind Speed and Direction*, volume 61 of *Lecture Notes in Statistics*. Springer New York, New York, NY.

Brenner, S. (2017). *The free oscillatory response of fjord-type multi-armed lakes*. Masters thesis, University of British Columbia, 86pp.

Brewer, M. C., Mass, C. F., and Potter, B. E. (2012). The West Coast thermal trough: climatology and synoptic evolution. *Monthly Weather Review*, 140(12):3820–3843.

Bryant, K. and Akbar, M. (2016). An exploration of wind stress calculation techniques in hurricane storm surge modeling. *Journal of Marine Science and Engineering*, 4(3):58.

Burford, J. E., Déry, S. J., and Holmes, R. D. (2009). Some aspects of the hydroclimatology of the Quesnel River Basin, British Columbia, Canada. *Hydrological Processes*, 23:1529–1536.

Burt, S. (2012). *The Weather Observer's Handbook*. Cambridge University Press, Cambridge, 444pp.

Campbell Scientific (2017). Campbell Scientific: Wind monitor 05103-10 description. (Retrived from https://www.campbellsci.ca/05103-10).

Carrera, M. L., Gyakum, J. R., and Lin, C. A. (2009). Observational study of wind chan-

neling within the St. Lawrence River Valley. *Journal of Applied Meteorology and Climatology*, 48(11):2341–2361.

Castillo, M. I., Pizarro, O., Ramírez, N., and Cáceres, M. (2017). Seiche excitation in a highly stratified fjord of southern Chile: The Reloncaví fjord. *Ocean Science*, 13(1):145–160.

Chenoli, S. N., Turner, J., and Samah, A. A. (2013). A climatology of strong wind events at McMurdo station, Antarctica. *International Journal of Climatology*, 33(12):2667–2681.

Cremades, L. V., Santaba, J. M., and Marti, M. (1999). Analysis and modelling of time series of surface wind speed and direction. *International Journal of Climatology*, 209:197–209.

de Jong, M. P. C. and Battjes, J. A. (2004). Seiche characteristics of Rotterdam Harbour. *Coastal Engineering*, 51(5-6):373–386.

Dee, D. P., Uppala, S. M., Simmons, A. J., Berrisford, P., Poli, P., Kobayashi, S., Andrae, U., Balmaseda, M. A., Balsamo, G., Bauer, P., Bechtold, P., Beljaars, A. C., van de Berg, L., Bidlot, J., Bormann, N., Delsol, C., Dragani, R., Fuentes, M., Geer, A. J., Haimberger, L., Healy, S. B., Hersbach, H., Hólm, E. V., Isaksen, L., Kållberg, P., Köhler, M., Matricardi, M., Mcnally, A. P., Monge-Sanz, B. M., Morcrette, J. J., Park, B. K., Peubey, C., de Rosnay, P., Tavolato, C., Thépaut, J. N., and Vitart, F. (2011). The ERA-Interim reanalysis: Configuration and performance of the data assimilation system. *Quarterly Journal of the Royal Meteorological Society*, 137(656):553–597.

Delacre, M., Lakens, D., and Leys, C. (2017). Why psychologists should by default use Welch's t-test instead of Student's t-test. *International Review of Social Psychology*, 30(1):92–101.

Déry, S. J., Clifton, A., MacLeod, S., and Beedle, M. J. (2010). Blowing snow fluxes in the Cariboo Mountains of British Columbia, Canada. *Arctic, Antarctic, and Alpine Research*, 42(2):188–197.

Déry, S. J., Stadnyk, T. A., MacDonald, M. K., Koenig, K. A., and Guay, C. (2018). Flow alteration impacts on Hudson Bay river discharge. *Hydrological Processes*, 32(24):3576–3587.

Donelan, M. A., Haus, B. K., Reul, N., Plant, W. J., Stiassnie, M., Graber, H. C., Brown, O. B., and Saltzman, E. S. (2004). On the limiting aerodynamic roughness of the ocean in very strong winds. *Geophysical Research Letters*, 31(18):L18306.

Eckman, R. M. (1998). Observations and numerical simulations of winds within a broad forested valley. *Journal of Applied Meteorology*, 37(2):206–219.

Edwards, R. Y. (1954). Fire and the decline of a mountain caribou herd. *The Journal of Wildlife Management*, 18(4):521–526.

Falconer, R. A., George, D. G., and Hall, P. (1991). Three dimensional numerical modelling of wind-driven circulation in a shallow homogeneous lake. *Journal of Hydrology*, 124:59–79.

Farmer, D. M. (1978). Observations of long nonlinear internal waves in a lake. *Journal of Physical Oceanography*, 8(1):63–73.

Findikakis, A. and Law, A. (1999). Wind mixing in temperature simulations for lakes and reservoirs. *Journal of Environmental Engineering*, 125(5):420–428.

Garcia, A., Torres, J. L., Prieto, E., and De Francisco, A. (1998). Fitting wind speed distributions: A case study. *Solar Energy*, 62(2):139–144.

Gardner, J. T., English, M. C., and Prowse, T. D. (2006). Wind-forced seiche events on

Great Slave Lake: Hydrologic implications for the Slave River Delta, NWT, Canada. *Hydrological Processes*, 20(19):4051–4072.

Garratt, J. R. (1992). *The Atmospheric Boundary Layer*. Cambridge University Press, Cambridge, 316pp.

Government of Canada (2017). Historical climate data, Environment and Climate Change Canada. (Retrieved from http://climate.weather.gc.ca/).

Greene, S., Morrissey, M., and Johnson, S. E. (2010). Wind climatology, climate change, and wind energy. *Geography Compass*, 4(11):1592–1605.

Gryning, S. E., Floors, R., Peña, A., Batchvarova, E., and Brümmer, B. (2016). Weibull wind-speed distribution parameters derived from a combination of wind-lidar and tall-mast measurements over land, coastal and marine sites. *Boundary-Layer Meteorology*, 159(2):329–348.

Hanley, K. E., Belcher, S. E., and Sullivan, P. P. (2010). A global climatology of wind–wave interaction. *Journal of Physical Oceanography*, 40(6):1263–1282.

Hellerman, S. and Rosenstein, M. (1983). Normal monthly wind stress over the world ocean with error estimates. *Journal of Physical Oceanography*, 13(7):1093–1104.

Hernández-Henríquez, M. A., Sharma, A. R., Taylor, M., Thompson, H. D., and Déry, S. J. (2018). The Cariboo Alpine Mesonet: sub-hourly hydrometeorological observations of British Columbia's Cariboo Mountains and surrounding area since 2006. *Earth System Science Data*, 10(3):1655–1672.

Hewitson, B. C. and Crane, R. G. (2002). Self-Organizing Maps : Applications to synoptic climatology. *Climate Research*, 22:13–26.

Hodges, B. R., Imberger, J., Laval, B., and Appt, J. (2000). Modeling the Hydrodynamics of Stratified Lakes. *Hydroinformatics 2000 Conference*, (July):23–27.

Hofherr, T. and Kunz, M. (2010). Extreme wind climatology of winter storms in Germany. *Climate Research*, 41(2):105–123.

Horn, W., Mortimer, C. H., and Schwab, D. J. (1986). Wind-induced internal seiches in Lake Zurich observed and modeled. *Limnology and Oceanography*, 31(6):1232–1254.

Imam, Y. E., Laval, B., Pieters, R., and Lawrence, G. (2013). The strongly damped baroclinic response to wind in a multibasin reservoir. *Limnology and Oceanography*, 58(4):1243–1258.

Jimenez, P. A. and Dudhia, J. (2013). On the ability of the WRF model to reproduce the surface wind direction over complex terrain. *Journal of Applied Meteorology and Climatology*, 52(7):1610–1617.

Jordi, A., Basterretxea, G., Casas, B., Anglès, S., and Garcés, E. (2008). Seiche-forced resuspension events in a Mediterranean harbour. *Continental Shelf Research*, 28(4-5):505–515.

Józsa, J. (2014). On the internal boundary layer related wind stress curl and its role in generating shallow lake circulations. *Journal of Hydrology and Hydromechanics*, 62(1):16–23.

Klink, K. (1999). Climatological mean and interannual variance of United States surface wind speed, direction and velocity. *International Journal of Climatology*, 19(5):471–488.

Klink, K. (2002). Trends and interannual variability of wind speed distributions in Minnesota. *Journal of Climate*, 15(22):3311–3317.

Kuo, Y.-H., Gyakum, J. R., and Guo, Z. (1995). A case of rapid continental mesoscale cyclogenesis. *Monthly Weather Review*, 123:970–997.

Lavagnini, A., Sempreviva, A. M., Transerici, C., Accadia, C., Casaioli, M., Mariani, S., and Speranza, A. (2006). Offshore wind climatology over the mediterranean Basin. *Wind Energy*, 9(3):251–266.

Laval, B., Imberger, J., Hodges, B. R., and Stocker, R. (2003). Modeling circulation in lakes: spatial and temporal variations. *Limnology and Oceanography*, 48(3):983–994.

Laval, B. E., Morrison, J., Potts, D. J., Carmack, E. C., Vagle, S., James, C., McLaughlin, F. A., and Foreman, M. (2008). Wind-driven summertime upwelling in a fjord-type lake and its impact on downstream river conditions: Quesnel Lake and River, British Columbia, Canada. *Journal of Great Lakes Research*, 34(1):189–203.

Laval, B. E., Vagle, S., Potts, D., Morrison, J., Sentlinger, G., James, C., McLaughlin, F., and Carmack, E. C. (2012). The joint effects of riverine, thermal, and wind forcing on a temperate fjord lake: Quesnel Lake, Canada. *Journal of Great Lakes Research*, 38(3):540–549.

Leggat, M. S., Owens, P. N., Stott, T. A., Forrester, B. J., Déry, S. J., and Menounos, B. (2015). Hydro-meteorological drivers and sources of suspended sediment flux in the pro-glacial zone of the retreating Castle Creek Glacier, Cariboo Mountains, British Columbia, Canada. *Earth Surface Processes and Landforms*, 40(11):1542–1559.

LeHau, H. H. (1959). Wind profile, surface stress and geostrophic drag coefficients in the atmospheric surface layer. *Advances in Geophysics*, 6(C):241–257.

Loikith, P. C., Lintner, B. R., and Sweeny, A. (2017). Characterizing large-scale meteo-

rological patterns and associated temperature and precipitation extremes over the northwestern United States using self-organizing maps. *Journal of Climate*, 30:2829–2847.

Lun, I. Y. F. and Lam, J. C. (2000). A study of Weibull parameters using long-term wind observations. *Renewable Energy*, 20(2):145–153.

Maclagan-Wedderburn, E. (1904). Seiches observed in Loch Ness. *The Geographical Journal*, 24(4):441–442.

Menounos, B., Hugonnet, R., Shean, D., Gardner, A., Howat, I., Berthier, E., Pelto, B., Tennant, C., Shea, J., Noh, M., Brun, F., and Dehecq, A. (2019). Heterogeneous changes in western North American glaciers linked to decadal variability in zonal wind strength. *Geophysical Research Letters*, 46(1):200–209.

Meteorological Service of Canada (2015). *Manual of Surface Weather Observations*. Environment Climate Change Canada, Gatineau QC, 479pp.

Meyers, M. P. and Steenburgh, J. W. (2013). Mountain Weather Prediction: Phenomenological Challenges and Forecast Methodology. In Chow, F. K., De Wekker, S. F., and Snyder, B. J., editors, *Mountain Weather Research and Forecasting*, pages 1–34. Springer-Verlag, Berlin.

Naizghi, M. S. and Ouarda, T. B. M. J. (2017). Teleconnections and analysis of long-term wind speed variability in the UAE. *International Journal of Climatology*, 37(1):230–248.

Oke, T. R. (1987). *Boundary Layer Climates, 2nd edition*. Routledge, New York, 435pp.

Okihiro, M., Guza, R. T., and Seymour, R. J. (1993). Excitation of seiche observed in a small harbor. *Journal of Geophysical Research*, 98(C10):18201–18211.

Onset computer corporation (2017). Onset meteorological products: HOBO U30-NRC-

SYS-B description. (Retrieved from http://www.onsetcomp.com/products/kits/u30-nrc-sys-c).

Petersen, E. (1993). Wind resources part I: The European wind climatology. *1993 European Community wind energy conference*, pages 663–668.

Petersen, E. L., Mortensen, N. G., Landberg, L., Højstrup, J., and Frank, H. P. (1998). Wind power meteorology. Part I: climate and turbulence. *Wind Energy*, 1(1):2–22.

Petticrew, E. L., Albers, S. J., Baldwin, S. A., Carmack, E. C., Déry, S. J., Gantner, N., Graves, K. E., Laval, B., Morrison, J., Owens, P. N., Selbie, D. T., and Vagle, S. (2015). The impact of a catastrophic mine tailings impoundment spill into one of North America's largest fjord lakes: Quesnel Lake, British Columbia, Canada. *Geophysical Research Letters*, 42(9):3347–3355.

Potts, D. J. (2004). *The heat budget of Quesnel Lake, British Columbia*. Masters thesis, University of British Columbia, 80pp.

Rabinovich, A. B. and Monserrat, S. (1998). Generation of meteorological tsunamis (large amplitude seiches) near the Balearic and Kuril Islands. *Natural Hazards*, 18(1):27–55.

Radic, V., Menounos, B., Shea, J., Fitzpatrick, N., Tessema, M. A., and Déry, S. J. (2017). Evaluation of different methods to model near-surface turbulent fluxes for a mountain glacier in the Cariboo Mountains, BC, Canada. *Cryosphere*, 11(6):2897–2918.

Richardson, L. F. (1920). The supply of energy from and to atmospheric eddies. *Proceedings of the Royal Society A: Mathematical, Physical and Engineering Sciences*, 97(686):354–373.

Ricker, W. E. (1947). Hell's Gate and the sockeye. *Journal of Wildlife Management*, 11(1):10–20.

Romero-Centeno, R., Zavala-Hidalgo, J., Gallegos, A., and O'Brien, J. J. (2003). Isthmus of Tehuantepec wind climatology and ENSO signal. *Journal of Climate*, 16(15):2628–2639.

Rueda, F., Vidal, J., and Schladow, G. (2009). Modeling the effect of size reduction on the stratification of a large wind-driven lake using an uncertainty-based approach. *Water Resources Research*, 45(3):W03411.

Rueda, F. J., Schladow, S. G., Monismith, S. G., and Stacey, M. T. (2005). On the effects of topography on wind and the generation of currents in a large multi-basin lake. *Hydrobiologia*, 532(1):139–151.

Ryan, B. C. (1977). A mathematical model for diagnosis and prediction of surface winds in mountainous terrain. *Journal of Applied Meteorology*, 16(6):571–584.

Schuenemann, K. C. and Cassano, J. J. (2010). Changes in synoptic weather patterns and Greenland precipitation in the 20th and 21st centuries: 2. Analysis of 21st century atmospheric changes using self-organizing maps. *Journal of Geophysical Research Atmospheres*, 115(D5):D05108.

Scrivener, C., Brown, T. C., and Andersen, B. C. (1994). Juvenile Chinook Salmon utilization of Hawks Creek, a small and nonnatal tributary of the Upper Fraser River. *Canadian Journal of Fish and Aquatic Sciences*, 51:1139–1146.

Seguro, J. V. and Lambert, T. W. (2000). Modern estimation of the parameters of the Weibull wind speed distribution for wind energy analysis. *Journal of Wind Engineering and Industrial Aerodynamics*, 85(1):75–84.

Sentlinger, G. I., Hook, S. J., and Laval, B. (2008). Sub-pixel water temperature estima-

tion from thermal-infrared imagery using vectorized lake features. *Remote Sensing of Environment*, 112(4):1678–1688.

Sharma, A. R. and Déry, S. J. (2016). Elevational dependence of air temperature variability and trends in British Columbia's Cariboo Mountains, 1950-2010. *Atmosphere - Ocean*, 54(2):153–170.

Sheridan, S. C. and Lee, C. C. (2011). The self-organizing map in synoptic climatological research. *Progress in Physical Geography*, 35(1):109–119.

Shintani, T., de la Fuente, A., Niño, Y., and Imberger, J. (2010). Generalizations of the Wedderburn number: Parameterizing upwelling in stratified lakes. *Limnology and Oceanography*, 55(3):1377–1389.

Shteinman, B., Eckert, W., Kaganowsky, S., and Zohary, T. (1997). Seiche-induced resuspension in Lake Kinneret: A fluorescent tracer experiment. *Water, Air, and Soil Pollution*, 99(1-4):123–131.

Singer, I. A. (1967). Steadiness of the wind. *Journal of Applied Meteorology*, 6:1033–1038.

Skific, N. and Francis, J. (2018). Self-Organising Maps: A Powerful Tool for the Atmospheric Science. In *Developments and Applications of Self-Organizing Maps*, volume 2, chapter 13, page 64.

Small, D., Atallah, E., and Gyakum, J. (2011). Wind regimes along the Beaufort Sea coast favorable for strong wind events at Tuktoyaktuk. *Journal of Applied Meteorology and Climatology*, 50(6):1291–1306.

Spigel, R. H. and Imberger, J. (1980). The classification of mixed-layer dynamics of lakes of small to medium size. *Journal of Physical Oceanography*, 10(7):1104–1121.

Stahl, K., Moore, R. D., and McKendry, I. G. (2006). The role of synoptic-scale circulation

in the linkage between large-scale ocean-atmosphere indices and winter surface climate in British Columbia, Canada. *International Journal of Climatology*, 26(4):541–560.

Stevens, C., Lawrence, G., Hamblin, P., and Carmack, E. (1996). Wind forcing of internal waves in a long narrow stratified lake. *Dynamics of Atmospheres and Oceans*, 24(1–4):41–50.

Stockner, J. G. and Shortreed, K. S. (1983). A comparative limnological survey of 19 sockeye salmon (Oncorhynchus nerka) nursery lakes in the Fraser River system, BC. *Canadian Technical Report of Fisheries and Aquatic Sciences*, 1190(1190):64.

Stull, R. B. (1988). *An Introduction to Boundary Layer Meteorology*. Kluwer Academic Publishers, Boston, 666pp.

Taylor, G. (1916). Skin friction of the wind on the earth's surface. *Proceedings of the Royal Society A: Mathematical, Physical and Engineering Sciences*, 92(637):196–199.

Tuller, S. E. (2004). Measured wind speed trends on the West Coast of Canada. *International Journal of Climatology*, 24(11):1359–1374.

Tuller, S. E. and Brett, A. C. (1984). The characteristics of wind velocity that favor the fitting of a Weibull distribution in wind speed analysis. *Journal of Climate and Applied Meteorology*, 23:124–134.

Valerio, G., Cantelli, A., Monti, P., and Leuzzi, G. (2017). A modeling approach to identify the effective forcing exerted by wind on a prealpine lake surrounded by a complex topography. *Water Resources Research*, 53(5):4036–4052.

Van Den Hoek, J., Read, J. S., Winslow, L. A., Montesano, P., and Markfort, C. D. (2015). Examining the utility of satellite-based wind sheltering estimates for lake hydrodynamic modeling. *Remote Sensing of Environment*, 156:551–560.

Wan, H., Wang, X. L., and Swail, V. R. (2010). Homogenization and trend analysis of Canadian near-surface wind speeds. *Journal of Climate*, 23(5):1209–1225.

Whiteman, D. C. (2000). *Mountain Meteorology: Fundamentals and Applications*. Oxford University Press, Oxford, 355pp.

Wilks, D. S. (2011). *Statistical Methods in the Atmospheric Sciences*. Academic Press, Oxford, 680pp.

Wilson, M. V. H. (1977). Paleoecology of Eocene lacustrine varves at Horsefly, British Columbia. *Canadian Journal of Earth Sciences*, 14(5):953–962.

Wüest, A., Piepke, G., and Van Senden, D. C. (2000). Turbulent kinetic energy balance as a tool for estimating vertical diffusivity in wind-forced stratified waters. *Limnology and Oceanography*, 45(6):1388–1400.

Yarnal, B. (1993). *Synoptic climatology in environmental analysis: A primer*. Belhaven Press, London, 195pp.

Yarnal, B., Comrie, A. C., Frakes, B., and Brown, D. P. (2001). Developments and prospects in synoptic climatology. *International Journal of Climatology*, 21(15):1923–1950.